UNIVERSITY OF LIVERPOOL

Department of Electrical Engineering and Electronics

Development of MAST-U Langmuir Probe Interpretation Through Particle-in-cell Simulation and Experiment

Thesis submitted in accordance with the requirements of the University of Liverpool for the degree of Doctor in Philosophy by

Jack Eliot Leland

March 2021

Abstract

Interpreting flush-mounted Langmuir probes at small angles of magnetic field incidence – routinely found in tokamak plasma facing components (PFCs) by design – is notoriously problematic due to the difficulty of accounting properly for sheath expansion. The Mega Amp Spherical Tokamak Upgrade (MAST-U) has 850 probes installed with a novel probe tip designed to mitigate the effects of sheath expansion. This angled-tip design has been investigated through experimental and computational means, to both verify that the design works as intended and to provide insight on how best to interpret the IV characteristics in preparation for the upcoming MAST-U physics campaign.

A rederivation of Bergmann and Murphy-Sugrue's sheath expansion model, and associated parameter, is presented for the novel geometry of the MAST-U angled-tip probe. Two alternate formulations are presented with different approximations of the sheath shape around the probe. This model was verified with 2D3V particle-in-cell simulations, using the code SPICE, of the plasma around a flush-mounted probe tip and an angled-tip probe with MAST-U-like physical proportions. The rotated-rectangular model was found to describe the sheath expansion well for both probes, with new values found for the sheath expansion parameter coefficients for the angled-tip case. An investigation of the effect of wall potential on probe measurements is also presented. Additional current was collected for $V_w < V_{fl}$ due to the reduced wall-sheath height, which must be accounted for to ensure accurate density measurements with probes in this scenario. A method to correct for this additional current is presented.

A 4-probe array of MAST-U-like angled-tip probes was also taken to the linear plasma device Magnum-PSI at the Dutch Institute for Fundamental Energy Research (DIFFER). Parameter scans were made on a range of plasmas in conditions comparable to those expected in MAST-U. Plasma parameters were extracted from the measured IV characteristics – using a novel fitting approach that minimised a goodness-of-fit parameter ($T_e \delta T_e$) – and compared to Magnum-PSI Thomson scattering measurements. The measured plasma parameters show that the MAST-U angled-tip design seems to successfully mitigate the effects of sheath expansion at low angles of magnetic field incidence. The standard MAST-U Langmuir probe also shows an apparent upper operational limit of $\theta = 8°$. This covers the vast majority of expected plasma configurations in MAST-U when running both conventional and Super-X configurations.

Acknowledgements

The work presented here would not be possible without the guidance and support of many people who are gratefully acknowledged here. I would firstly like to thank my supervisors Sarah Elmore and James Bradley. Their direction and enthusiasm, both throughout the PhD and during the writing up process, has been indispensable. It was not always an easy process, so I thank you both for your patience and understanding. I would also like to thank Andrew Kirk for stepping in as an interim supervisor and for the insightful discussions that punctuated my third year.

CCFE has been an extremely fruitful place of work, in no small part due to the incredible staff that have helped me throughout. Particular thanks in that regard go to Scott Allan for the tremendous help with the DSF and navigating UKAEA bureaucracy. Thanks also go to James Harrison, Jack Lovell and Andrew Thornton, as well as heartfelt apologies to the team in electronics for the number of MAST-U power supplies *used* in my experiments. I am also grateful to Fulvio Militello for his boundless generosity.

This project was made possible by a great number of European collaborations. Huge thanks go to Michael Komm and Ales Podolnik, without whom half of this thesis would not exist. Thanks for the other half go to the team at Magnum-PSI, in particular to Hennie van der Meiden, John Scholten, Serge Brons and Thomas Morgan. Particular thanks also go to Jonathan van den Berg-Stolp and Karol Jesko for their indomitable assistance both on and off the machine. I would also like to offer a great personal thanks to Mozghan Laki, Bram Lamers, Joe Allcock and Fabio Federici for making my time in Eindhoven unforgettable.

During this PhD, I have had the great privilege of meeting many wonderful fellow students and making many lifelong friends. The full list is certainly too long to include here, but my heartfelt thanks go to Samuel Ward, Charlie Vincent, Bhavin Patel, Simon Orchard, Thomas Nicholas, Omkar Myatra, and Sam Gibson for bringing endless joy to my post-graduate existence.

Eternal thanks go to my family, both by blood and by marriage – your unwavering support and generosity made all of this possible. Particular thanks go to Ben, Emma and Lulu for providing a warm place to type during these closing weeks.

A final and formidable gratitude goes to Rona Costello, whose boundless energy and support have been utterly invaluable.

Oh, and Tom.

Declaration

I declare that the work presented in this thesis, other than contributions cited or acknowledged in the text, is my own.

Jack Leland, March 2021.

Contents

List of Figures

List of Tables

Chapter 1

Introduction

1.1 Global Energy Demand

The 20^{th} and 21^{st} centuries have seen an enormous increasing trend in the consumption of energy across the vast majority of human societies. This trend is projected to continue well into this century as nations in Africa and Asia continue to develop industrially and grow their populations, resulting in a growth of world energy consumption by 1.3% per year until 2040[1]. This growth has historically been powered through the carbon-intensive combustion of fossil fuels, of which the advantages are numerous: low cost, highly energy dense and abundance of fuel supply. However, the need to reduce CO_2 emissions to limit the effects of human induced climate change is now more clear than ever[2], with most nations now legally committed to keeping average global temperature rise below $2.0°C$ compared to pre-industrial levels[3].

Nuclear fusion is a long-term solution to fulfilling these energy needs without emitting CO_2. It will likely be advantageous over nuclear fission – its main competitor amongst firm (i.e. non-intermittent), low carbon sources – through inherent safety from meltdown and non-proliferation of weapons-grade nuclear materials (the specifics of this are nuanced however, and discussed in more detail in Appendix A). It is therefore important to solve the outstanding problems in fusion research and bring this technology to fruition.

1.2 Fusion

Fusion is a reaction between two nuclei that occurs when a collision of sufficient energy, overcoming the coulomb repulsion between like charges, allows the strong nuclear force to combine the nuclei together into a new, energetically favourable nuclear configuration. If the binding energy of the new nucleus is smaller than the incoming nuclei, as is the case for most elements less massive than iron, then the reaction releases this excess energy through its products.

1.2.1 Candidate Reactions

The main candidate reactants for controlled fusion are deuterium and tritium (DT), two isotopes of hydrogen with one and two extra neutrons respectively. The equation for this reaction is given by:

$$ {}^{2}_{1}H + {}^{3}_{1}H \rightarrow {}^{4}_{2}He + {}^{1}_{0}n + 17.59MeV \tag{1.1} $$

where ${}^{2}_{1}H$, ${}^{3}_{1}H$ and ${}^{4}_{2}He$ are deuterium, tritium and helium respectively. This reaction is chosen because, when compared to other viable fusion reactions (e.g. deuterium-deuterium, proton-boron, deuterium-helium3, proton-lithium6 etc.), its cross-section peak is both an order of magnitude higher than other candidate reactions, and is at the lowest energy ($100keV$ – see fig. 1.1). These fuels are also convenient in terms of their abundance. Deuterium is highly abundant in seawater as it comprises approximately 0.017% of the hydrogen in all water molecules. Tritium is not naturally abundant on earth due to its short half-life of 12.5 years, but it can be 'bred' from lithium via two separate neutron capture reactions:

$$\begin{aligned} {}^{1}_{0}n + {}^{7}_{3}Li &\rightarrow {}^{3}_{1}H + {}^{4}_{2}He + {}^{1}_{0}n - 2.8MeV \\ {}^{1}_{0}n + {}^{6}_{3}Li &\rightarrow {}^{3}_{1}H + {}^{4}_{2}He + 4.8MeV \end{aligned} \tag{1.2}$$

The idea is that lithium is placed surrounding a DT fusion reaction and the neutrons produced via eq. (1.1) are used to produce the tritium required for further fusion reactions. As lithium is abundant in the Earth's crust this therefore gives fusion a supply of fuel which even pessimistically would last centuries – providing no other material constraints are imposed by other parts of the reactor[4]. This of course relies on an initial starter supply of tritium, which is present in the ∼10kg civilian supply generated from Canada Deuterium Uranium (CANDU) fission reactors. Due to the aforementioned half-life, this available tritium inventory will shrink every year that fusion is delayed, underscoring the need to develop this technology as soon as possible.

As the reserves of tritium are so limited, it is rarely used in experiments unless absolutely necessary. The vast majority of fusion devices therefore utilise a purely deuterium fuel mixture, resulting in the following reactions

$$\begin{aligned} {}^{2}_{1}H + {}^{2}_{1}H &\rightarrow {}^{3}_{1}H + {}^{1}_{0}p + 4.03MeV \\ {}^{2}_{1}H + {}^{2}_{1}H &\rightarrow {}^{4}_{2}He + {}^{1}_{0}n + 3.27MeV \end{aligned} \tag{1.3}$$

which occur with equal probability. The tritium produced by eq. (1.3) is burned up almost immediately, through eq. (1.1), due to its much larger cross section (see fig. 1.1).

1.2.2 Criteria for Energy Gain

We can produce collisions of the peak cross-section energy for the DT reaction by heating a gas to a temperature where a significant portion of the particles have the requisite energy

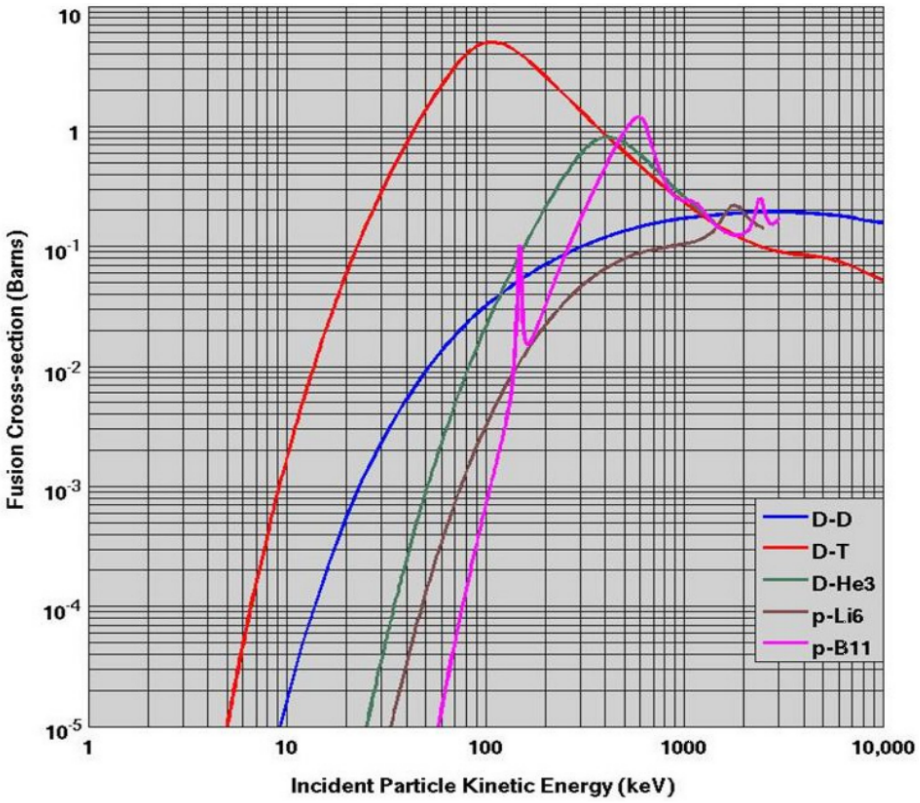

Figure 1.1: Graph showing the cross sections, in Barns, for a variety of candidate fusion reactions.

to fuse. This corresponds to a temperature on the order of 15keV (10^8K), at which any gas will be energetic enough to ionise and become a plasma – a state of matter consisting of freely moving electrons and ions. Therefore net energy can be achieved by confining a DT plasma at this high temperature and for a sufficiently long time.

This statement can be expressed mathematically by the Lawson criterion[5], which is the requirement for igniting a fusion plasma, i.e. heating via the released fusion products is greater than the external sources of heating. This was later extended to the triple product which states that a fusion plasma is ignited if it obeys the following inequality

$$nT\tau_E \geq \frac{12k_B}{E_{ch}} \frac{T^2}{\langle \sigma v \rangle} \tag{1.4}$$

where n and T are the density and temperature of the plasma, τ_E is the confinement time (a measure of the rate at which a system loses energy to its environment), k_B is the Boltzmann constant, E_{ch} the energy of charged fusion products, and $\langle \sigma v \rangle$ is the average over the Maxwellian velocity distribution v with temperature T and cross section σ. The left-hand side (LHS) is the triple product and the right-hand side (RHS) gives a minimum value for this triple product in order to achieve 'break-even' – power being released by the fusion reactions is equal to the required heating power. This is known as the Q value and needs to be greater than 1 for net energy to be produced.

1.3 Plasma Confinement

There are two principal methods of producing the necessary temperatures and densities required to satisfy the Lawson criterion in a terrestrial fusion device: magnetic confinement fusion (MCF) and inertial confinement fusion (ICF). In short, MCF utilises magnetic fields to confine plasmas such that fusion can occur, and ICF does so through compression of a DT pellet to extreme, but transient, temperatures and densities. This body of work will be focused on MCF.

1.3.1 Single Particle Motion

It would be prudent to first examine how a plasma interacts with a magnetic field. The individual constituents of a plasma are freely moving charged particles, so their movements can be described by the Lorentz force

$$m_i \frac{\mathrm{d}\mathbf{v_i}}{\mathrm{d}t} = q_i(\mathbf{E} + \mathbf{v_i} \times \mathbf{B}) \tag{1.5}$$

for a particle of mass m_i with charge q_i moving at a velocity $\mathbf{v_i}$.

In the case of a single charged particle in a magnetic field, with no external electric field, this results in a gyration about the magnetic field. The frequency of this gyration is described by the gyrofrequency (or cyclotron frequency)

$$\omega_c \equiv \frac{|q|B}{m} \tag{1.6}$$

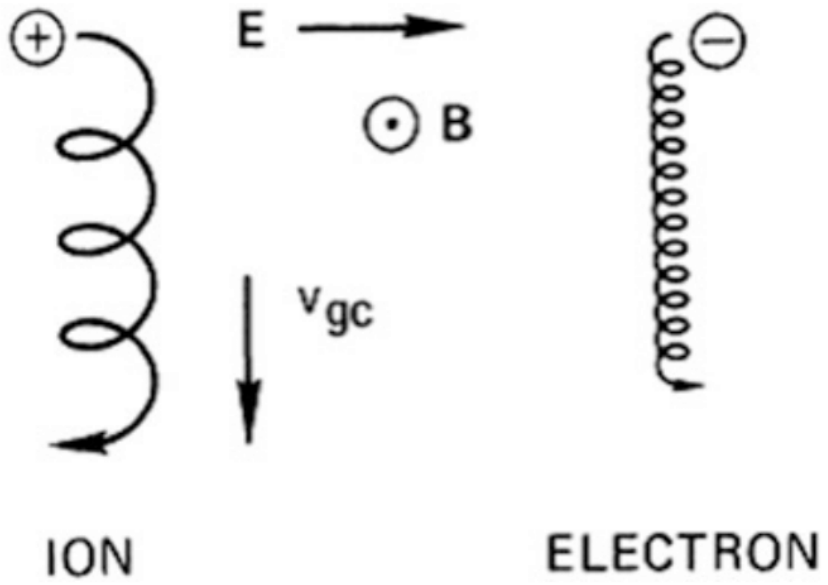

Figure 1.2: Diagram showing the drift of ions and electrons in an electromagnetic field. The ions and electrons gyrate in different directions because of their opposite charge and have different radii due to their differing masses[6].

and size of the gyration is described by the Larmor radius

$$\rho_L \equiv \frac{v_\perp}{\omega_c} = \frac{m v_\perp}{|q|B}. \tag{1.7}$$

These are both mass dependent, so electrons in a plasma will have smaller Larmor radii than ions and will gyrate more quickly. The direction of motion is also charge dependent, with the magnetic field generated by the particle being opposite to the external field. This motion is entirely within the plane perpendicular to the magnetic field, so the particle will generally travel in a helical trajectory along a field line, assuming there is some parallel component of velocity $v_\parallel$. The particles are said to gyrate about a guiding centre.

The situation changes somewhat if we introduce an electric field. If we choose the electric field to lie perpendicular to the magnetic field, there is still circular Larmor motion as before, but with an additional velocity added to the guiding centre in the direction perpendicular to both **E** and **B**. This is known as an $E \times B$ drift, and is caused by the particle being accelerated and decelerated on alternate sides of its Larmor orbit. This concept can also be

extended to other forces which would cause a similar, periodic contraction and expansion of the Larmor orbit, such as a gradient in the magnetic field ($\boldsymbol{\nabla} B$ drift), a centrifugal force acting on a particle moving along a curved field line (curvature drift), or due to a time varying electric field (polarisation drift).

1.3.2 Tokamaks

Given that ions and electrons in a plasma are confined to magnetic fields, the first thought for a magnetic confinement device might be to simply arrange a magnetic field into a torus (a toroidal field) and therefore force the particles to gyrate around the field lines forever. This simple solution does not work however, as the curved nature of the field invariably leads to a radial gradient in the magnetic field, and so a $\boldsymbol{\nabla} B$ drift, as well as a curvature drift through the centrifugal force. These drifts act on the ions and electrons in opposite directions – up and down – so a charge separation is created, leading to an electric field, and thus an $E \times B$ drift out of the plasma.

A combination of a toroidal (B_t) and a poloidal (B_p) magnetic field (see fig. 1.3a) mitigates this problem however, as the resultant helical field means the gyrating particles experience a periodically changing $\boldsymbol{\nabla} B$ drift over the course of their orbit. The drift direction is therefore also periodically changing and results in no net drift occurring, maintaining confinement. To generate these magnetic fields there are several approaches, but the most advanced, and most relevant to this body of work, is a configuration known as a tokamak[7]. This uses electromagnetic coils to produce the toroidal field and a central solenoid to induce a current density in the plasma and generate the poloidal field [8]. This induction of the plasma current (I_p) is however dependent on a time-varying change of current in the central solenoid and therefore limits the tokamak to short pulses of operation. Alternative current drive methods are being explored to allow for steady state operation [9]. Additional poloidal field coils are used to shape and control the plasma, though conventionally the solenoid provides the majority of the confining poloidal field.

The induced plasma current also serves to Ohmicly heat the plasma in a tokamak through resistivity. Currently plasma currents of a few MA can be created using this method, but as resistivity (ν) decreases with increasing temperature ($\nu \propto T_e^{-\frac{2}{3}}$) the amount of heating this can provide is both limited and insufficient to reach the temperatures necessary to assuage the Lawson criterion. Other methods of heating are therefore needed to attain higher temperatures, including the use of beams of neutral particles and electromagnetic

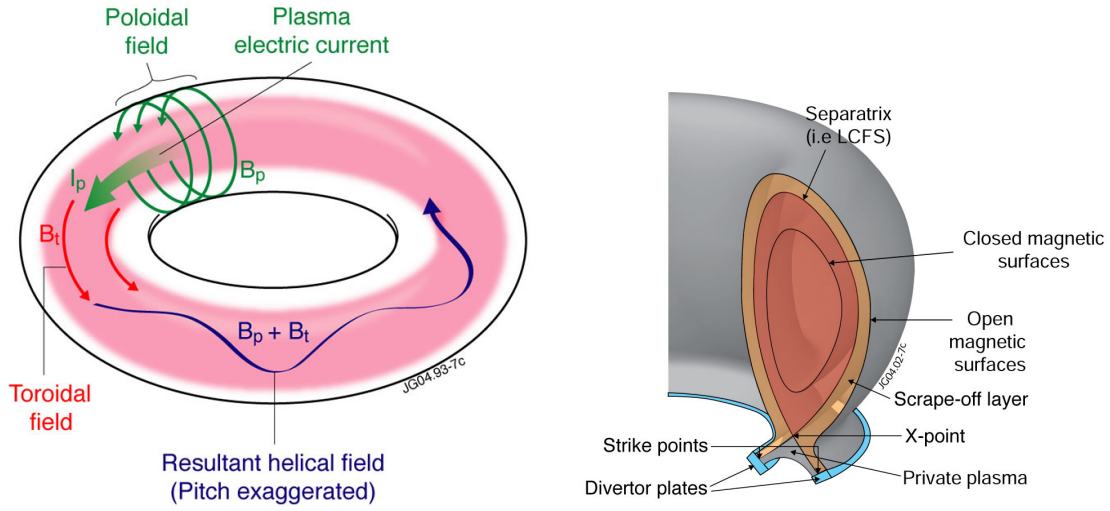

(a) (b)

Figure 1.3: (a) A diagram of the magnetic field configuration needed for confinement in a tokamak (b) A diagram of the regions within a tokamak plasma, including the SOL and the divertor.

waves.

A variation on this design is the spherical tokamak, a tokamak with a smaller ratio between the major radius R and the minor radius a. This makes the torus into a "cored apple" shape (spherical with a central cylinder removed) and allows for a higher ratio of plasma pressure to magnetic pressure (β), meaning that for the same magnetic field strength better confinement can be achieved. The original Mega Amp Spherical Tokamak (MAST)[10], and its subsequent upgrade MAST-U, are examples of such devices.

1.3.3 Limiters and Divertors

Particles in a tokamak move along field lines, but can still diffuse across field lines and will therefore eventually move outwards and hit the vessel wall. Any plasma in contact with a surface will cause it to sputter, sending impurities into the plasma and degrading performance through radiative loss of energy. Additionally, high heat fluxes can cause damage to plasma facing components (PFCs) through erosion, requiring more frequent replacement and raising the cost of an eventual commercial reactor. To mitigate these effects MCF devices must limit plasma contact with the PFCs.

The simplest method of separating the plasma from the vessel wall is by inserting a

solid piece of material into the plasma to break field lines. This solid piece of material is called a limiter, and can be inserted either polloidally or toroidally. Any field line which ends at this limiter surface is deemed 'open' and any field line which does not is 'closed', and the outermost flux surface with closed field lines is termed the Last Closed Flux Surface (LCFS). As particles move much more quickly along magnetic field lines than across them, a thin, fast-flowing layer of plasma outside the LCFS called the scrape-off layer (SOL) is also formed. An advantage of this is that the helium 'ash' produced by the fusion reactions in the core, which is detrimental to performance, is removed quickly by the SOL once it crosses the LCFS.

The width of the scrape off layer is largely determined by how quickly particles diffuse between field lines (cross-field transport), and can be therefore be written as

$$\lambda_{SOL} = \sqrt{\frac{D_\perp L_\parallel}{c_s}} \tag{1.8}$$

where $D_\perp$ is the radial diffusion coefficient (units of $\mathrm{m^2 s^{-1}}$), $L_\parallel$ is the connection length (half the total length of the SOL from limiter surface to limiter surface along a field line). c_s is the sound speed in the plasma, which will be described in chapter 2. The SOL width is typically on the order of ~ 1 cm, and therefore shows us the disadvantage of using a limiter: the high heat loads of the plasma are concentrated into a small region of the limiter by the SOL, causing sputtering. Given the close proximity of the limiter to the core plasma, the probability of these sputtered impurities diffusing back into the core and degrading performance is high.

A divertor can alternatively be used, which separates the target from the core by creating a poloidal current in the same direction as the plasma current above and/or below the core plasma, forming a magnetic null (X-point) between the two regions. The LCFS will pass through this X-point and is sometimes termed the separatrix, outside of which the open field lines end on a target surface and the SOL is formed. The points on the divertor plates where the open field lines connect to the X-point are called the strike points (see fig. 1.3b).

This configuration is advantageous as it physically separates the material surfaces from the core plasma and therefore lowers the probability of impurity diffusion into the core. It also increases the field line connection length, meaning that particles flowing in the SOL travel further, radiatively losing energy as they do so and therefore lowering the heat flux to the divertor target plate. A further benefit of the divertor configuration is that it allows

access to the high confinement mode (H-mode) of tokamak operation, whereby the core plasma density and temperature increases due to increased confinement time.

1.4 The Heat Exhaust Problem

Divertors have been used for decades with great success, allowing for more stable plasmas to be created. However, large toroidal fusion devices, such as the upcoming International Thermonuclear Experimental Reactor (ITER) project in France[11], will have very high heat fluxes to their divertor target plates because of the high core temperature required. Dealing with and mitigating these heat fluxes is one of the key challenges currently standing in the way of commercial fusion power for toroidal devices[12] and is known as the *Heat Exhaust Problem*.

This problem is being addressed by two general methods: materials science, to find composites, ceramics or alloys that can withstand the high heat fluxes; and plasma physics, to lower the heat and particle loads delivered by the SOL to the material surfaces. This thesis is focused on the latter of these approaches.

1.4.1 MAST-U

A proposed mitigation for the heat exhaust problem is the use of divertor configurations that allow for reduced heat flux to plasma facing components. Mega Amp Spherical Tokamak Upgrade (MAST-U)[13] at CCFE has been designed as an experiment to test several aspects of advanced divertor physics, namely the use of a closed divertor with Super-X capability [14].

The Super-X configuration reduces heat flux by extending the plasma out radially (see fig. 1.4). This increases the size of the strike point, which scales with R for a given SOL width, so the same power is spread over a wider area. Radial extension also increases the length of the field lines connecting the divertor plates ($L_{\|}$) and therefore increases the flight time of particles in the divertor, allowing them to lose energy over a longer period of time. But the key purpose behind this closed divertor is to facilitate detachment.

1.4.2 Detachment

Detachment is a plasma regime in which neutral gas is used as a buffer in front of the divertor target plate[16]. The power coming from the SOL, instead of being localised around

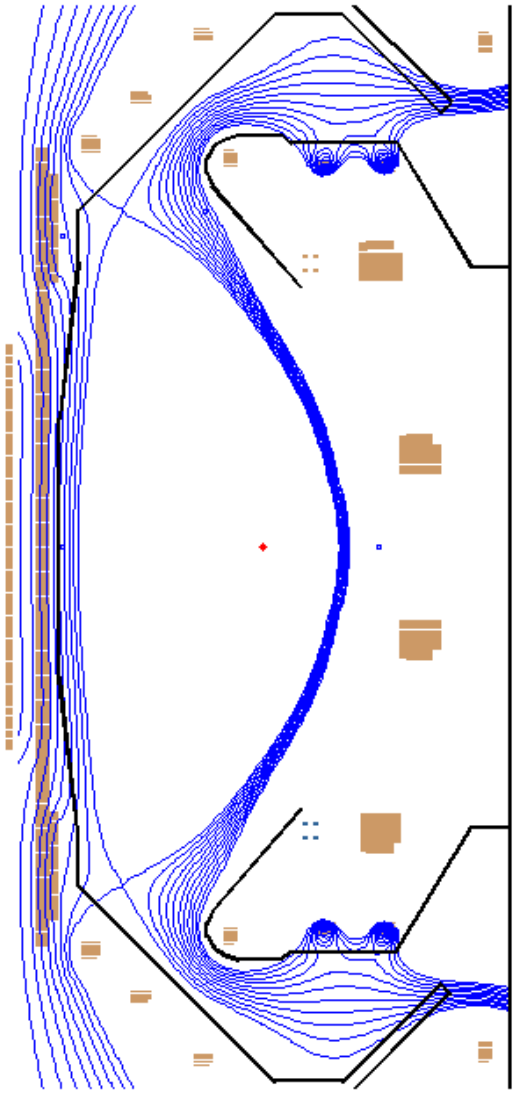

Figure 1.4: Diagram of the magnetic flux of the SOL in Super-X configuration on MAST-U.

the strike point, is transferred to this neutral gas through collisions and then radiated across the whole divertor (see fig. 1.5). This can effectively mitigate the high incoming heat flux if the neutral pressure is able to be pushed high enough. This must be balanced however, as a high neutral pressure in the core results in lower confinement and harder access to high confinement modes of operation (H-mode). These neutrals must therefore be

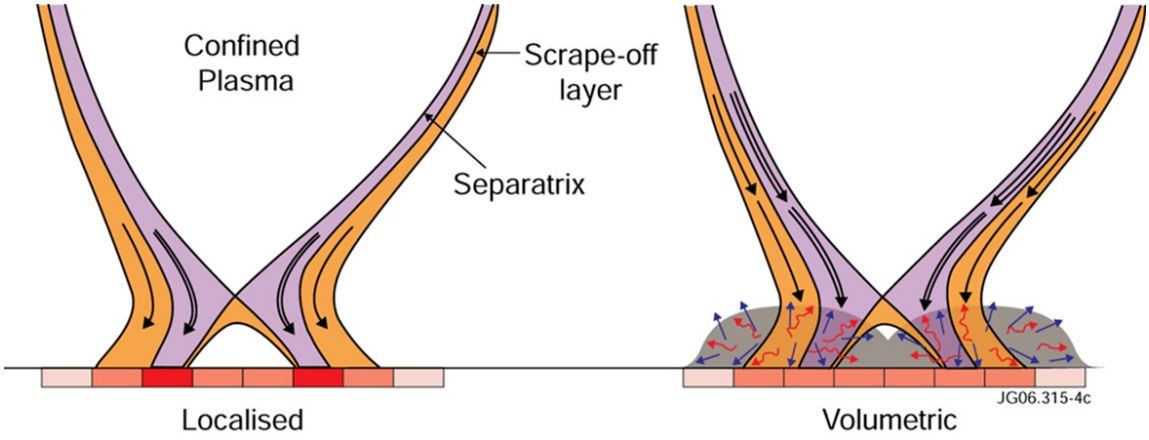

Figure 1.5: Diagram showing the reduction in peak heat flux to a divertor tile in an attached case (left) and a detached case (right)[15].

prevented from accessing the core. The MAST-U divertor has been built with a 'closed' design, meaning that it is separated from the main chamber by a baffle. This should allow for finer control of neutral pressure and for the feasibility of detachment, in tandem with flux expansion, to be experimentally explored and for detailed simulations of the divertor[17] to be verified.

1.4.3 Edge Diagnostics

As the physics in the divertor is crucial to ensuring good exhaust control, it is necessary to understand, with great detail, what goes on in the MAST-U divertor. This is done through the use of different diagnostic techniques which can extract information about certain local and global parameters from the plasma. Particularly of interest to edge plasma physicists are the density and temperature of the plasma, as these tell you how much heat flux is being deposited into the exhaust region of the device. It is therefore of great importance to measure these parameters accurately throughout the divertor.

One of the key diagnostics for measuring these parameters is Thomson scattering (TS), which is a method of obtaining the radial profile of electron temperature in a tokamak, generally (but not always) through the core. It is performed by passing a high power laser through the plasma, which will be scattered off of the electrons. The oscillating electric field of the laser causes the electrons to emit dipole radiation, which will appear in the spectra of collected scattered light as a broadened spectral line around the original laser

frequency. The width of this broadening is related to the thermal motion of the electrons, and can therefore be utilised to infer electron temperature (T_e). Similarly, the amplitude of the spectral line is related to how many electrons were interacted with, and n_e can therefore be calculated through the area under the curve. MAST-U has two TS systems that take profiles of density and temperature across the core and divertor plasmas respectively[18]. However these measurements are spatially restricted, especially in the case of the divertor TS system on MAST-U, which necessitates the use of other diagnostics to get a more holistic impression of the plasma conditions.

1.4.4 Langmuir Probes

Another ubiquitous diagnostic in fusion devices, and one of the key diagnostics in MAST-U, is the Langmuir probe. First devised at the beginning of the 20$^{\text{th}}$ century by Irving Langmuir[19], Langmuir probes have been used widely ever since due to their relative simplicity of operation. In its simplest form, a Langmuir probe is a small electrode inserted into a plasma and biased to a range of voltages – usually in the form of a continuous voltage sweep. The voltage bias on the probe only allows particles of requisite energy to reach the probe and be collected as current. The measured current-voltage (IV) characteristic is therefore analogous to an energy distribution and can thus be interpreted to yield the temperature of the plasma. The plasma potential and floating potential can also be extracted from an IV characteristic. Additionally, at sufficiently negative or positive voltages the current collected by the probe consists solely of ions or electrons respectively. If the area through which this *saturation current* (I_{sat}) is being collected is known then the definition of current can be used to calculate the density of the plasma. The saturation current is also related to the saturation current density (J_{sat}) which gives a measure of particle flux to the wall.

Probes are restricted to taking purely local measurements of the plasma directly in front of the probe tip, and so many must be used in tandem to more extensively characterise the plasma. Fortunately they are relatively cheap and easy to implement – all that is required is a power supply and access to the plasma facing components – and so are widely used in plasma physics research and in fusion devices. However, they are an example of the 'first law of plasma diagnostics'[20] whereby a diagnostic's ease of implementation is inversely proportional to its ease of interpretation. IV characteristics, especially in tokamaks due to the need to flush-mount probes to reduce heat flux, can be notoriously difficult to interpret

correctly and gain accurate measurements of the plasma. The reasons for this are complex, and will be discussed further in chapter 2, but it should suffice to say here that using them in an environment with a strong magnetic field, such as a tokamak, and where this field is at grazing incidence with the probe, such as in the divertor, introduces subtle changes to how the Langmuir probes collect current. This must be properly understood and accounted for if Langmuir probes are to be utilised to their full extent within fusion devices.

1.4.5 MAST-U Langmuir Probes

MAST-U has an extensive suite of Langmuir probes installed, with 850 individual probes arrayed throughout the divertor and PFCs[18]. Of these, 640 can be used simultaneously via sixteenfold multiplexing – i.e. probes are grouped into arrays of 16 and the bias sweep applied to one probe at a time. All probes are partially recessed into the PFCs – to reduce heat flux and therefore reduce sputtering and erosion – and have a special angled-tip design to assist in mitigating the effects of small angles of magnetic field incidence. This design is described in detail in chapter 4.

These probes can be operated in standard swept mode – with the bias voltage able to be varied continuously – or in J_{sat} mode – whereby the probe is held to a fixed, negative bias and collects the saturation current. The former can be used to measure temperature and density profiles of the edge plasma in the divertor with spatial resolutions of 10mm[21]. These measurements allow the strike points to be located and heat fluxes to be determined. The latter can be used to take higher frequency measurements of density[22] (up to 1 MHz). On MAST-U, J_{sat} will primarily be used to study detachment.

1.5 Thesis Motivation

The probe system for MAST-U is vitally important for two key reasons: understanding whether the Super-X divertor is operating correctly, and detecting the onset of detachment. Both of these functions require the probes to be functioning optimally, so it is therefore of great importance to the MAST-U mission, and towards solving the heat exhaust problem, that they are doing so.

This body of work therefore seeks to characterise the performance of the novel Langmuir probe tip design employed in MAST-U, and thereby improve the measurements taken in the MAST-U physics campaign. This will be done in two ways: experimentally and

computationally.

1.5.1 Experiment at Magnum-PSI

The experimental approach to this was conducted with a set of measurements on the Magnum-PSI linear device at the Dutch Institute for Fundamental Energy Research (DIFFER). A linear device is a plasma device whereby the magnetic field is generated by a set of linearly aligned solenoids. The plasma in such a device is not confined and therefore flows directly from a source at one end to a target at the other end, acting much like plasma in the SOL emerging from the core. Linear devices are thus invaluable to researchers as test beds for both divertor physics and diagnostics.

Magnum-PSI was specifically designed to recreate the conditions of the ITER divertor, and has been successfully used to test various designs for the divertor target plates[23]. The target is also able to be manipulated through the use of a target manipulator arm, and so targets can be rotated to the grazing angles of magnetic field incidence present in the divertor. This device therefore offers an opportunity to test the MAST-U probes in a MAST-U-like environment, but with much greater control over magnetic field incidence and local plasma parameters.

1.5.2 Particle-in-cell Simulations

The computational approach to this was conducted using the particle-in-cell (PIC) method of plasma simulation. As Langmuir probes are reliant on the precise kinetics of the plasma constituents around the probe tip, simulations must be done with a fully kinetic code. This means that very few assumptions can be made to simplify the mathematics of the plasma and make the problem more computationally tractable. Unfortunately simulating the exact position and velocity of every particle within a plasma would be far too computationally complex to attempt, even with modern supercomputers. Fortunately, the PIC method of plasma simulation allows us to model the plasma kinetically, preserving most of the relevant physics, while also allowing us to run the simulations in a reasonable time by collecting the motions of groups of particles together into superparticles. These are limited to small regions of plasma to remain tractable, but fortunately the volume of plasma required to be modelled around the probe tip falls within this range. The specifics of this method will be discussed in chapter 3.

PIC simulations of probes have historically been used to great effect to improve upon

the understanding of how Langmuir probes operate within tokamak plasmas[24]. PIC simulations allow the opportunity to control the input temperature, density and magnetic field of the plasma around the probe and can therefore be used to judge how accurate a probe measurement would be through interpretation of the extracted, synthetic IV characteristic. They can also be used to precisely track the movements of individual particles which would be otherwise impossible in a laboratory setting.

The code used in the computational elements of this thesis is the Sheath Particle-in-cell (SPICE) simulation code, developed jointly by the Institute for Plasma Phyics (IPP) in Prague and Alternative Energies and Atomic Energy Commission (CEA)[25]. The 2D and 3D versions of this code family were specifically designed to simulate the physics of plasma surface interactions, and so are uniquely suited among publicly available PIC codes to simulate the plasma around a Langmuir probe.

1.5.3 Outline

In this chapter we have outlined fusion energy: its place in the energy market, its key features, one of the major challenges to its realisation, and how that is being addressed. We have also discussed the importance of Langmuir probes, and in chapter 2 we will examine this diagnostic more closely. This will involve defining key plasma concepts, such as the Debye sheath, how these change in the presence of a magnetic field, and reviewing the literature on interpreting Langmuir probes in tokamaks. Chapter 3 describes the Particle-in-cell methodology of plasma simulation, and describes SPICE – the simulation code used to run simulations in other chapters of the thesis. Chapter 4 outlines the specifics of the MAST-U probe tip design and reviews the setup for the experiment performed on the linear device Magnum-PSI at DIFFER in the Netherlands. The novel approach taken to interpreting the IV characteristics measured there is also discussed. The results from 2D simulations of the MAST-U probe tip are presented in chapter 5, in addition to an expansion to the current probe theory incorporating a shadowed leading edge and an angled surface. Chapter 6 discusses the results from the angular dependence experiment conducted on Magnum-PSI in MAST-U like plasma conditions. The performance of the probe in a range of plasma conditions is also presented. Finally, this work is summarised and its conclusions discussed in chapter 7, alongside suggestions for further work to be done in this field.

Chapter 2

Sheath Physics and Langmuir Probes

2.1 Introduction

Langmuir probes have been used to diagnose plasmas for over a century. Being easy to implement and cheap, they have become the go-to plasma diagnostic for both tabletop laboratory and large collaborative plasma devices since their invention by Langmuir and Mott-Smith [26, 27] in the early 20^{th} century. They provide local measurements of the plasma parameters directly around the probe, and so can be arrayed to easily gain profiles of temperature and density. The relative simplicity of the electronics involved means there is also scope to measure these profiles at high repetition rates; recently Langmuir probes have been designed that can measure once per μs[28, 29].

Unfortunately their use, especially in strong magnetic fields, is marred by difficulties in interpretation. Theories have improved over recent years, but there still remain unresolved issues related to parameter over- and under-estimation. Moreover, given that they require direct contact with the plasma to function, their deployment is limited to conditions in which they can survive. The harsh, strongly magnetised environment of a tokamak is therefore particularly challenging, spelling difficulties for their accurate usage. Nevertheless they are still widely used[18, 30–32], so efforts to improve understanding of their operation and the measurements they make are extremely helpful to both fusion researchers and indeed the greater plasma physics community.

2.2 The Sheath and Pre-Sheath

Given that Langmuir probes require putting a surface in contact with the plasma, understanding of their measurements can only be gained through understanding of the plasma-surface interface. Thus the sheath – the layer of space charge which forms on the surface of any material in contact with a plasma – is of the utmost importance, especially in the context of Langmuir probes, which manipulate it to reveal information about the plasma.

2.2.1 Debye Shielding

Consider a 1D plasma made of singly charged ions and electrons with Maxwellian velocity distributions. The density of electrons and ions is equal ($n_e = n_i$), so there is no net charge. In the absence of an external magnetic field, the behaviour of the plasma is dominated by the electric fields associated with the particles. This can be described by the electric

potential and therefore by Poisson's equation[33]

$$\boldsymbol{\nabla}^2\phi = -\frac{\rho}{\epsilon_0} = -\frac{q}{\epsilon_0}(n_i - n_e) \tag{2.1}$$

which can be rewritten in our 1D, singly charged plasma as

$$\frac{\partial^2\phi}{\partial x^2} = -\frac{e}{\epsilon_0}(n_i - n_e) \tag{2.2}$$

where ϕ is the electrostatic potential.

If a charge is introduced into this plasma, the plasma will rearrange itself so as to shield the bulk plasma from the generated electric field of this perturbing charge. This can be seen if we examine the densities of the electrons and ions in the plasma through eq. (2.2). The ions are much more massive and therefore less mobile than the electrons. We can therefore assume that the ions are immobile and that the electrons adopt a thermal equilibrium distribution, whereby the density is described by the Boltzmann factor

$$n_e = n_0 \exp\left(\frac{e\phi}{k_B T_e}\right) \tag{2.3}$$

where k_B is Boltzmann's constant, T_e is the electron temperature, and n_0 is the density in the bulk plasma, i.e. far away from the perturbing charge. Equation (2.2) then becomes

$$\frac{\partial^2\phi}{\partial x^2} = -\frac{en_0}{\epsilon_0}\left[1 - \exp\left(\frac{e\phi}{k_B T_e}\right)\right]. \tag{2.4}$$

If we assume that $e\phi \ll k_B T_e$, which corresponds to the region where the potential energy of the perturbing charge is much less than the thermal energy of the electrons, we can simplify this through a Taylor expansion of the exponential term $\left(1 + \frac{e\phi}{k_B T_e}\right)$

$$\frac{\partial^2\phi}{\partial x^2} = -\frac{e^2 n_0}{\epsilon_0 k_B T_e}\phi \tag{2.5}$$

which is a second-order differential equation with the solution

$$\phi(x) = -\phi_0 \exp\left(-\frac{x}{\lambda_D}\right) \tag{2.6}$$

where we have defined the *Debye length*

$$\lambda_D \equiv \sqrt{\frac{\epsilon_0 k_B T_e}{e^2 n_0}}. \tag{2.7}$$

The potential therefore decays exponentially with increasing distance from the perturbing charge with characteristic length λ_D. ϕ_0 in this case corresponds to the potential in the bulk plasma. The potential well is called the sheath, and forms in the presence of any unscreened charge in the plasma.

From this definition arises 'quasineutrality', whereby the plasma will inherently screen out any large electric potentials or fields. This means that over scales of plasma size L much larger than λ_D, the n_e and n_i are approximately equal (to within 10^6[6]), but not completely equivalent so as to prevent any electromagnetic forces from arising. This is notably only true in the plasma bulk, the consequences of which will be discussed in section 2.2.2.

It was assumed in this derivation that the ions were 'cold' and so couldn't contribute to the potential screening. A suitable re-expression for eq. (2.7) can be found if we assume the ions have a finite temperature and therefore follow a similar thermal equilibrium distribution to eq. (2.3), i.e.

$$n_i = n_0 \exp\left(\frac{e\phi}{k_B T_i}\right) \tag{2.8}$$

where n_i and T_i are the ion density and temperature respectively, and n_0 is the bulk plasma density. Following the same procedure as above for the cold ion case, we find a modified Debye length of

$$\lambda_D = \left(\frac{\epsilon_0 k_B (T_e + T_i)}{e^2 n_0}\right)^{\frac{1}{2}}. \tag{2.9}$$

2.2.2 Sheath Formation

A further consequence of the higher mobility of the electrons compared to the ions in a plasma is the creation of what is known as a Debye sheath (DS) in front of the vessel walls i.e. the divertor target plates in a tokamak.

We now consider the case of a plasma in contact with a wall. As electrons are less massive than ions by several orders of magnitude, their thermal velocity is much larger and therefore more electrons than ions will diffuse into the neutrally charged wall, negatively charging it. This quickly creates a potential well in front of the wall which both reflects incoming electrons away and accelerates ions toward the wall. As more ions impinge on the

wall it becomes less positively charged and the well shrinks. The height of this potential well therefore spontaneously evolves until the flux of ions and non-reflected electrons to the wall is equal. The potential that the wall relaxes to in order to balance the flux of ions and electrons is called the floating potential (ϕ_{fl}). The distance this sheath encroaches into the plasma is limited to the order of a few Debye lengths by Debye shielding.

In order for this flux-balancing space charge to exist the ion density must be greater than the electron density in the sheath. This in turn requires that the ions enter the sheath at, or above, the sound speed c_s, a condition known as the Bohm criterion[34]. It also implies the existence of a second layer of sheath, the pre-sheath, containing a finite electric field which accelerates ions so they cross the sheath boundary with the requisite velocity. The characteristic length of the pre-sheath is highly dependent on conditions of the plasma, but is generally on the order of many Debye lengths i.e. much longer than the Debye sheath[35].

A simple derivation of this condition can be obtained through examining a 1D plasma with cold ions ($T_i = 0$) in contact with a wall. To do this we must look at the quantities at the sheath edge; the densities of ions and electrons are equal up to the sheath edge ($n_e = n_i = n_{se}$) and we set the potential in the bulk plasma $\phi_0 = 0$ so as to find the potential drop at the sheath edge ϕ_{se}. The electrons are considered again to have a Maxwellian distribution in the sheath and so their density can be described by a Boltzmann relation

$$n_e = n_{se} \exp\left(\frac{e(\phi - \phi_{se})}{k_B T_e}\right). \tag{2.10}$$

From here we consider the ions to originate from the bulk plasma with $T_i = 0$ and be accelerated uniformly by the pre-sheath potential drop. Considering energy and particle conservation (in the absence of particle sources and collisions) for the accelerated ions gives us

$$\textbf{Energy conservation} \qquad \frac{1}{2} m_i v_i^2 = -e\phi, \qquad \frac{1}{2} m_i v_{se}^2 = -e\phi_{se} \tag{2.11}$$

$$\textbf{Particle conservation} \qquad n_i v_i = n_{se} v_{se} = \text{constant} \tag{2.12}$$

where v_i and v_{se} are the velocities of an ion at potentials ϕ and ϕ_{se} respectively. We can rearrange eq. (2.12) to get expressions for v_i and v_{se} and substitute these into eq. (2.12) to

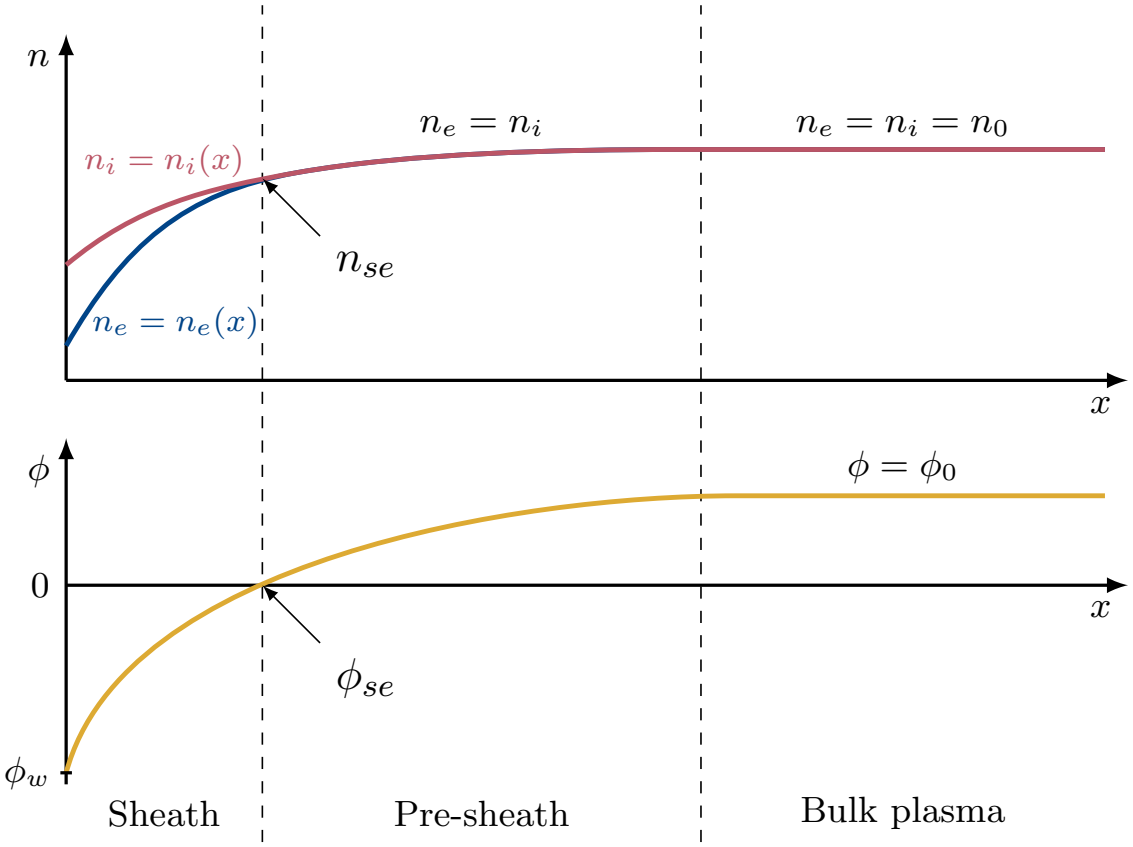

Figure 2.1: Plots showing the 1D variation of potential (bottom) and density (top) in the sheath and pre-sheath. Far from the wall the plasma is quasineutral, but a finite electric field is set up in the pre-sheath to accelerate ions toward the wall. At the sheath edge, where ϕ is set arbitrarily to 0 as a reference, quasineutrality breaks down.

get an expression for the ion density in terms of quantities at the sheath edge

$$n_i = n_{se}\left(\frac{\phi_{se}}{\phi}\right)^{\frac{1}{2}}. \tag{2.13}$$

Thus we now have expressions for n_i and n_e which we can use with Poisson's equation (eq. (2.1)) to get an expression for the potential

$$\frac{\partial^2\phi}{\partial x^2} = -\frac{e}{\epsilon_0}n_{se}\left[\left(\frac{\phi_{se}}{\phi}\right)^{\frac{1}{2}} - \exp\left(\frac{e(\phi-\phi_{se})}{k_B T_e}\right)\right]. \tag{2.14}$$

This describes the potential ϕ from the start of the pre-sheath up to the wall. To solve this for ϕ_{se} we can examine just the sheath region and define a new variable φ such that

$$\varphi = \phi_{se} - \phi. \tag{2.15}$$

As this is always positive we can now approximate the value of eq. (2.14) at the sheath edge by approximating the inner terms using a Taylor series, substituting eq. (2.15) and expanding around $\varphi = 0$. For the first term

$$\left(\frac{\phi_{se}}{\phi}\right)^{\frac{1}{2}} \approx 1 + \frac{1}{2}\frac{\varphi}{\phi_{se}} + ... = 1 - \frac{\varphi}{2|\phi_{se}|} \tag{2.16}$$

and for the second term

$$\exp\left(\frac{e(\phi - \phi_{se})}{k_B T_e}\right) \approx 1 - \frac{e\varphi}{k_B T_e}. \tag{2.17}$$

We can now substitute these back into eq. (2.14)

$$\frac{\partial^2 \varphi}{\partial x^2} = -\frac{e n_{se}}{\epsilon_0}\varphi\left[\frac{e}{k_B T_e} - \frac{1}{2|\phi_{se}|}\right]. \tag{2.18}$$

Now we have a second-order differential equation of the form $x'' = ax$, which only has non-oscillatory solutions for $a > 0$. Assuming that an oscillating sheath would be unphysical, we are therefore left with the inequality

$$\frac{e}{k_B T_e} \geq \frac{1}{2|\phi_{se}|} \tag{2.19}$$

which we can re-express using the conservation of energy (eq. (2.11)) to get

$$m_i v_{se}^2 \geq k_B T_e \tag{2.20}$$

or

$$v_{se} \geq c_s \equiv \sqrt{\frac{k_B T_e}{m_i}} \tag{2.21}$$

which is the Bohm criterion where c_s is the sound speed of ions in the plasma. The physical reasoning for the existence of this requirement is to guarantee the monotonically decreasing potential profile in the sheath and therefore maintain electron reflection[36]. To reach this speed the ions have to be accelerated, so this condition implies the existence of a finite

electric field in the pre-sheath to provide this acceleration. We can estimate the potential drop required for this from our equation for energy conservation

$$\frac{1}{2}m_i c_s^2 = -e\phi_{se} \tag{2.22}$$

which results in

$$\phi_{se} = \frac{k_B T_e}{2e}. \tag{2.23}$$

This criterion can also be derived, albeit in a more complicated fashion, for ions with a finite temperature. The generalised Bohm criterion can be expressed as

$$\int_0^\infty \frac{f_{i,se}(v)}{v^2}\mathrm{d}v \leq \frac{m_i}{k_B T_e} \tag{2.24}$$

where $f_{i,se}(v)$ is the 1D ion velocity distribution at the sheath edge. Various forms of this distribution can be assumed; an assumption of a step-wise function results in a c_s with a similar form to the hot ion Debye length (eq. (2.9))[37]. It has been shown however that the most appropriate form is

$$c_s = \sqrt{\frac{k_B(T_e + \gamma T_i)}{m_i}} \tag{2.25}$$

where γ is the adiabatic constant and should be changed according to the type of flow in the plasma. The best value for this is contentious[36, 38], with the value at the sheath edge best set between 2-3.

2.3 Langmuir Probes

The concept behind the Langmuir probe is elegant in its simplicity; a conductor is inserted into the plasma and a range of bias voltages V_p applied to it. These bias voltages will necessarily change the size and nature of the sheath, allowing different fluxes of particles to reach the conductor and be measured as a current I_{tot}. This current-voltage characteristic (IV) curve is then interpreted to reveal information about the plasma.

2.3.1 Particle Fluxes to a Biased Surface

The derivation of the Bohm criterion in section 2.2.2 assumed that the surface in contact with the plasma was floating, i.e. the wall was isolated and therefore the electron and ion

fluxes to the wall evolved to balance each other. As a probe functions by varying bias potential, different behaviour will arise depending on the size of V_p to the plasma potential Φ. From this section onwards, potentials associated with the probe potential bias will be written as V instead of ϕ.

If we now consider the wall to be a probe biased to a sufficiently negative potential compared to the plasma, the probe will reflect all but the tail of the Maxwellian electron distribution function. This electron contribution can be neglected, leaving just the ion flux to be collected as current. The ion particle flux density to the wall is given by the Bohm criterion

$$\Gamma^i = n_{se} c_s \tag{2.26}$$

from which we can, assuming singly charged ions, obtain current

$$I_i = I_{i,sat} = e n_{se} c_s A_{probe} \tag{2.27}$$

where we have introduced the probe collecting area A_{probe}. As this expression is not dependent on the voltage applied – the current collected is constant – it is referred to as the *ion saturation current*.

We must treat the electrons differently however as the particle flux reaching the probe is dependent on the probe bias. Assuming, as before, that the electrons follow a Maxwellian distribution, their flux to the wall is the one-way random thermal flux. In general for a Maxwellian this is given by

$$\Gamma^{Max} = \frac{1}{4} n \bar{c} \tag{2.28}$$

where $\bar{c}$ is the average thermal velocity of the Maxwellian distribution. Thus for an electron this is

$$\bar{c}_e = \left(\frac{8 k_B T_e}{\pi m_e} \right)^{\frac{1}{2}}. \tag{2.29}$$

We can substitute the density at the probe surface using a Boltzmann factor. This is dependent on the potential, which we will set here as the probe bias potential relative to the sheath edge, setting $\phi_{se} = 0$

$$\Gamma^e = \frac{1}{4} \bar{c}_e n_{se} \exp\left(\frac{e V_p}{k_B T_e} \right). \tag{2.30}$$

As we bias the probe more positively towards the plasma potential, the sheath potential

drop will decrease allowing a larger proportion of the electron population to reach the probe without being reflected in the sheath. The contribution of the electrons to the probe current can therefore no longer be ignored. This part of the IV characteristic is known as the transition region, and is crucial for extracting thermal information about the plasma. The current of the electrons can be obtained from eq. (2.30) in a similar manner to the ion current

$$I_e = \Gamma^e e A_{probe} = \frac{1}{4} e \bar{c}_e A_{probe} n_{se} \exp\left(\frac{eV_p}{k_B T_e}\right) \tag{2.31}$$

which shows us that the electron contribution will increase exponentially as V_p increases towards Φ. The total current in the transition region is therefore given by

$$\begin{aligned} I_{tot} &= I_i - I_e \\ &= e n_{se} c_s A_{probe} - \frac{1}{4} e \bar{c}_e A_{probe} n_{se} \exp\left(\frac{eV_p}{k_B T_e}\right). \end{aligned} \tag{2.32}$$

Biasing the probe further positively, past V_{fl} and up to the plasma potential Φ, the sheath potential drop will disappear as there is no potential difference between the probe and the plasma. As there is no sheath, the probe will collect the random thermal flux of both the electrons and the ions. Increasing the bias any further will form a thin sheath of electrons around the probe to screen out the positive charge. As such the ions will be reflected, and biasing sufficiently positively will reflect all ions, leaving only the electron contribution to be collected. This is generally taken to be current associated with the random thermal flux of electrons, given by

$$I_{e,sat} = \frac{1}{4} e \bar{c}_e A_{probe} n_{se}. \tag{2.33}$$

This is, as before, not dependent on probe bias and so is known as the *electron saturation current*. The potential at which this saturation current is reached can be used to infer Φ. We can compare the ratio of the two saturation currents

$$\frac{I_{e,sat}}{I_{i,sat}} = \left[\frac{m_i}{2\pi m_e}\left(\frac{T_e}{T_e + \gamma T_i}\right)\right]^{\frac{1}{2}} \tag{2.34}$$

and see that $I_{e,sat}$ is generally an order of magnitude larger than $I_{i,sat}$ (assuming $T_e \approx T_i$). For a hydrogen plasma in the cold ion approximation this reduces to ~ 40.

2.3.2 Interpreting the IV Characteristic

Once the probe bias has been swept and the current collected, the full IV characteristic can be plot and interpreted (fig. 2.2). We can write an expression for I_{tot} more simply by considering the currents at the floating potential, i.e. when the flux of electrons and ions to the wall is equal

$$\begin{aligned} I_i &= I_e \\ I_{i,sat} &= I_{e,sat} \exp\left(\frac{eV_{fl}}{k_B T_e}\right). \end{aligned} \tag{2.35}$$

We can use this to rewrite eq. (2.32) as

$$I_{tot} = I_{e,sat} \exp\left(\frac{eV_{fl}}{k_B T_e}\right)\left[1 - \exp\left(\frac{e(V_p - V_{fl})}{k_B T_e}\right)\right] \tag{2.36}$$

or

$$I(V_p) = I_{i,sat}\left[1 - \exp\left(\frac{e(V_p - V_{fl})}{k_B T_e}\right)\right]. \tag{2.37}$$

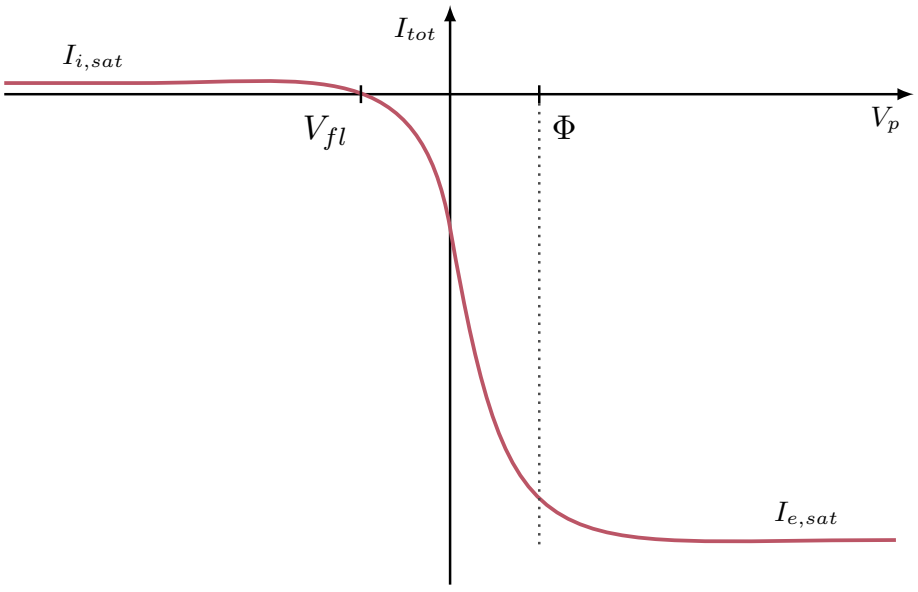

Figure 2.2: A schematic diagram of a single Langmuir probe IV characteristic. The ion and electron saturation currents ($I_{i,sat}$ and $I_{e,sat}$) and the floating and plasma potentials (V_{fl} and Φ) are indicated.

This is the standard 3-parameter Langmuir probe equation, giving the current measured on the probe in terms of the potential applied to it and allowing T_e, V_{fl} and $I_{i,sat}$ to be measured. Note that this is only valid for the transition region and the ion saturation region. The floating potential can be easily read from the x-intercept – where the current becomes 0. $I_{i,sat}$ is also straight forward to read off the IV characteristic as the value the current saturates to when $V_p << V_{fl}$ (aptly named the ion saturation region). T_e can be obtained from the exponential portion of the characteristic i.e. the transition region, through the rate of the exponential decay (or growth depending on current sign convention). In general this is performed by subtracting $I_{i,sat}$ from the whole curve (a mostly valid assumption up to the plasma potential) and then fitting a straight line on a semi-log plot to the transition region. The reciprocal of the gradient of this line is then $k_B T_e/e$. Φ can also be obtained as the potential value at which the current begins to saturate in the electron saturation region. This is usually read graphically from the curve (see fig. 2.2).

This process of parameter extraction can alternatively be done by using a non-linear least squares fit to the whole IV curve (below the plasma potential) using eq. (2.37). This was the method employed throughout this thesis.

Once the three parameters have been extracted from the IV characteristic, the plasma density can be calculated from $I_{i,sat}$ and T_e. Both of eqs. (2.27) and (2.31) we have density at the sheath edge, which we must relate to the plasma density in the bulk n_0. A good approximation of this can be gained by substituting our estimate of ϕ_{se} from section 2.2.2 into the Boltzmann relation eq. (2.3). This comes out as $\exp(1/2) \approx 0.61$, changing our equation for ion saturation current to

$$I_{i,sat} = 0.61 n_e c_s e A_{probe} \tag{2.38}$$

which can be rearranged for n_e. The calculation of c_s requires knowledge of T_i, which is not obtainable from a standard Langmuir probe. As such the value of T_i is often assumed. In divertor plasmas $T_i = T_e$ is usually a good assumption, as was shown to be the case on MAST where T_i was directly measured using a Retarding Field Energy Analyser (RFEA) [39]. This assumption may not hold well closer to the core[40], so reciprocating probes must alter their analysis accordingly. Measurements of T_i by RFEA are planned for MAST-U.

It should be noted as well that eq. (2.35) can be rearranged to find an expression for V_{fl}

$$V_{fl} = \frac{k_B T_e}{2e} \ln \left[2\pi \frac{m_e}{m_i} \left(1 + \frac{\gamma T_i}{T_e} \right) \right]. \tag{2.39}$$

Substituting values for a hydrogen plasma with $T_e = T_i$ results in an approximate V_{fl} of $\sim -3T_e$. The choice of reference potential is also important in this equation. We have chosen a reference whereby $\phi_{se} = 0$, but the reference could instead be made to the plasma potential Φ and this equation used to calculate an estimate of it.

2.4 Probes In A Magnetised Plasma

2.4.1 The Magnetic Pre-sheath

When a magnetic field is applied to a plasma, several important aspects of the sheath change. The application of the field necessarily changes the motion of the ions and electrons, as they are forced to gyrate about the field line and therefore lose a degree of freedom. If the field is applied normal to the surface the plasma is in contact with then the basic premises of our derivation of the Bohm criterion hold; the velocity distribution parallel to the field is still Maxwellian. It is not immediately clear then what happens in the case where the magnetic field makes an angle with the surface.

This question was answered in the seminal work by Chodura[41] through development of a fluid model, backed up with numerical modelling, of the sheath in such a case. In this model, the field was defined to be incident on a plasma-adjacent surface at an oblique angle (θ), mimicking the case in most divertors. Chodura posited the existence of a third region of the sheath between the Debye-sheath and pre-sheath discussed in section 2.2: the magnetic pre-sheath (MPS). This region is an extension of the pre-sheath in that quasineutrality is maintained, but serves a different purpose. The pre-sheath exists to accelerate ions to the requisite velocity to satisfy the Bohm criterion upon entry into the Debye sheath.

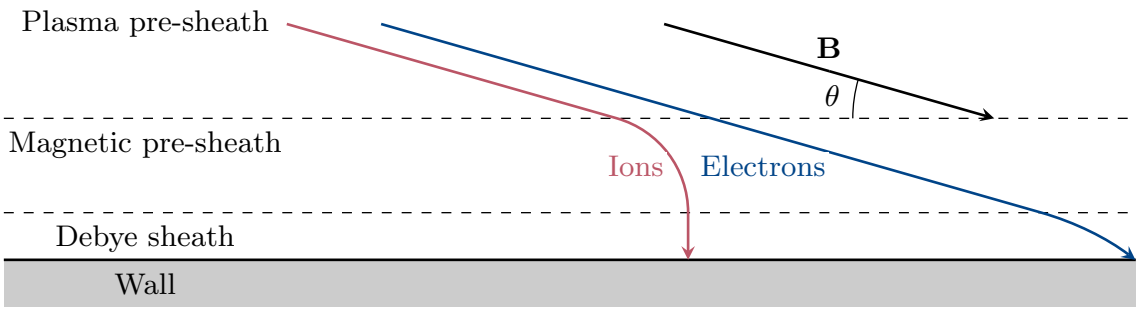

Figure 2.3: Schematic showing the structure of the 3 sheaths in a magnetised plasma, and the approximate trajectories of ions (red) and electrons (blue) within them.

However, it was found that in the case of a plasma where $\theta \neq 90°$, the presheath will accelerate the ions *parallel to the field* and thus they would arrive at the exit of the pre-sheath with

$$v_{\parallel} \geq c_s \tag{2.40}$$

where $v_{\parallel}$ is the ion velocity parallel to the magnetic field. This is known as the *Chodura-Bohm condition*, or sometimes simply the *Chodura condition*. The MPS exists then as an intermediate region, wherein ions arrive with $v_{\parallel} \geq c_s$, and are turned so that upon entrance to the Debye sheath satisfy the original Bohm condition, which we can reinterpret in this context as being

$$v_{se}^{\perp} \geq c_s \tag{2.41}$$

where $v_{se}^{\perp}$ is the velocity normal to the Debye sheath edge or collecting surface (see fig. 2.3). The MPS extends several Larmor radii (ρ_L) into the plasma from the Debye sheath edge, with Chodura deriving the characteristic length more precisely as

$$L_{mps} = \frac{\sqrt{6}c_s}{\omega_{c,i}} \cos\theta \tag{2.42}$$

which tends towards 1 ρ_L as $\theta \to 0$.

The mechanism by which this occurs is a gradient in the electric field in the MPS which results in a polarisation drift[42]. The ions' cyclotron motion is disturbed and they are torn from their magnetic field lines. The electrons, with much smaller Larmor radii, are less affected by this and pass straight through the MPS before being deflected by the stronger E-field in the Debye sheath (see fig. 2.3).

For the electric field in the MPS to appear, a potential drop (V_{MPS}) must be present. When studying the MPS using a fluid model, [43] calculated this potential drop as

$$\frac{eV_{MPS}}{k_B T_e} = \ln(\sin\theta) \tag{2.43}$$

from the conservation of flux at the entrance and exit to the MPS. A further interesting hypothesis from [43] was the argument for a critical angle θ_c at which the Debye sheath disappears completely. The total potential drop between the surface and the entrance to the MPS is equal to the sum of the Debye sheath drop and the MPS sheath drop. In the

case of a floating wall this sum is equal to V_{fl}, i.e.

$$V_{fl} = V_{DS} + V_{MPS} \tag{2.44}$$

where V_{DS} is the potential at the Debye sheath edge (formerly ϕ_{se}). Both of these fluid models showed that V_{fl} is not affected by the incidence angle of the magnetic field (to first order) and so is simply given by eq. (2.39). This can be seen briefly by the combination of eq. (2.43) and the expression for V_{DS}, given by

$$\frac{eV_{DS}}{k_B T_e} = \frac{1}{2}\ln\left[2\pi\frac{m_e}{m_i}\left(1+\frac{\gamma T_i}{T_e}\right)\right] - \ln[\sin\theta] \tag{2.45}$$

where the additional $\ln[\sin\theta]$ term arises from assuming electron flux remains purely parallel to the field and equating it to the turned ion flux perpendicular to the wall. Evaluating this with $V_{DS} = 0$ we can rearrange for θ_c

$$\theta_c = \arcsin\left\{\left[2\pi\frac{m_e}{m_i}\left(1+\frac{\gamma T_i}{T_e}\right)\right]^{\frac{1}{2}}\right\} \tag{2.46}$$

which tells us the angle at which the DS disappears. It is then argued that with no DS the Bohm criterion is no longer limiting and therefore the ions flowing to the wall are necessarily no longer sonic, instead arriving with a mach number dependent on the incident angle. They still enter the Debye sheath perpendicular to the wall however. This subsonic ion flow was later confirmed through kinetic simulations [44], although the disappearance of the Debye sheath was found to be a smooth transition rather than the critical angle predicted by the fluid model in [43].

This phenomenon is also dependent on the wall potential. The specific example used in the derivation was a floating wall, but the derivation can be extended to a general wall potential. In this case wall potentials more negative than V_{fl} will decrease θ_c and more positive potentials increase it.

There is also a density drop across the MPS due to the conservation of the turned fluxes, with the magnitude of the drop given by

$$n_{DS} = n_{MPS}\sin\theta \tag{2.47}$$

where n_{DS} and n_{MPS} are the densities at the entrance to the Debye sheath and MPS

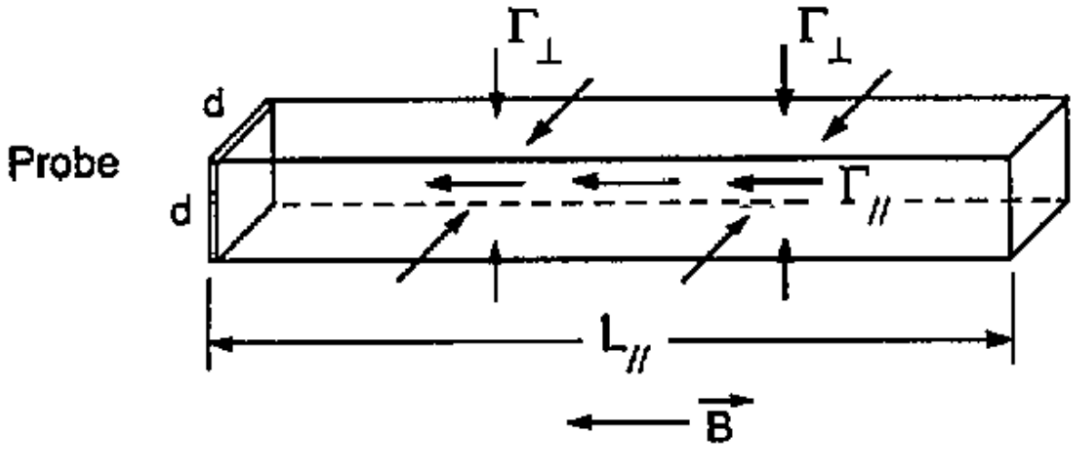

Figure 2.4: Schematic of the collection flux tube subtended by a probe in a strong magnetic field. d in this case denotes probe size, so the cross section of the flux tube is $A = d^2$. Taken from [45].

respectively. This density drop manifests itself in an increase of the local Debye length near the sheath entrance, the consequences of which will be discussed in section 2.4.3.

2.4.2 Magnetised Probe Measurements

In the unmagnetised case, the probe was assumed to collect particles flowing towards it from all directions. With the introduction of a magnetic field, the ions and electrons in the plasma lose a degree of freedom by being forced to gyrate around magnetic field lines, with electrons being more strongly coerced than the ions due to their smaller mass. This in turn affects Langmuir probe measurements as it changes, depending on the degree of magnetisation, the nature of the plasma from which the probe can collect. The following subsection will examine how the different degrees of magnetisation affect probe measurements.

The size of ρ_L (eq. (1.7)) compared to the probe extent L is the key factor in determining how the probe measurements are affected. In the case where the ion and electron Larmor radii ($\rho_{L,i}, \rho_{L,e}$) are both larger than the probe extent, the collection of current occurs mostly the same as in the unmagnetised case, and the standard interpretation of the IV characteristic can be used (as per section 2.3.2) to obtain plasma parameters.

However when this ratio changes and the ordering instead becomes

$$\rho_{L,i} > L > \rho_{L,e} \tag{2.48}$$

the plasma is said to be strongly magnetised. In this case the probe IV characteristic becomes distorted by the magnetic effects, especially in the electron region. This was originally observed through a reduced ion-electron saturation ratio in magnetised plasmas, falling from $\sim (m_i/m_e)^{1/2}$ (~ 40 for hydrogen) to ~ 10 [46] in Bohm's original findings. Values as low as unity have been observed [47]. As the electrons will only be collected from field lines which intersect the probe, the probe is in effect sampling electrons from a flux tube directed along $\mathbf{B}$ with a cross sectional area of $\sim A$ – the probe area (see fig. 2.4). Bohm theorised that as the parallel transport is much larger than the perpendicular transport, the flux tube must extend far into the plasma to balance these fluxes ($\Gamma_{\parallel}$ and $\Gamma_{\perp}$). To overcome finite parallel and perpendicular resistances a potential "hill" structure is formed so as to attract electrons into the flux tube. This in turn decelerates ions which, through the Boltzmann relation, creates an ion density – and thus plasma density – drop in front of the probe. The electron current to the probe is dependent on the plasma density in front of the probe and so leads to the observed decreased electron current. This is not the only explanation however, and a rigorous description of the mechanics which lead to this reduction in electron current has yet to appear, partly due to cross field transport processes being poorly understood.

The reduction in saturation current ratios was found to be because of a distortion of the electron current, with the current collected deviating from an exponential – sometimes quite drastically – above the floating potential. This can result in overestimation of T_e if this region is included in the IV interpretation[20]. However, as this reportedly only affects the electron current and not the ion current, the probe characteristic can still be interpreted in the regions where the electron current is small, i.e. $V < V_{fl}$. This was confirmed experimentally in [45] through the use of a pin-plate probe, whereby the combination of a small floating pin in front of a swept plate probe allowed the measurement of the plasma potential, offset by some constant, at different parts of the IV characteristic. It was found that the plasma potential was stable up until the floating potential was reached, at which point the plasma potential increased monotonically. This finding showed that the plate probe's potential was entirely contained within the plate probe's sheath for $V < V_{fl}$, and therefore the aforementioned potential hill does not form. It was thus concluded that T_e

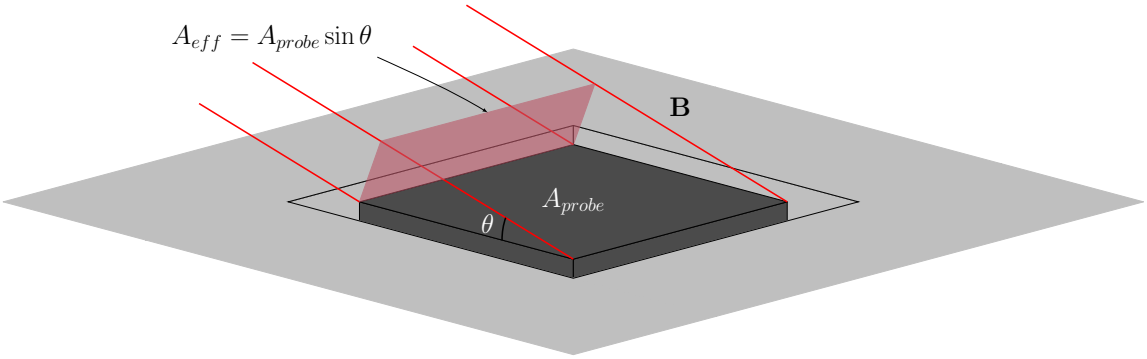

Figure 2.5: A schematic diagram of the effective collection area of a probe in a strong magnetic field. The cross-sectional area of the subtended flux tube is reduced to the projection of the probe's surface area along the magnetic field. This is a simplification that does not account for the size of the sheath in front of the probe, which becomes significant as $\theta \to 0$.

could be reliably measured in this section of the IV characteristic, albeit with uncertainty estimates of up to 15-20%. This region of course also allows the measurements of V_{fl} and n_e, thereby not limiting the measurement of other plasma parameters.

It should be noted that this method of only using a small portion of the electron current to measure the electron temperature, while valid, introduces the unfortunate consequence of being highly reliant on the high energy tail of the electron distribution. As such, any deviation from a standard Maxwellian, or the presence of a second hot electron population, will result in an overestimate of T_e[48]. This is particularly a problem in tokamaks, wherein large temperature gradients can exist between the core and the edge which in some circumstances cannot be properly relaxed back to a standard Maxwellian through collisions. Nevertheless, probe T_e measurements have been compared with other tokamak diagnostics and been found to be in agreement, generally to within a factor of 2[45].

The final regime of magnetisation – very strongly magnetised plasmas – occurs when

$$L > \rho_{L,i} > \rho_{L,e} \tag{2.49}$$

i.e. the probe is larger than the ion Larmor radius. In this regime the ion collection is also dominated primarily by cross-field transport, with the major consequence being for the collection area. It is generally assumed in this case that the probe is only collecting ions

from within the flux tube subtended by the effective probe area, i.e. the probe surface area projected along the magnetic field lines (see fig. 2.5). Consequently the calculation of density must be altered slightly from eq. (2.27) to

$$I_{i,sat} = en_e c_s A_{eff} = en_e c_s A_{probe} \sin\theta \tag{2.50}$$

where A_{eff} is the effective collection area of the probe in the magnetic field and θ is as defined in section 2.4.1. For certain probes this collection area is not quite as simple as this projected area and the accuracy of the extracted plasma parameters can be highly dependent on the exact geometry of the collection area — this will be discussed in section 2.4.3.

At still higher levels of magnetisation ($\rho_{L,i} \sim \lambda_D$), the ions are so confined to field lines that they can no longer be turned in the MPS to be normal to the wall. The MPS therefore disappears, but the Chodura criterion still holds. This has potential implications for models of ion current collection in flush-mounted probes. This degree of magnetisation is expected to be encountered more in higher magnetic fields with lower densities, with higher field devices therefore being more susceptible to this effect. The normalised ion magnetisation parameter, given by

$$\xi = \frac{\rho_{L,cold}}{\lambda_{D,cold}} \tag{2.51}$$

where the subscript $_{cold}$ denotes a value calculated in the cold ion approximation, can be used to quickly compare the machine parameter regimes in which this effect will become important ($\xi \leq 1$). Figure 2.6 shows this for several fusion and magnetic confinement devices.

2.4.3 Flush-mounted Probes and Sheath Expansion

The design requirements of probes necessarily change in the harsh environment of a tokamak with high temperatures, densities and heat fluxes to PFCs. Even in the cooler SOL, probes must be designed in such a way so as to minimise incident heat and particle flux, to both reduce erosion and extend component lifetime. Langmuir probes are therefore routinely implemented in tokamaks either embedded in plasma facing components, such as the divertor, or on reciprocating drives which sample the SOL plasma for short periods of time to limit heat loading. Probes installed in divertor surfaces tend to be mounted flush to the PFC to maximally reduce heat loads and perturbation of the local plasma; such probes are called flush-mounted probes (FMPs). Although practical for implementation, FMPs can be

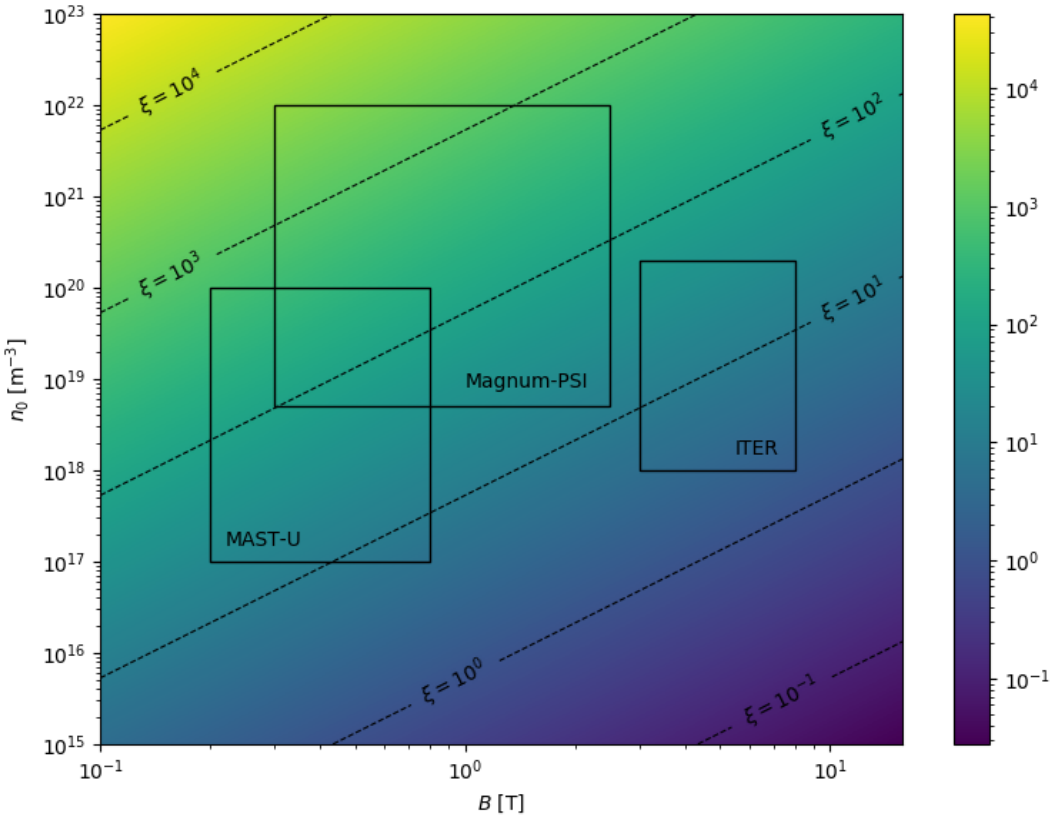

Figure 2.6: Sheath magnetisation regimes for several relevant fusion devices, with dashed lines showing contours of constant magnetisation (ξ). Below $\xi = 10$ magnetisation effects will begin to affect ion collection, and below $\xi = 0.1$ being a strongly magnetised sheath with no MPS. Adapted from [49].

notoriously difficult to interpret accurately.

The magnetic incidence angle to the divertor surfaces in tokamaks is intentionally made as small as possible to reduce the deposited heat flux. For flush-mounted probes in a strongly magnetised plasma, which we can consider most tokamak divertor plasmas to be, this significantly reduces the collection area of the probe. At grazing angles of incidence ($> 10°$) the contribution of the probe surface area to the effective collection area is very small (scales as $\sin\theta$) so the size of the sheath in front of the probe (scales as $\cos\theta$) becomes a much more dominant factor on how much current is collected. The sheath expands depending on the probe voltage according to the Child-Langmuir law[50]. For an

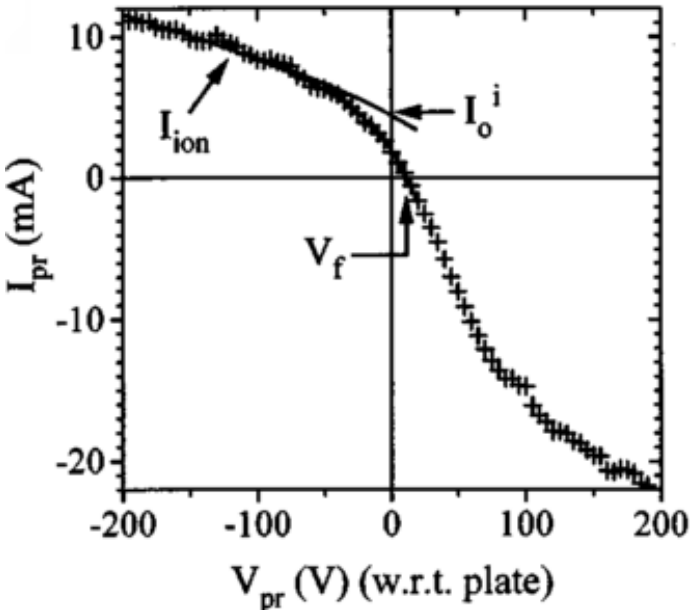

Figure 2.7: Example of an IV characteristic measured in Tokamak de Varennes (TdeV) with grazing magnetic field incidence angle. The ion saturation region does not saturate at a single current, but increases with increasingly negative voltage bias. Taken from [51].

unmagnetised sheath this is given by

$$s = \frac{2\sqrt[4]{2}}{3}\left|\frac{eV_p}{k_B T_e}\right|^{\frac{3}{4}}\lambda_D \tag{2.52}$$

where s is the distance from the probe to the sheath edge, where quasineutrality breaks down. Due to this the ion current does not saturate, but instead grows with increasingly negative voltage as the sheath – and therefore collection area – expands (see fig. 2.7). This is known as sheath expansion.

This phenomenon was observed in Matthews' meticulous study[47] of probe characteristics at different B-field incidence angles, measured on a probe array installed in the limiter of Divertor Injection Tokamak Experiment (DITE). The saturation currents were found to depart from the $\sin\theta$ scaling at very small angles, with the measurements of cross field flux taken at $\theta = 0$ being an order of magnitude larger than expected. It was also found that using the standard 3-parameter model of the IV characteristic, even when utilising voltages below V_{fl}, leads to large overestimation of the extracted T_e.

In a study with the flush-mounted probe system on the Tokamak de Varennes (TdeV), Gunn [51] developed a 4-parameter IV characteristic model whereby the non-saturating ion current could be accounted for with an additional term

$$I_{tot} = I_{i,sat} + \Delta I V_p - I_{e,sat} \exp\left(\frac{eV_p}{k_B T_e}\right). \tag{2.53}$$

Here the additional ΔI term is the gradient of the non-saturating ion current. By assuming a linear fit to the ion saturation region, extrapolating this out to the entire IV characteristic, and then subtracting it, one is left with an exponential IV trace made, in theory, entirely of the electron current. This acts to reduce the overestimation of T_e, as evidenced by the comparison done between this 4-parameter method and the standard 3-parameter method, which produced T_e values which differed by a factor of 2. The reasoning behind this linear fit is to approximate the standard sheath scaling $|V|^{3/4}$, which would be otherwise difficult to discern from noisy probe data. A disadvantage is that the density must be recovered from the approximated linearity and, while this may be accurate for the specifics of the setup on TdeV, this may not necessarily be applicable to other tokamaks.

Efforts have been made to model the size of the sheath in front of a flush-mounted probe, notably by Weinlich and Carlson[52]. Their model, depicted in fig. 2.8, took into account the density drop across the MPS, as described by eq. (2.47), which increases the local Debye length in front of the wall by a factor of $\sin^{1/2}\theta$. The Debye length enhancement must therefore be incorporated into any models of sheath expansion. The sheath in front of the probe was modelled as a rectangular box, with any ions that crossed the Debye sheath boundary collected by the probe as current. As the probe is biased more negatively the box expands upwards into the MPS, but the MPS is always a fixed width – controlled by eq. (2.42) – so the MPS boundary expands equivalently. The collection area of the sheath in this model is therefore the sheath size s and the probe length L projected along $\mathbf{B}$. Two further consequences of this model were the focusing of ions onto the leading probe edge due to the frontal sheath extension, and the existence of a region depleted of ions on the trailing edge, labelled 1 and 2 respectively in fig. 2.8. This phenomenon results in enhanced ion current to the probe with increasingly negative voltage, leading to a non-saturation of ion current.

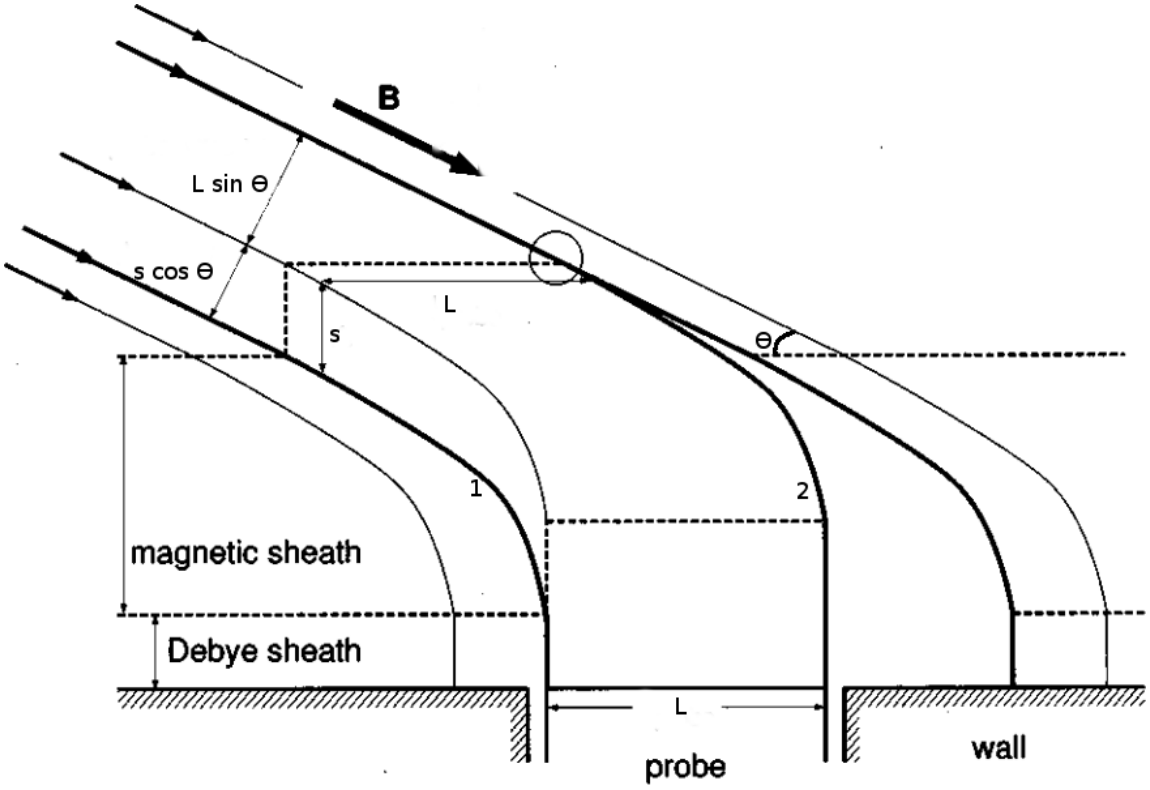

Figure 2.8: Schematic of the flush-mounted probe model developed by Weinlich and Carlson. Taken from [52].

2.5 The Bergmann and Murphy-Sugrue Models

The model presented by Carlson and Weinlich was unfortunately not completely predictive at small angles, presumably because of the lack of finite Larmor orbit effects captured by nature of being a fluid model. A fully kinetic approach was required, as used by Bergmann in two separate computational studies[24, 38] using a 2D particle-in-cell code. Similarly to [52], the sheath was modelled as a rectangular box around the probe, firstly with rounded corners but later with sharp corners. The frontal and lateral expansion of the sheath were considered.

The ion focusing effect predicted by the fluid model was observed in the simulations, and the scaling of the sheath thickness found to follow a modified Child-Langmuir relation

$$\Delta = \Delta_0 + \Delta_1 |V|^{\frac{3}{4}} \tag{2.54}$$

where Δ_0 is the thickness of the sheath in front of the wall, Δ_1 is the coefficient describing the additional sheath thickness introduced by negative potential biasing, and V is the voltage applied to the probe relative to the wall

$$V = \frac{e(V_w - V_p)}{k_B T_e}. \tag{2.55}$$

Several initial simulations were run to calculate the floating potential of the wall, which was held as fixed throughout the simulation. Δ_0 was found to decrease as $\theta \to 0$ as more of the potential drop is taken up by the MPS. Δ_1 on the other hand increases as $\theta \to 0$ due to the MPS density drop, which scales according to

$$\Delta_1 \approx \frac{1}{2} \frac{\lambda_D}{\sin^{1/2}\theta}. \tag{2.56}$$

This represents the change in local Debye length due to the MPS density drop. Bergmann also found that the lateral growth of the sheath, denoted as δ, was also well described by this functional dependence on V and θ. Equations (2.54) and (2.56) can therefore be otherwise expressed, for the frontal sheath expansion, as

$$\Delta - \Delta_0 \propto \frac{\lambda_D |V|^{\frac{3}{4}}}{\sin^{1/2}\theta} \tag{2.57}$$

and equivalently for the lateral sheath expansion as

$$\delta - \delta_0 \propto \frac{\lambda_D |V|^{\frac{3}{4}}}{\sin^{1/2}\theta} \tag{2.58}$$

which will have different constants of proportionality. Note that in Bergmann's derivation, and Murphy-Sugrue's subsequent extension, it is assumed that $\delta_0 = 0$.

This sheath scaling therefore corresponds to a change in the form of the IV characteristic model. It was found that the simulated current trace on the probe was well described by

$$\frac{I}{I_{i,sat}} = 1 + a|V|^{\frac{3}{4}} - e^V \tag{2.59}$$

where V is as described above and a is an angle- and geometry-dependent *sheath expansion parameter*.

The form for a was derived by comparing the ratio of the sheath size of the probe while

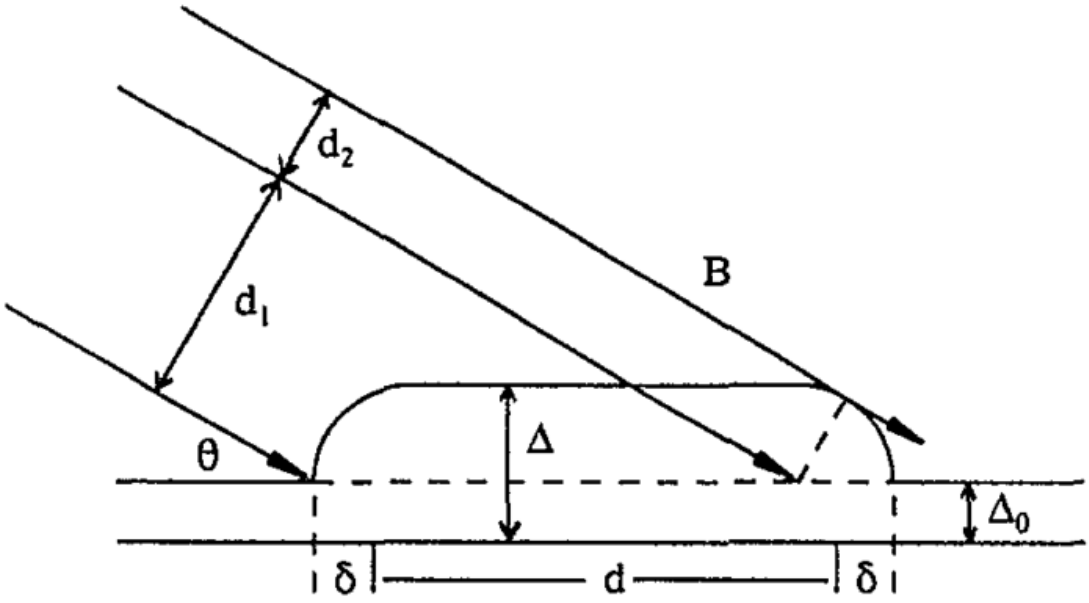

Figure 2.9: Schematic of the sheath modelled by Bergmann using 2D particle-in-cell simulations of a small probe. This model was later adapted to larger, more fusion-relevant probe sizes and found to approximate better with a purely rectangular sheath. Taken from [24].

floating to the sheath size of the probe at some large negative voltage. The probe in both cases was assumed to capture all ions incident on its sheath perimeter, and comparing the ratio of ion currents essentially reduces the problem to the comparison of collection areas in each case, as all other terms will cancel. The collection area in the floating case was assumed to be the probe surface area projected along the magnetic field line, i.e. $A_{probe} \sin\theta$, whereas in the biased case it was assumed to be the projected area of the expanded sheath – labelled as the effective collection area A_{eff} Taking the ratio of these currents and comparing them to the assumed form of the IV characteristic – given by eq. (2.59) – Bergmann obtained an expression for a in terms of θ, the probe length L, and coefficients c_1 and c_2 – which are the constants of proportionality from eqs. (2.57) and (2.58). These coefficients were then measured from fits to simulated IV characteristics.

The precise form of a differed with the assumptions of the sheath shape. The first study,

with the rounded sheath corners (see fig. 2.9), derived a value of a as

$$a = \frac{0.5 + 0.4\big(\sin^{-1}\theta - 1\big)}{\sin^{1/2}\theta}\frac{\lambda_D}{L} \tag{2.60}$$

where the fractions of 0.5 and 0.4 were found by fitting to simulated IV characteristics. L in this case is the probe length. The second study, which utilised larger probes ($L \gg \rho_{L,i} \sim 400\lambda_D$) and a rectangular sheath, re-derived this equation as

$$a = \frac{c_1 + c_2\cot(\theta)}{\sin^{1/2}(\theta)}\frac{\lambda_D}{L} \tag{2.61}$$

where c_1 and c_2 represent the coefficients for the frontal and lateral sheath scaling. These were found to be slightly changed from the first set of simulations, with $c_1 = 0.5$ and $c_2 \to 0.6$ with increasing probe length. This equation was found to closely match the results of probe measurements taken on the Axially Symmetric Divertor Experiment Upgrade (ASDEX-Upgrade) tokamak.

This study was then repeated by Murphy-Sugrue for MAST-like probes, which have much larger gaps either side between the probe and the floating wall[53]. This study confirmed the results of Bergmann's work before expanding the sheath model used to incorporate these gaps, resulting in an expression for a very similar to eq. (2.61) but with L replaced with $L + g$, i.e.

$$a = \frac{c_1 + c_2\cot(\theta)}{\sin^{1/2}(\theta)}\frac{\lambda_D}{L + g} \tag{2.62}$$

where g is the size of the gap. For MAST probes with $L = 5mm$ and $g = 1mm$, inclusion of these gaps results in a 20% increase of the collection area. Murphy-Sugrue also found slightly altered values for c_1 and c_2 as 0.9 and 0.6 respectively, with c_2 found similarly to depend on the probe length and 0.6 being the value tended to as probes are made longer.

2.6 Summary

This chapter has presented the theoretical background required to study probes in tokamaks. A 1D description of Debye shielding was introduced, with the Debye length in the cold and hot ion approximation defined. A similar 1D treatment of an unmagnetised sheath in front of a surface was then used to derive the Bohm criterion, and infer the existence of an accelerating pre-sheath with a finite electric field. The implications for this criterion on

the particle fluxes to a surface biased to different potentials were then explored and thus the theory for an ideal Langmuir probe laid out. The changes made to these derivations through the introduction of a magnetic field were then presented, with a description of the magnetic pre-sheath and a discussion of the existence of a critical angle. The complications that arise in interpreting Langmuir probes in magnetic fields were then described, with the inclusion of various models for explaining some of the phenomena that arise. The extension and further exploration of models for Langmuir probes in strong magnetic fields are studied through particle-in-cell simulations in chapter 5. An experimental investigation of the effects of magnetic field incidence angle on flush-mounted and angled-tip Langmuir probe measurements is presented in chapter 6.

Chapter 3

Computational Methods

3.1 Introduction

Simulations are a crucial tool available to scientists to study the universe and predict the behaviour of complex phenomena. Alongside theory and experiment, they constitute one of the three major approaches to the modern practice of physics. Since the 1960s computational power has increased by orders of magnitude, and consequently so has the usefulness of computational physics.

In the fusion community, a plethora of techniques for simulating plasmas have arisen, ranging in scope from simulating the tiny volumes of plasma directly in front of the wall, up to simulating a whole tokamak. These techniques are specifically tailored to the problems they are trying to solve; some are intended to help design new reactors, to predict the efficacy of heat exhaust mitigation techniques, or to foresee unstable areas of parameter space. In general there are five main families of codes in use by the fusion community to study plasmas: fluid codes, kinetic codes, hybrid codes, gyrokinetic codes and particle codes. Of these, the particle method is considered the most fundamental as the fewest assumptions are made — it provides a full description of the system down to the particle level and the fields calculated are self-consistent. As such this is the technique of choice to simulate Langmuir probes and interrogate the sheath as no conditions are placed on the distribution functions. Additionally, quasineutrality is not enforced and so its breakdown – the characteristic property of the sheath – can organically emerge from the simulation conditions.

3.2 The Particle-in-cell Method

As pioneered by Morse [54], the particle method, also known as particle-in-cell (PIC), involves discretising the simulation domain and field quantities onto a grid. The superparticles are free to move anywhere within this grid, but their charge is "weighted" onto the grid points they are nearest to to calculate charge density. This grid is commonly rectangular for simplicity, as is the case in SPICE, but can be any arbitrary shape assuming that the weighting function properly accounts for this. From the charge density, the electric potential can be calculated through Poisson's equation – solved using numerical methods. The gradient of the electric potential can then be used to calculate the electric field, which in turn can be used to "push" the particles by integrating their equations of motion. To get the value of the electric field at each superparticle's position, the field is interpolated

back to the particle positions according to the same weighting used to calculate the charge density. Once the particles are pushed into new positions over some time step Δt, any which move outside of the simulation domain – either outside the grid or onto some surface – are removed from the simulation. New particles are then injected into the simulation to conserve plasma density. The process can then start again, with the new particle positions interpolated back onto the grid to calculate charge density. This process is repeated some number of time steps until the requisite amount of total time has been simulated.

Several other optional steps can be inserted into the process to include a greater range of physical phenomena, such as collisions, heat diffusion, secondary electron emission etc., but the above is the minimum required process to simulate plasma using the PIC method. Note that the PIC method generally maintains all velocity dimensions regardless of spatial dimensionality. Thus a 2D PIC simulation is more correctly termed a 2D3V simulation.

3.2.1 Superparticles

The collection of individual particles together into superparticles allows for capturing the relevant physics of plasmas with far fewer particles than there are in a real plasma. This reduction in number of particles comes at a cost however, as there is a trade-off with number of particles and statistical noise. Therefore, large numbers of particles are still required to run a meaningful simulation and this restricts particle codes to looking at small regions of plasma compared to the other approaches.

Each superparticle is comprised of the same number of its constituent species and has the same charge-to-mass ratio as an individual particle, so it follows the same trajectory as an individual particle through the simulation window. That is to say that a superparticle, constituted of K particles, has a mass of $m_s = Km_p$ and a charge of $q_s = Kq_p$, where the subscripts $_s$ and $_p$ denote the superparticle and particle respectively. The number of particles in each superparticle changes based on implementation and simulation dimensionality, but the total number of particles in the simulation must remain high enough to capture the relevant physics involved. The metric for this, as described by Birdsall & Langdon [55], is the number of particles in a Debye cube (for a 3D plasma) - N_D. They quote a value of $N_D = 10$ as sufficient to satisfy the condition that the thermal kinetic energy of the plasma (KE) be much greater than the microscopic potential energy (PE), i.e. that the plasma constituents are moving fast enough that they will not recombine and neutralise. For reference, in a laboratory plasma where, if we take reasonable MAST-U divertor-like

parameters of $n_e = 1 \times 10^{18}$ and $T_e = 10eV$, the number of particles in the Debye cube is $\sim 1.3 \times 10^4$. Despite having far fewer particles in the Debye cube, we can still effectively simulate plasmas through the use of superparticles. From here onward, superparticles will be referred to in shorthand as particles.

3.2.2 Charge Density and Weighting

The process by which the particles are interpolated onto the discretised grid to calculate charge density, along with the reverse of this process to interpolate the electric field to particle position for pushing, is called *weighting*. The standard method used in PIC codes for doing this is the PIC bilinear approach[56] (or the similar cloud-in-cell approach[57]), wherein the particles are treated as clouds of uniform charge ~ 1 cell wide and with a tapered charge density profile. The charge density is therefore deposited onto the corners of the cell it is inside. In the case of a 2D simulation this would be to the four corners of the rectangular cell, in 3D the 8 corners of the cuboid cell.

If we consider the 2D case, this is done by dividing the cell into 4 through the particle position, with the area of each quadrant being the weighting applied to the opposite corner grid node (see fig. 3.1). If we take the ith particle, in position $\mathbf{r}_i = (y_i, z_i)$, with charge q_i, within the grid space defined by $n, n+1, m, m+1$ and grid spacing $\Delta y = \Delta z = \lambda_D$. We can re-express $\mathbf{r}_i$ as the relative position of the particle within the cell, $\mathbf{r}_{i,rel} = (y_{i,rel}, z_{i,rel}) = (y_i - n, z_i - m)$, making areas of the 4 quadrants (as depicted in fig. 3.1):

$$\begin{aligned} A_1 &= (1 - y_{i,rel})(1 - z_{i,rel}) \\ A_2 &= (1 - y_{i,rel}) z_{i,rel} \\ A_3 &= y_{i,rel}(1 - z_{i,rel}) \\ A_4 &= y_{i,rel} z_{i,rel} \ . \end{aligned} \tag{3.1}$$

Note that these areas are all normalised to the area of the cell, in this case λ_D^2 but in general $\Delta y \Delta z$. In a 1D case this becomes the normalised distance to the point in question, and in 3D the normalised octant volume. These weights contribute to the charge density by multiplying each by the charge of the particle in question q_i, with the process carried out for each particle and all contributions summed onto each grid point to get the charge density grid $\rho(y, z)$.

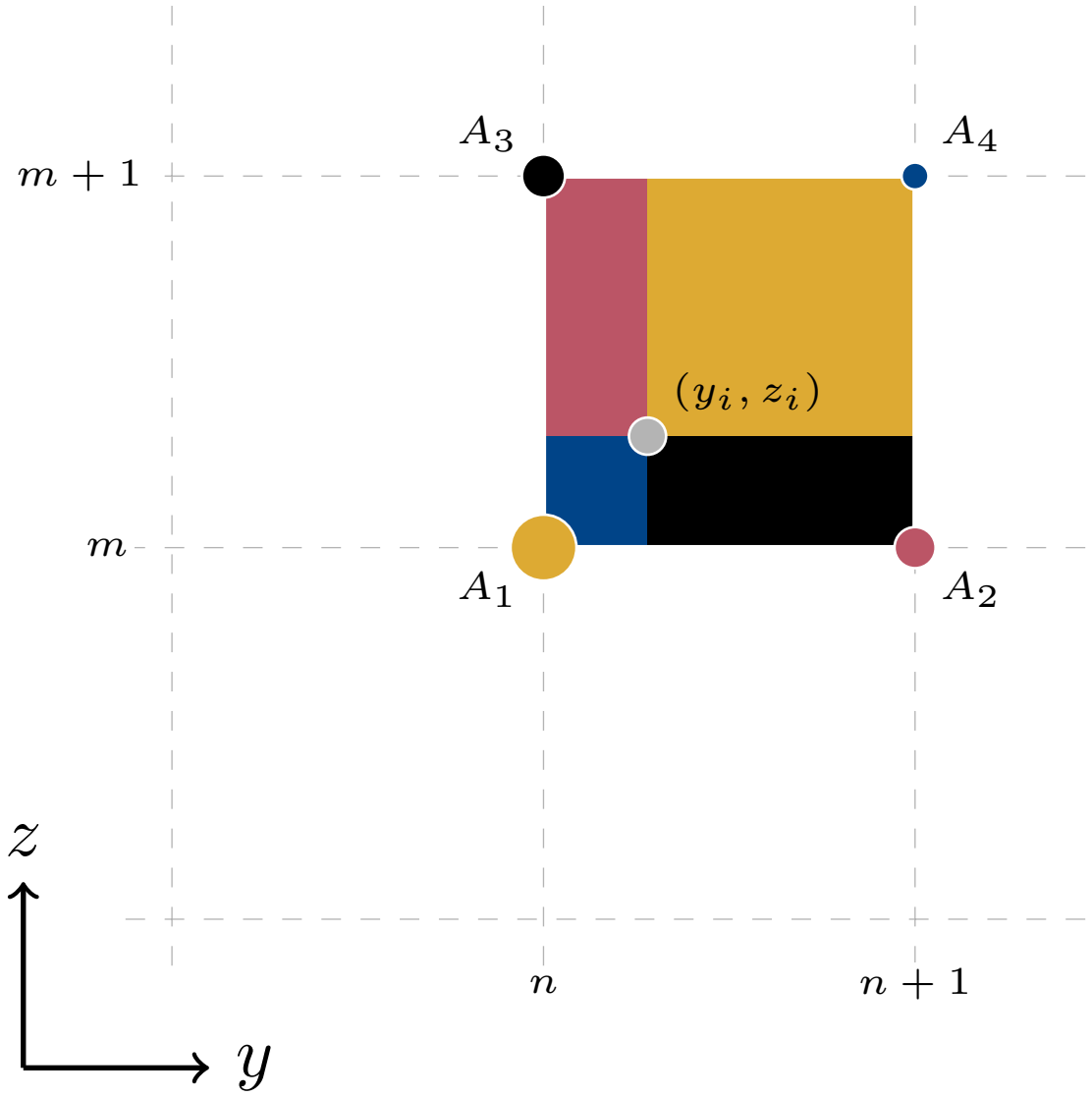

Figure 3.1: Diagram showing particle-in-cell bilinear weighting through splitting of the grid cell into quadrants. The weighting applied to each grid point – at each corner of the cell – is given by the area of the quadrant on the opposite side of the particle. In this case the grid point (n, m) sees the largest contribution to charge density from the shown particle, as it is closest to it, with the weighting given by the area A_1 (in yellow).

The method of weighting also has an effect on the size and shape of the particle being simulated. For example, the first order method results in a linearly increasing and

decreasing shape exactly $2\Delta x$ wide (hence bilinear). In a 1D simulation, particles in this first order method appear to the grid as a triangular shaped cloud of charge. This is of interest because the use of a grid, and the weighting that accompanies, naturally results in us simulating particles of finite size as opposed to the point charges found in a real plasma. This fundamentally changes how the particles interact with one another, as a finite sized particle will not undergo a $1/r$ or $1/r^2$ repulsion (as a point charge would in 2 or 3 dimensions) but will instead exert less force on other particles as they overlap. This results in a system whereby collisions are greatly reduced, which must be countenanced if we are to emulate real plasma behaviour. However, given that we are operating with relatively fewer particles (recall that $N_D \sim 10$ from section 3.2.1) and therefore operate with less available charge screening, the decrease in collision frequency helps to stop those collisions from pushing us into a non-relevant regime[58].

3.2.3 Potential and Electric Field

Once we have distributed charge density and have a discretised representation of ρ, we can use this to solve Poisson's equation and therefore arrive at the electrostatic potential. Poisson's equation is given by:

$$\boldsymbol{\nabla}^2\phi = -\frac{\rho}{\epsilon_0} \tag{3.2}$$

where ϕ is the electrostatic potential and ϵ_0 is the permittivity of free space. Finite differencing is used in SPICE.

The finite difference equations are an approximation of the derivative of a function, derived by evaluating the Taylor expansion of that function at some value x plus some finite Δx

$$f(x+\Delta x) = f(x) + \Delta x\frac{\partial f(x)}{\partial x} + \frac{\Delta x^2}{2!}\frac{\partial^2 f(x)}{\partial x^2} + O(x^3). \tag{3.3}$$

If we then evaluate the function in the reverse direction, i.e. at $x - \Delta x$

$$f(x-\Delta x) = f(x) - \Delta x\frac{\partial f(x)}{\partial x} + \frac{\Delta x^2}{2!}\frac{\partial^2 f(x)}{\partial x^2} + O(x^3) \tag{3.4}$$

we then have two equations which can be combined to give $\frac{\partial f(x)}{\partial x}$ in terms of the original function. Subtracting eq. (3.4) from eq. (3.3), rearranging, and then omitting the third-order term to ensure second-order accuracy, we get the finite difference approximation of the first

derivative for a 1D function

$$\frac{\partial f(x)}{\partial x} = \frac{f(x+\Delta x) - f(x-\Delta x)}{2\Delta x}. \tag{3.5}$$

Similarly, for the second derivative we can add eqs. (3.3) and (3.4) together to get

$$\frac{\partial^2 f(x)}{\partial x^2} = \frac{f(x+\Delta x) - 2f(x) + f(x-\Delta x)}{(\Delta x)^2}. \tag{3.6}$$

These have similar forms for higher dimensionality.

If we consider a 1D PIC simulation attempting to solve eq. (3.2), the $\boldsymbol{\nabla}^2\phi$ becomes $\frac{\partial^2\phi}{\partial x^2}$ and we can use eq. (3.6), replacing the $x \pm \Delta x$ with the value of ϕ at neighbouring grid positions:

$$\frac{\partial^2\phi}{\partial x^2} = \frac{\phi_{n+1} - 2\phi_n + \phi_{n-1}}{(\Delta x)^2} = -\frac{\rho_n}{\epsilon_0} \tag{3.7}$$

where Δx is now the grid spacing. This is a set of N coupled linear equations which can be solved to find ϕ at each of the N grid points. Note that the potential at a grid point n is also dependent on grid points $n \pm 1$. If we introduce two boundary conditions for the edges of the domain it becomes soluble (boundary conditions will be discussed in section 3.2.6). The N coupled equations can be written in matrix form[55] as

$$\begin{pmatrix} -2 & 1 & & & & \\ 1 & -2 & 1 & & & \\ & 1 & -2 & 1 & & \\ & & \ddots & \ddots & \ddots & \\ & & & 1 & -2 & 1 \\ & & & & 1 & -2 \end{pmatrix} \begin{pmatrix} \phi_1 \\ \phi_2 \\ \phi_3 \\ \vdots \\ \phi_{N-1} \\ \phi_N \end{pmatrix} = -\frac{(\Delta x)^2}{\epsilon_0} \begin{pmatrix} \rho_1 \\ \rho_2 \\ \rho_3 \\ \vdots \\ \rho_{N-1} \\ \rho_N \end{pmatrix}. \tag{3.8}$$

We know the value of ρ at every grid point, so this matrix equation must now be solved to find the value of ϕ at every grid point. This can be achieved through various numerical methods, usually grouped into direct solvers and iterative solvers. The best of these to use is usually dependent on the specifics of the simulation. For example the direct solver in SPICE should generally not be used when running 3D simulations due to the excessive memory requirements.

Once a solution has been found to eq. (3.8), the resulting ϕ is used to calculate $\mathbf{E}$

through the gradient of the electrostatic potential

$$\mathbf{E} = -\boldsymbol{\nabla}\phi. \tag{3.9}$$

In our 1D example this becomes

$$E = -\frac{\partial\phi}{\partial x} \tag{3.10}$$

which can be straight-forwardly approximated by using eq. (3.5)

$$E_n = -\frac{\phi_{n+1} - \phi_{n-1}}{2\Delta x} \tag{3.11}$$

as ϕ is now known at every grid point.

3.2.4 Particle Pusher

Now the electric field is known, the particles can be pushed by separately integrating the two equations of motion: the Newton-Lorentz equation and the velocity:

$$m_i \frac{\mathrm{d}\mathbf{v}_i}{\mathrm{d}t} = q_i(\mathbf{E} + \mathbf{v}_i \times \mathbf{B}) \tag{3.12}$$

$$\mathbf{v}_i = \frac{\mathrm{d}\mathbf{r}_i}{\mathrm{d}t} \tag{3.13}$$

where $\mathbf{v}_i$ and $\mathbf{r}_i$ are the velocity and position of the ith particle respectively. The principle of pushing the particles draws parallels from the field calculations, except time is discretised instead of space and a form of finite differencing is used to integrate over Newton's equations of motion at that discretised time. The leap-frog method is most commonly used and frequently implemented using the Boris method[59], which is both computationally efficient and stable over many time steps[60].

The leap-frog method involves separately integrating the above two differential equations at offset time steps; each time step Δt is split in half with the position being known at integer values of t and the velocity being known at half integer values of t. The value of position at time t can therefore be calculated from the velocity at $t - \frac{\Delta t}{2}$ and the velocity at $t = t + \frac{\Delta t}{2}$ can be calculated from the position at time t. This can be repeated as many times as necessary for as long as the desired simulation length. This does require that the initial velocities ($\mathbf{v}_i(t = 0)$) be moved back to $t = -\frac{\Delta t}{2}$ to ensure the two values are correctly centred. We can therefore rewrite eqs. (3.12) and (3.13) in finite differencing form

using eq. (3.5) and the discretised time offset by $\Delta t/2$

$$\frac{\mathbf{r}_{t+\Delta t} - \mathbf{r}_t}{\Delta t} = \mathbf{v}_{t+\Delta/2} \tag{3.14}$$

$$\frac{\mathbf{v}_{t+\Delta t/2} - \mathbf{v}_{t-\Delta t/2}}{\Delta t} = \frac{q}{m}\left[\mathbf{E}_t + \left(\frac{\mathbf{v}_{t+\Delta t/2} + \mathbf{v}_{t-\Delta t/2}}{2}\right) \times \mathbf{B}_t\right] \tag{3.15}$$

where the subscripts denote at what time step the values are taken from, and the velocity in the magnetic term has been t-centred by averaging $\mathbf{v}_{t-\Delta t/2}$ and $\mathbf{v}_{t-\Delta t/2}$. Note that $\mathbf{E}$ and $\mathbf{B}$ are interpolated to each particle's position through the reverse of the weighting process described in section 3.2.2. These can thus be solved in turn for each particle in the system, with eq. (3.15) solved for $\mathbf{v}_{t+\Delta t/2}$ (the new particle velocity) and then substituted into eq. (3.14) for $\mathbf{r}_{t+\Delta t}$ (the new particle position).

The solution for $\mathbf{v}_{t+\Delta t/2}$ from eq. (3.15) can be obtained, via the Boris method, through several steps. If we make the following substitutions

$$\mathbf{v}_{t-\Delta t/2} = \mathbf{v}^- - \frac{qE}{m}\frac{\Delta t}{2} \tag{3.16}$$

$$\mathbf{v}_{t+\Delta t/2} = \mathbf{v}^+ + \frac{qE}{m}\frac{\Delta t}{2} \tag{3.17}$$

where $\mathbf{v}^+$ and $\mathbf{v}^-$ are intermediate dummy variables, then we are left with

$$\frac{\mathbf{v}^+ - \mathbf{v}^-}{\Delta t} = \frac{q}{2m}\left(\mathbf{v}^+ + \mathbf{v}^-\right) \times \mathbf{B}_t \tag{3.18}$$

which is a rotation of $\mathbf{v}$. We can therefore use eq. (3.16) to apply half of the electric impulse to obtain $\mathbf{v}^-$, rotate with eq. (3.18) to obtain $\mathbf{v}^+$, and finally apply the other half of the electric impulse to arrive at $\mathbf{v}_{t+\Delta t/2}$.

3.2.5 Stability Conditions

All of these calculations are dependent on the choice of Δt and Δx for stability. There is an error in the leap-frog technique that zeroes out as $\Delta t \to 0$, but clearly we must use a finite value of Δt. There are however some constraints upon how large it can be. Firstly, to ensure stability in the leap-frog algorithm, we require

$$\omega_p \Delta t < 2 \tag{3.19}$$

where $\omega_p = \sqrt{\frac{e^2 n_e}{\epsilon_0 m_e}}$ is the plasma frequency. Birdsall[55] finds that the LHS reduces further to 0.2 if accurate results are to be obtained.

Secondly, the grid spacing Δt is upper bounded at 1 λ_D. This is to ensure the simulation resolves the shielding effects across this length scale, anything larger will result in the electrons undergoing non-physical, numerical heating until this condition is satisfied. The Debye length therefore represents the largest possible grid resolution and any potential structures must be smaller than this to be resolved.

A final condition is placed upon the combination of Δt and Δx, whereby they should be large enough that the fastest moving particle in the system cannot move further than 1 grid cell in 1 time step. Formally

$$\Delta x > v_{max} \Delta t \tag{3.20}$$

which is a form of the Courant-Friedrich-Lewy condition[61, 62].

3.2.6 Boundary Conditions and Particle Injection

Practically speaking, it is not feasible to simulate large volumes of fusion plasma with a PIC simulation – the computational cost limits us to small regions on the order of 100-1000 Debye lengths in width. Thus we must choose carefully what the conditions along the boundary of the simulation are so as to not alter the physics being observed in the bulk.

As mentioned in section 3.2.3, the finite difference solution to Poisson's equation in 1D (eq. (3.7)) requires the simultaneous solving of N equations – where N is the number of grid points along our domain. As each grid point is dependent on the grid points directly either side of it, we get $N-2$ equations with three unknowns and two, corresponding to the points at either end of the domain, with only two unknowns each. We therefore cannot solve this set of equations without some value to give to the neighbours of grid points ϕ_1 and ϕ_N. There are two broad approaches to this: periodic and fixed. SPICE uses a combination of both.

The periodic approach imposes that $\phi_1 = \phi_N$, causing the domain to loop back on itself. The simulation is then effectively modelling an infinite line of concatenated grid points, allowing more fundamental continuous behaviour to be examined. This imposes the condition that the system have no net charge. It also allows the use of a spectral approach to solve Poisson's equation as the charge density can now be Fourier transformed and converted to ϕ in k-space.

The fixed boundary approach requires some quantity at the boundary to be set to some

known value. There are three typical ways this is done:

Dirichlet – the potential at the edge is assigned some function, usually constant, e.g. $\phi_1 = \phi_N = 0$

Neumann – the gradient of the potential (i.e. the electric field) is assigned some function

Cauchy – both the Dirichlet and Neumann boundary conditions are assigned simultaneously

Any of these solutions will make Poisson's equation solvable. Note that different boundary conditions can be imposed on different boundaries depending on the specifics of the system being simulated.

As particles move freely about the simulation, their behaviour at the domain boundary must also be accounted for. The particles can treat the boundaries as periodic, in which case they move freely from cells at the boundary edge into the opposite boundary cells. As in the case of the periodic field boundary conditions, this effectively makes the plasma infinite in the dimension of periodicity. The alternative is for the boundary to be a "sink", whereby any particle which moves across the boundary is removed from the simulation. Presence of these boundary conditions necessitates the reinsertion of particles through injection, to maintain plasma density. This condition can also be applied to arbitrary cells in the domain to represent objects inserted into the plasma, for example a vessel wall or a probe. If that is the case then the removed particle can be recorded to measure incident current to that object, or adjust its potential.

An additional boundary type specific to particles is that of a particle source. This acts to load particles into the system to conserve plasma density, with velocities according to some source velocity distribution. This is done continuously throughout the simulation as an additional step with the PIC cycle. The conservation of particle density is achieved through injection at a rate proportional to how quickly the particles move across the domain. This is dependent on the size of the cells, the length of the time step and the mass of the species.

The velocity distribution can be chosen arbitrarily to reflect the physics of the plasma intended to be simulated. For simulations of the sheath, the injection boundary is analogous to the plasma bulk, and the velocity of injected particles is therefore usually sampled from a Maxwellian to reflect this. The injection boundary is usually also a sink. In the case of a magnetised plasma, care must be taken to ensure that the particles can gyrate around

the field lines appropriately upon injection without being removed from the simulation. A buffer injection zone is usually used to prevent this and therefore preserve the desired velocity distribution.

3.3 SPICE

The Sheath Particle In Cell (SPICE) codes are a family of parallelised 2D3V and 3D3V collisionless PIC codes specialised in investigating behaviour at the plasma-surface interface, i.e. the sheath. It was developed jointly by J. P. Gunn and R. Dejarnac [49, 63–65] to investigate particle deposition into gaps between PFC tiles. It has subsequently been developed by both M. Komm [25, 66, 67] and A. Podolnik [68, 69]. As a code designed to simulate the sheath, it is uniquely placed to investigate Langmuir probe behaviour. This section will briefly break down the implementation of various parts of the PIC process outlined in section 3.2, as well as some of the unique features of the code and its use in this body of work.

3.3.1 Key Features

SPICE has several key features that benefit the investigation of the sheath, but limit the range of possible scenarios accordingly. The code uses a rectangular/cuboid grid shape and a static, homogeneous magnetic field throughout the simulation domain. It is collisionless, and has a unique particle injection scheme which accurately recreates the velocity distribution of ions and electrons at the entrance to the sheath.

The simulation is controlled by four core input parameters which specify the plasma parameters. The first of these is the magnetisation parameter

$$\xi = \frac{\rho_L}{\lambda_D} \tag{3.21}$$

where ρ_L is the Larmor radius (eq. (1.7)). This gives a measure of the Larmor radius in normalised units. The second is the temperature ratio

$$\tau = \frac{T_i}{T_e} \tag{3.22}$$

where T_i and T_e are the ion and electron temperatures respectively. The third is the mass

ratio

$$\mu = \frac{m_i}{m_e} \tag{3.23}$$

where m_i and m_e are the ion and electron mass respectively. This is commonly set to values lower than the real value of ∼1836 for protons and electrons as it significantly speeds up the simulation while maintaining the relevant physics. $\mu = 200$ is generally considered appropriate[41], except when simulating particularly low angles of magnetic field incidence[24]. The fourth major input parameter is the magnetic field orientation

$$\boldsymbol{\alpha}_B = \begin{pmatrix} \alpha_{xz} \\ \alpha_{yz} \end{pmatrix} \tag{3.24}$$

where α_{xz} and α_{yz} are the components of the magnetic field in the x-z and y-z planes respectively (see section 3.3.3 for coordinate system).

There are other input parameters to specify the simulation size (L_y, L_z) and grid spacings $(\Delta y, \Delta z)$ in each dimension. The number of particles per cell N_{PC} is also an explicit input.

The physical quantities of the simulation are normalised, as is common practice in computational physics, to minimise the rounding errors associated with floating point operations on numbers with different orders of magnitude. The normalisations in SPICE are:

$$\text{Time step} \quad \hat{\Delta t} = \omega_{c,i}\Delta t \tag{3.25}$$

$$\text{Distance} \quad \hat{L} = \frac{L}{\lambda_D} \tag{3.26}$$

$$\text{Potential} \quad \hat{V} = \frac{eV}{k_B T_e} \tag{3.27}$$

$$\text{Density} \quad \hat{n}_s = \frac{n_s}{n_0} \tag{3.28}$$

$$\text{Velocity (particle)} \quad \hat{\mathbf{v}}_p = \frac{\mathbf{v}_p}{\lambda_D \omega_{c,i}} \tag{3.29}$$

$$\text{Mass (particle)} \quad \hat{m}_p = \frac{m_p}{m_{i,main}} \tag{3.30}$$

$$\text{Charge (particle)} \quad \hat{q}_p = \frac{q_p}{q_{i,main}} \tag{3.31}$$

where $\omega_{c,i}$ is the ion cyclotron frequency (eq. (1.6)), and n_0 is the density at the sheath

entrance. There can be any number of species in a SPICE simulation, but their quantities are normalised to the 'main' ion species – as designated in the input file.

There is an additional measure of time – the ion travel time – which is used as an input to denote the total desired simulation time. It is a measure of the time taken for an ion to cross the simulation domain in the z-dimension:

$$t_{z,trav} = \frac{L_z}{v_{i,\parallel} \sin \alpha_B} \tag{3.32}$$

where $v_{i,\parallel}$ is the ion thermal velocity parallel the magnetic field. Simulations must be run so as to reach a saturation of the particle count, which was found to require $t_{sim} \approx 2t_{z,trav}$. However, as $t_{z,trav}$ is also dependent on θ – the angle of magnetic field incidence – we find that $t_{sim} \to \infty$ as $\alpha_B \to 0$, making the study of grazing θ computationally expensive.

3.3.2 Collisionless Condition

The code is collisionless, i.e. there is no implementation of collisions between particles. This means that any plasmas simulated must also be classified as collisionless through the following two criteria:

Mean free path – the mean free path of particles within the system (L_{mfp}) must be larger than the total system size (L). L is defined in this case as the traversal distance of an ion across the simulation window $L_{z,trav}$, which we can calculate from eq. (3.32).

Frequency – all characteristic frequencies of the plasma should be larger than the collision frequency. The largest frequency tends to be ω_c.

The collision frequency is defined as

$$\nu_{coll} = \frac{\pi e^4 n_0}{(4\pi\epsilon_0)^2 m^{1/2} (k_B T_e)^{3/2}} \ln \Lambda \tag{3.33}$$

where $\ln \Lambda$ is the Coulomb logarithm representing the maximum impact parameter. From this we can define the mean free path as

$$L_{mfp} = \frac{v_{th}}{\nu_{coll}} \tag{3.34}$$

and are therefore equipped to check the collisionless conditions of the plasmas. Running these calculations for the representative MAST-U divertor-like plasma ($n_e = 1 \times 10^{18}$

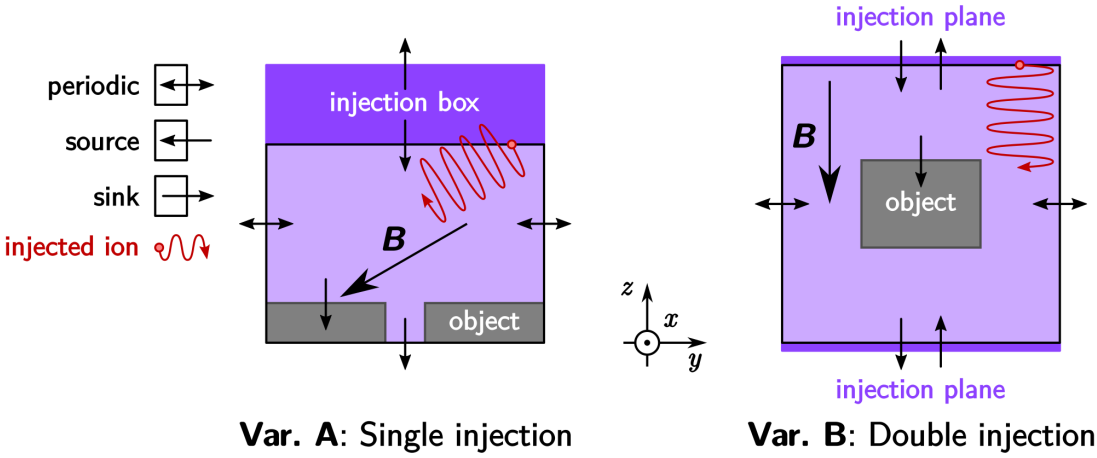

Figure 3.2: The injection scenarios available in both SPICE-2 and SPICE-3. In both cases the side boundaries of the simulation are periodic and the top and bottom are particle sinks. Objects can be placed in the simulation domain and are treated as particle sinks. *(left)* Variation A has a single injection box at the top of the domain which allows particles to be injected at any arbitrary angle without being immediately removed from the simulation by the sink lining the top boundary. *(right)* Variation B is available when **B** is normal to the injection plane. Particles can be injected from the top and bottom of the simulation domain. Taken from [70].

and $T_e = 10eV$), taking $\ln\Lambda = 13$, we arrive at $L_{mfp} = 5 \times 10^4 \lambda_D$ for electrons. From Bergmann[38], a reasonable estimate for the size of a large Langmuir probe is $d = 600\lambda_D$, which is two orders of magnitude lower and therefore gives ample collisionless simulation space around the probe tip.

3.3.3 Simulation Scenarios

All SPICE simulations start empty of particles. They are populated over several $t_{z,trav}$ through continuous particle injection from the injection boundary or boundaries. SPICE has two main injection scenarios (see fig. 3.2):

Variation A – injection from the top of the simulation domain ($z = L_z$). As per section 3.2.6, this injection boundary has an "injection box" which extends $\sim \rho_L \cos\alpha_B$ past the simulation domain boundary to allow for injected particles to gyrate about the magnetic field. The particle boundary at the top of the injection box is a sink.

Both side walls ($y = 0, y = L_y$) are periodic for both particles and field calculations and the bottom acts as a particle sink. The field boundaries at the top and bottom are Dirichlet.

Variation B – injection from the top and bottom of the simulation domain ($z = 0, z = L_z$)
This variation is only available when **B** lies in z, and therefore requires no injection box as gyromotion is purely in the y-x plane. All field and particle boundary conditions are otherwise the same as Variation A.

Both variations feature the option to place objects into the simulation domain, which act as particle sinks. Variation A was intended to be used to simulate the interactions at the plasma-surface interface, and so objects are generally placed on the bottom of the simulation domain to replicate wall tiles or probes.

SPICE can use any arbitrary velocity distribution to determine injected particles' initial velocities. Two default options are available, a Maxwellian distribution and a Chung-Hutchinson distribution[71], the latter of which has several variations depending on the input value of τ, ranging from 0.1 to 5.0. The particle velocity is distributed differently along different components of the magnetic field. The parallel component is modified according to previously run 1D pre-sheath simulations [72], and the perpendicular components are Maxwellian, with the gyromotion phase uniformly distributed. Particles are randomly distributed in space along y (and x in 3D), and randomly in z within the injection box limits. The particles are also given a random deviation parallel to the magnetic field to prevent artificial modes.

The use of a Chung-Hutchinson distribution function, the predicted distribution of ions having been accelerated by the pre-sheath, constitutes one of the major reasons SPICE is well suited to simulating the sheath. It allows the effects of the pre-sheath to be included but not explicitly simulated, drastically reducing computational complexity.

3.3.4 Langmuir Probes

SPICE is uniquely suited to running simulations of Langmuir probes as it has the ability to simulate swept voltage and therefore IV characteristics. Objects can be placed in the simulation domain in 'swept' mode, which will force the simulation to sweep the potential of the probe between two preset values. By default these values are $-10\hat{V}$ and $10\hat{V}$, with steps of $0.05\hat{V}$, but this can be altered. SPICE leaves at least $200\Delta t$ time steps to allow

the plasma to adjust to the new bias voltage on the probe object. This bias voltage sweep should only be started after the simulation has reached saturation.

This feature can be combined with the current diagnostic inherent to SPICE objects, whereby the particles crossing into simulation cells designated as 'probe' are counted in a time series. The currents to objects from different species are tracked independently, so separate ion and electron currents can be extracted and analysed. This is particularly useful when evaluating the enhancement of ion current to the probe due to sheath expansion. The currents to objects in the simulation domain can also be used to track the state of particle saturation of the simulation and therefore decide the value of t_{sim}.

If both the bias voltage on the probe, and the current collected at that voltage are known, then an IV characteristic can be extracted from the simulation. The time varying quantities (t, I_e, V) are binned across each voltage step. To remove the values measured during the plasma's reaction to the voltage change, the former half ($100\Delta_t$) are discarded and the latter half averaged to get a single value for each time varying quantity at that particular voltage step. This averaging results in a relatively smooth IV characteristic which can be fit or otherwise interpreted as necessary.

The current values are normalised by

$$\hat{I} = \left(\frac{\hat{\Delta} t}{eK\omega_{c,i}} \right) I \tag{3.35}$$

where $\hat{\Delta} t$ is the normalised time step in the simulation, K is the number of particles in each superparticle as given by the number of particles in a Debye square (or cube). For a specified input of N_{pc} particles per cell in a 2D simulation, this becomes

$$n_0 \lambda_D^2 = N_{pc} K \tag{3.36}$$

where n_0 is the density at the sheath entrance, and K is the number of particles in a superparticle.

One of the major benefits of using SPICE to simulate the MAST-U Langmuir probes in particular is the ability to implement arbitrary shapes in the simulation window. SPICE comes with the inherent functionality to draw arbitrary rectangles, circles, and triangles in 2D, and cuboids, cones and triangular prisms in 3D. Given the MAST-U probe tip's unconventional shape, as described in chapter 4, the ability to recreate this within the

simulation window is crucial. The inability to do this was a particular problem in previous simulation work done on MAST probes[73].

SPICE therefore represents a very good option among PIC codes for simulating the MAST-U Langmuir probe tips, both due to its particular attention to simulating the sheath through the pre-sheath particle distribution functions, and because of this arbitrary simulation object-shape feature.

3.4 Summary

This chapter has detailed the fundamentals of Particle-in-cell simulation. The positives and negatives of various approaches to simulating plasmas have been outlined while making it clear that particle simulation is the most promising route for simulating the plasma around Langmuir probes. The basic algorithmic flow of a PIC code has been described and some of the numerical methods illustrated using 1D examples. The specifics of the PIC code SPICE have also been presented and the features of that code which make it particularly well suited to simulating Langmuir probes have been highlighted. The SPICE simulation scenario designed for examining sheaths in the divertor has been introduced, which will be used to simulate flush-mounted probes and angled-tip probes in MAST-U-like conditions in chapter 5.

Chapter 4

Experimental Methods

4.1 MAST-U Langmuir probes

4.1.1 Introduction

As part of this body of work, an experiment was carried out on the linear device Magnum-PSI at the Dutch Institute for Fundamental Energy Research (DIFFER). This experiment aimed to verify the design of the MAST-U Langmuir probe tip through a series of measurements with well defined magnetic field incidence angles. The physical setup and plasma conditions are also considerably simpler than in a tokamak, aiding analysis. The design of the MAST-U probe tip, the experimental setup, and the analysis techniques used in this experiment are presented in the remainder of this chapter, with the results and discussion on the consequences for the interpretation of Langmuir probes in MAST-U discussed in chapter 6.

4.1.2 Angled tip design

As part of the diagnostic suite on MAST-U, there are Langmuir probes installed throughout the plasma facing components (PFCs). A total of 850 are arrayed in the divertors (top and bottom), gas baffle, central column and the nose (see figs. 4.1 and 4.3). These probes have

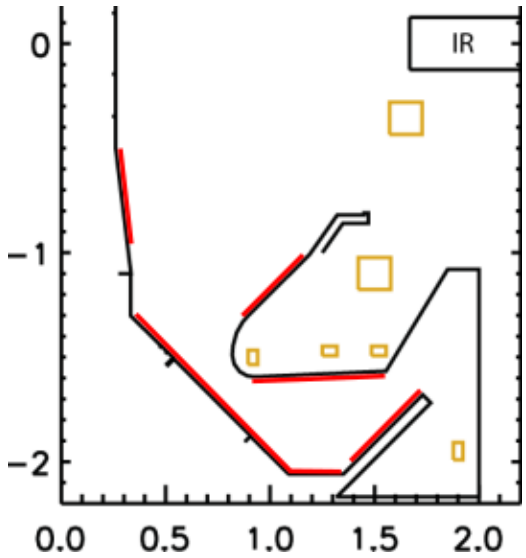

Figure 4.1: Schematic cross-sectional diagram of MAST-U showing location of the Langmuir probe arrays in the lower divertor. Identical arrays are also present in the upper divertor. The scale is in m.

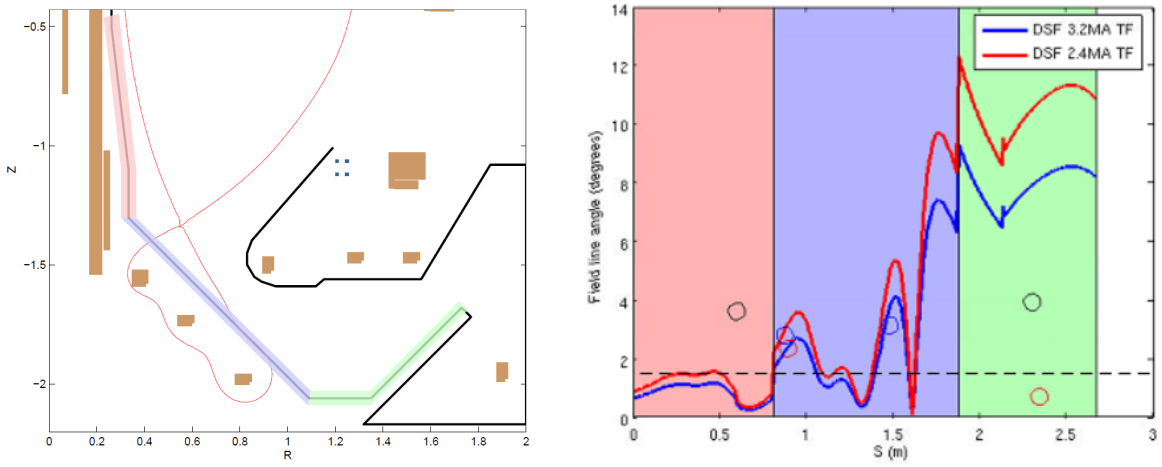

(a) (b)

Figure 4.2: (a) A schematic view of the MAST-U divertor with a *conventional* scenario plasma equilibrium overlaid. (b) The variation of the field line incidence angle to divertor surfaces as a function of distance along the divertor. In this particular case plasma is controlled so the strike point is on the divertor science facility and the maximum incidence angle to the divertor surfaces can be seen for two different plasma currents. The range of angles is therefore from 0-12°. The background colours correspond to the different surfaces coloured in (a). Adapted from [74].

a novel design intended to maximise the area presented to the plasma for measurements by angling the probe tip 10° towards the expected inclination of field lines. Such an approach was pioneered on the Joint European Torus (JET)[31] and DIII-D[75, 76] tokamaks, wherein similarly angled-tip designs were used successfully. There are a range of expected field line angles in MAST-U (see fig. 4.2), which vary depending on the plasma scenario used, but typically fall in the range of 0-12°. The value of probe tip inclination was chosen to maximise the effective collection area for the smallest incidence angles and therefore reduce or prevent non-saturation of the ion current. However, this approach also exposes more of the probe tip to the plasma and so must be balanced by improving the maximum tolerable heat flux of the probe. This was done in a twofold approach: each probe has a large bulk of material attached to the probe tip to act as a thermal reservoir and allow for higher operating temperatures; and the material chosen for the probes was pyrolitic graphite, oriented to allow maximum heat flow away from the probe tip to the accompanying thermal reservoir. This design therefore balances both the probe collection area and the

(a)

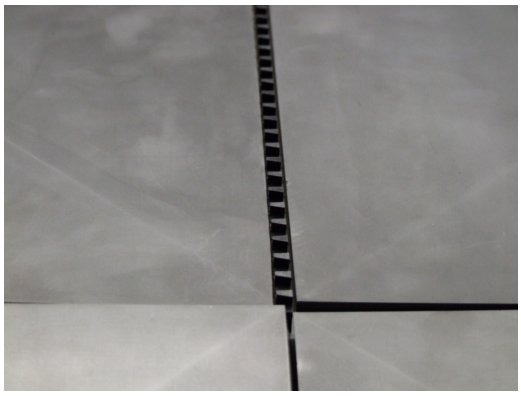

(b)

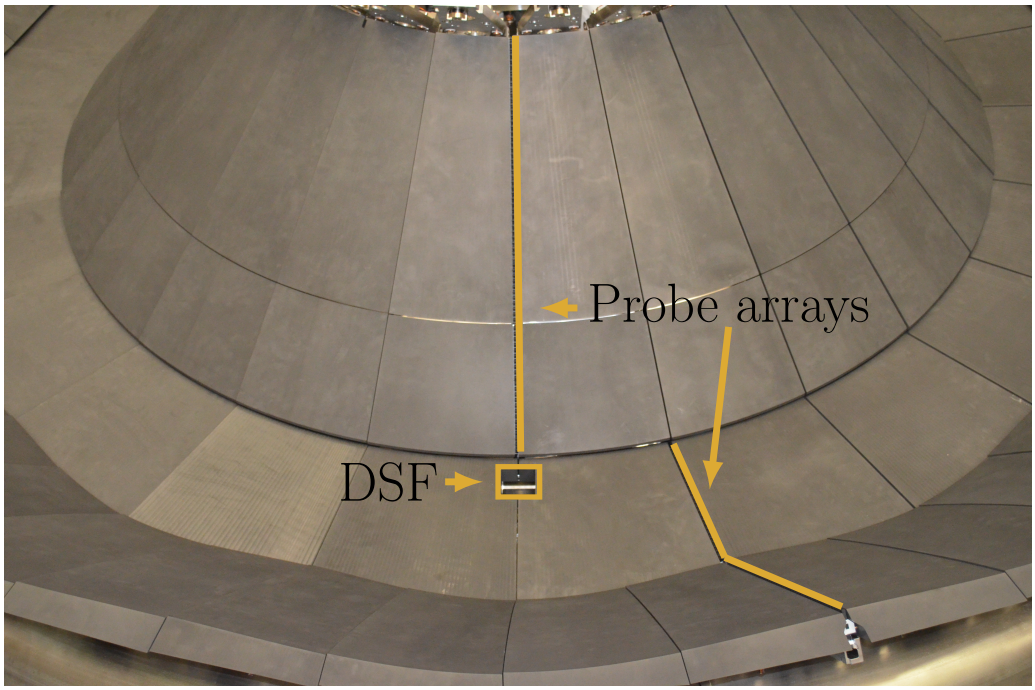

(c)

Figure 4.3: (a) Photograph of a MAST-U Langmuir probe, showing the right trapezoidal tip and thermal reservoir. (b) Photograph of one of the MAST-U Langmuir probe arrays (c) Photograph of the MAST-U lower divertor showing the *in situ* location of the probe arrays and the square hole of the divertor science facility (DSF), into which the DSF probe head will be inserted.

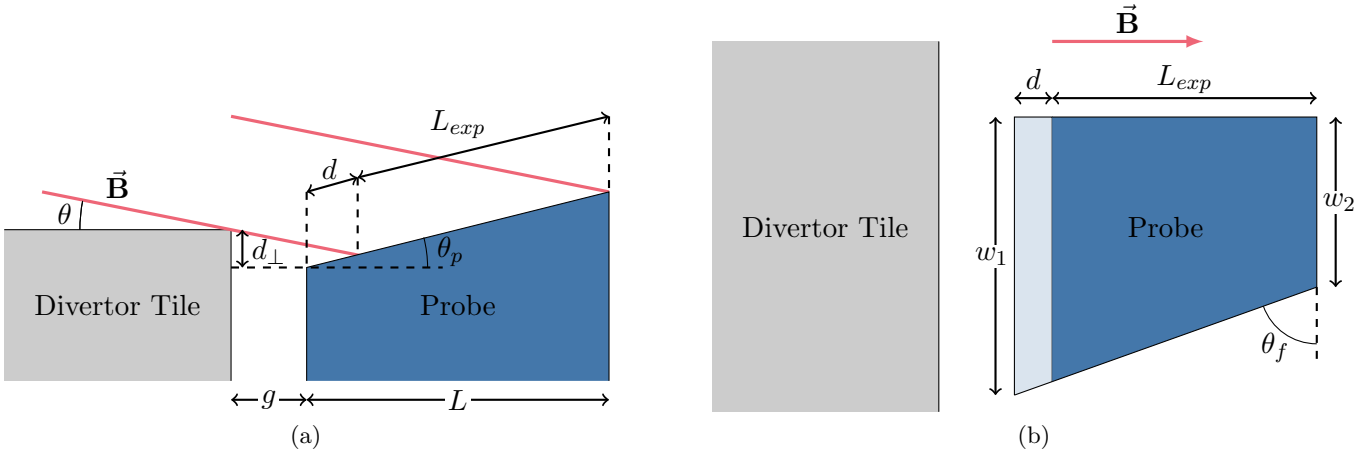

Figure 4.4: Schematic of MAST-U probe (a) cross section, and (b) plan view. The lighter blue section in (b) corresponds to the shadowed portion of the probe.

safe operating temperature, allowing for the best performance of the diagnostic within expected MAST-U conditions[74].

The probe is also recessed relative to the tile in front of it (toroidally) to allow the leading edge to be shadowed, i.e. protected from direct exposure to the plasma. Leading edge shadowing is standard practice in PFCs to prevent the exposed material from both sputtering into the plasma or from receiving too high a heat flux. The size of the recession (denoted $d_\perp$) in this case was chosen as 0.3mm, as this was the minimum value which both shadowed the leading edge (for expected operating conditions of $0.5 \geq \theta \geq 10.0$), and was able to be practically achieved given machining tolerances of $\pm$0.1mm. The probe is also right-trapezoidal in geometry to ensure that the RHS of the probe is not exposed to plasma at the expected values of the radial magnetic field component. The angle of the trapezoid, θ_f, is set to 75°.

The probe geometry is therefore a significant departure from the flush, square probe described by the sheath expansion parameter derived by Bergmann[24, 38] and Murphy-Sugrue[53]. Figure 4.4 shows the definitions of the various geometrical aspects of this probe design. Using these definitions, we can write down an estimate of the effective collection area of this probe as the unshadowed geometric area projected along the magnetic field

$$A_{eff} = \frac{1}{2}\left[w_1 + w_2 - \frac{d}{\tan\theta_f}\right] L_{exp} \sin\theta_{tot} \tag{4.1}$$

Probe	w_1 [mm]	w_2 [mm]	L [mm]	g [mm]	θ_f [°]	A_{geom} [mm^2]
L	3.34	2	5	1	75	13.3
S	3	2	3	2	72	7.5
B	6	4.5	5	1	73.3	26.25
R	N/A	N/A	4	1.5	N/A	12.6

Table 4.1: Principal dimensions and geometric areas of each of the probe tips on the divertor science facility probe head.

where $\theta_{tot} = |\theta| + |\theta_p|$ and d is the length of the shadowed probe extent, given by

$$d = \frac{d_\perp - g\tan\theta}{\sin\theta_p + \tan\theta\cos\theta_p} \tag{4.2}$$

and L_{exp} is the exposed probe extent, given by

$$L_{exp} = \frac{L}{\cos\theta_p} - d. \tag{4.3}$$

In the event that the equality $d_\perp > g\tan\theta$ is not satisfied, i.e. the leading edge is exposed due to unexpectedly large θ, an additional term must be added to eq. (4.1) to account for the additional collection area exposed on the front face of the probe. A_{eff} in this case becomes

$$A_{eff} = \frac{L[w_1 + w_2]}{2\cos\theta_p}\sin\theta_{tot} + w_1\cos\theta_p\big[g\tan\theta - d_\perp\big]. \tag{4.4}$$

4.1.3 Divertor Science Facility Probe Head

An additional part of the MAST-U probe suite is the divertor science facility (DSF) – a sample manipulator in the divertor which allows for the introduction of different electrical probe heads[77] and material samples without requiring a vessel vent. A probe array has been designed for use as a DSF head, to operate in tandem with the divertor Langmuir probe system. The probe array has four different Langmuir probe tips:

L – a standard MAST-U FMP, as described in section 4.1.2

S – a smaller probe with approximately half the geometric area of the L probe

B – a larger probe with approximately double the geometric area of the L probe

R – a flush, cylindrical probe with similar geometric area to the L probe

Table 4.1 describes the exact values of geometric parameters, including the geometric area of each probe variant.

The S and B probes are very similar to the standard MAST-U probe (L): right-trapezoidal in geometry with the surface of the trapezium angled 10° relative to the incident magnetic field. The angle of the trapezoid varies between probes. As such the calculation of the effective collection area similarly uses eq. (4.1) (and eq. (4.4)) with different values for L, g, w_1, w_2 and θ_f where necessary. The R probe is cylindrical in geometry and recessed to shadow the leading edge, but does not have an inclined surface. The shape, and thus geometric area, can therefore be described by principal variables r – the probe radius, and $d_\perp$ – the recession of the leading edge with respect to the shadowing tile. The effective collection area is therefore given by

$$A_{eff}^{R} = \left(\pi - \frac{\theta_c - \sin\theta_c}{2}\right) r^2 \sin\theta \tag{4.5}$$

where θ_c, the angle subtended by the chord delineating the shadowed region (see fig. 4.5),

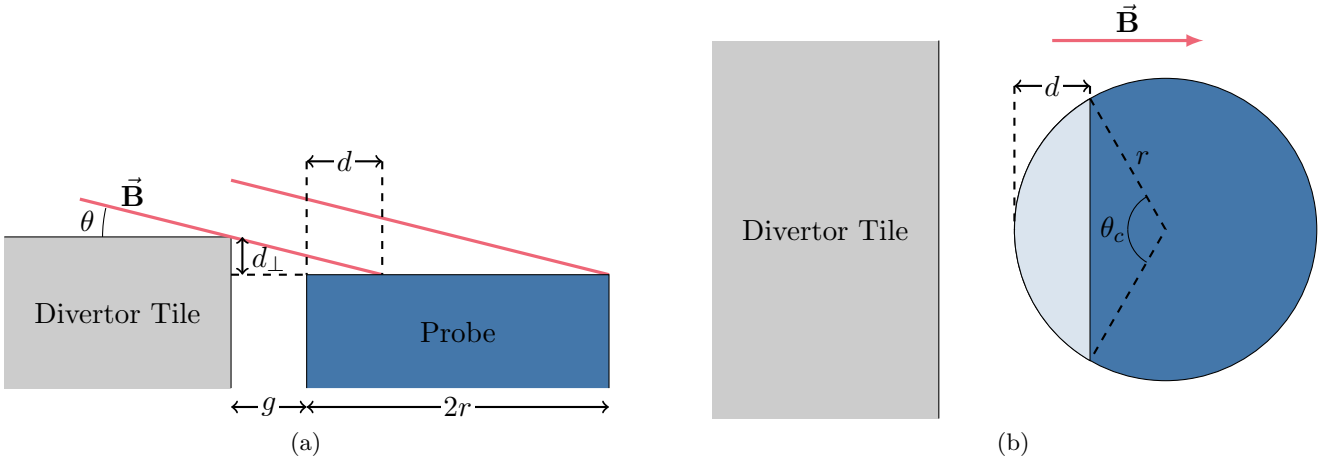

Figure 4.5: Schematic of cylindrical probe on the divertor science facility probe head, designated R, shown in (a) cross section, and (b) plan view. The lighter blue section in (b) corresponds to the shadowed portion of the probe.

is given by

$$\theta_c = 2 \arccos\left(\frac{r-d}{r}\right). \tag{4.6}$$

In all cases $d_\perp = 0.3$mm.

Materially the probes were designed within the same engineering constraints as the standard MAST-U Langmuir probe tip. All are made from pyrolitic graphite oriented down the long axis of the probe and all have a large thermal reservoir set back from the plasma facing tip to allow for higher operating heat fluxes. All probes are electrically isolated from each other by a ceramic pin holder, and shadowed from plasma exposure by a graphite shell around the whole assembly.

4.2 Experiment on Magnum-PSI

The MAST-U probe tip is well designed to mitigate problems with interpretation, but has yet to be experimentally tested. An experiment has therefore been carried out with twofold objectives: (a) confirm that the angled-tip design of the MAST-U Langmuir probe mitigates the issues caused by grazing angles of incidence, and (b) assess their performance in different regions of plasma parameter space before the upcoming MAST-U experimental campaign. Measurements were taken on the linear device Magnum-PSI at DIFFER, using the DSF probe head, at a range of plasma parameters and magnetic field configurations.

Magnum-PSI is a linear plasma device utilising a cascaded arc plasma source to generate stable plasmas [78] which emulate the high heat and particle fluxes expected in the ITER divertor. The source can produce low temperature (1-10 eV), high density plasmas ($> 10^{21}$ m^{-3}) confined with superconducting magnets to a beam with a full width at half maximum (FWHM) of $\sim 20mm$. The position of the target can be adjusted along the central axis of the beam (z), and rotated at angles to this axis (fig. 4.6). Density and temperature are not control variables; the input parameters to the source (gas flow and current) and the magnetic field are used in combination to produce different plasmas which are characterised with a well established Thomson scattering (TS) system [79]. Peak densities were achieved from 5 $\times 10^{18}$ m^{-3} up to $\sim$1 $\times 10^{21}$ m^{-3}.

This experiment used the 4-probe array designed for use in the DSF, as described in section 4.1.3. A specialised mounting assembly was designed and manufactured to hold the DSF probe head in place against the Magnum 'flat' target holder. This target holder is water cooled and could tilt the probes to a range of magnetic field incidence angles (θ).

A piece of graphite foil (a thin, flexible graphite material) was inserted into the interface between the graphite shell and the cooled target holder to improve the thermal conductivity between the two surfaces.

The voltage sweep on the probes was a 100Hz triangle wave (see fig. 4.7) created by an arbitrary function generator and amplified by a KEPCO 100-4M 100V bipolar operational power supply. The current from the probes was measured using a dual-channel isolational amplifier to observe the voltage drop across two separate shunt resistors. As such two shots were required to get a full set of probe measurements for a given plasma. All of these signals were then digitised by a National Instruments NI PXI-5105 digitiser, with the voltage signal attenuated by a factor of 10 to be sampled by the digitiser's 10V range. The digitiser samples at different, configurable rates, but the sample rate used was generally a minimum of 100kHz. The amplitude of the voltage sweep was configurable and therefore varied depending on the plasma parameters being observed. Typically the voltage sweep

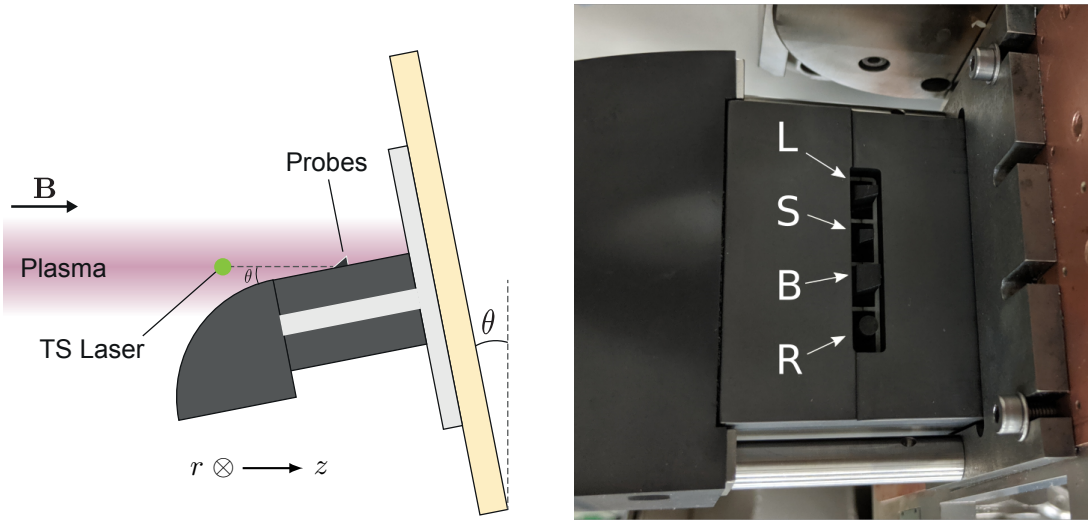

(a) (b)

Figure 4.6: (a) Experimental setup diagram showing relative location of probes and Thomson scattering (TS) laser, and θ as the magnetic field incidence angle. r and z correspond to the radial and axial coordinates used throughout. r follows Magnum-PSI convention and is positive toward the bottom of the machine, with $r = 0$ being at the approximate TS laser position. $z = 0$ at the TS laser position and is positive toward the probes. (b) Photograph showing the divertor science facility probe array installed in Magnum-PSI with all probes labelled.

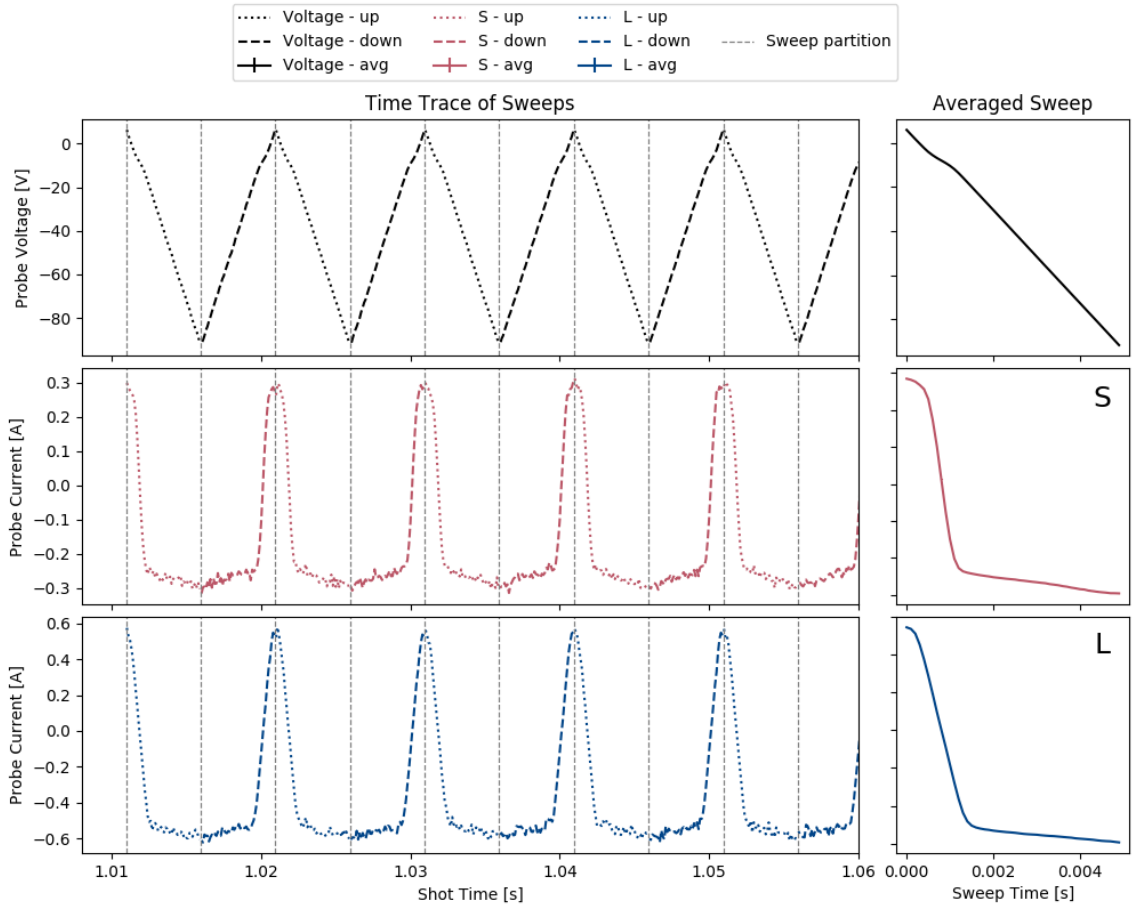

Figure 4.7: An example of the processed time-trace of the voltage *(top)* and current readouts for the S *(middle)* and L *(bottom)* probes on a 0.8T hydrogen shot. The shots have been divided into sweeps (shown as vertical dashed grey lines) and the up and down sweeps demarcated by dotted and dashed line styles respectively. Individual IV characteristics were later attained by averaging over both sweep-number and sweep-direction – see section 4.2.1.

ran from −100V to +10V, with the positive limit changed to capture more or less of the electron saturation region as appropriate to avoid drawing large currents ($> 1.5A$). The whole system was calibrated by scaling the voltage and current values outputted from the digitiser to match the IV characteristic of a 100Ω resistor. This calibration is accurate to $\sim 10^{-3}$A.

A diagram of the experimental setup – with the relative positions of the probe array, TS laser, and magnetic field – can be seen in fig. 4.6. The TS measurements are made at

$z = 0$, and were used as a comparison to the Langmuir probe measurements. The probe array was positioned perpendicular to the magnetic field and parallel to the radial profile measured by the TS system. The probes were moved as close to the TS laser as was possible without intercepting it. The probe holder was, as far as practically possible, aligned on the mounting arm such that the axis of rotation for θ lay inside all probes in the probe array, so as to minimise translation through the beam at different values of θ. Due to a tandem experiment being run by the MAST-U coherence imaging spectrometer, the distance to the TS laser was sometimes extended up to 200mm. Short exposures (5 seconds) were favoured to limit the surface temperature of the graphite components and thus prevent thermionic emission and carbon blooming.

Magnetic field incidence angle (θ) scans were performed, whereby all plasma parameters were held fixed while the probes were tilted with respect to the magnetic field using Magnum's rotating target arm, thus altering only the magnetic field incidence angle to the probe tip. This was conducted in the vein of Matthews et al.'s seminal work [47], and done with the aim of investigating how the angled-tip design functioned with changing θ. θ is defined as the angle between the magnetic field and the surrounding tile surface.

4.2.1 IV Characteristic Interpretation

Two shots were performed in J_{sat} mode (i.e. at a fixed voltage of -100V) to get a current time series for Fourier analysis. High frequency harmonics were found at ∼52kHz (fig. 4.8), so a low-pass Butterworth filter with a critical frequency of 45kHz was applied to all signals.

For all further shots the time trace was partitioned into individual voltage sweeps. Sweeps not performed during steady-state plasma operation in the shot (i.e. when the beam dump was fully out of the plasma and the source control parameters were constant, see fig. 4.9) were then discarded. The remaining sweeps were used to give IV characteristics. These were then sweep averaged – under the assumption that the plasma was steady state throughout probe exposure – and sweep-direction averaged – to cancel capacitance effects. The uncertainty on each current value was taken as the standard error ($\sigma_{\bar{x}} = \frac{\sigma}{\sqrt{n}}$) of the values being averaged (fig. 4.10).

A novel combination of probe analysis techniques was employed to minimise temperature overestimation when fitting the measured IV characteristics. The 3-stage fitting method, developed on the MAST probe system[80], was used with the final step being replaced by a goodness-of-fit minimisation algorithm. The 3-stage method involves first fitting a

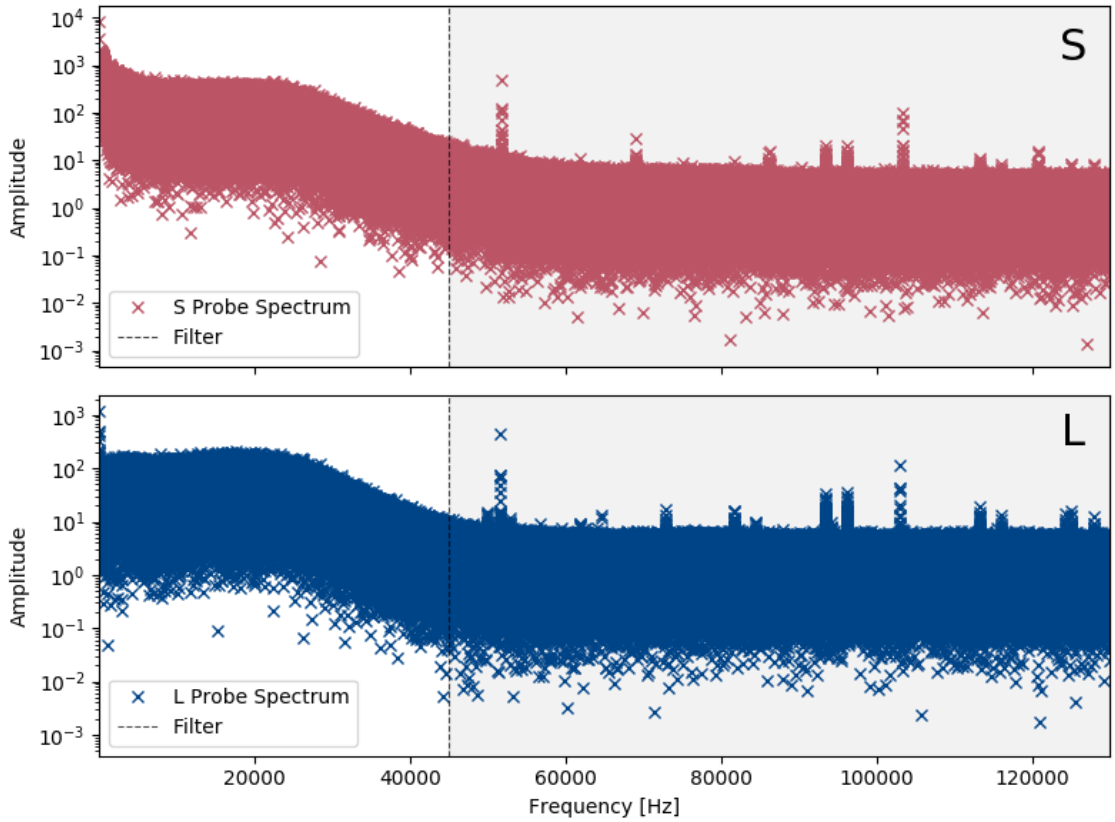

Figure 4.8: A frequency decomposition of a single bias (J_{sat}) shot for the S and L probe. Harmonics can be seen at ~52 kHz, with a low-pass filter applied with a critical frequency at the position delineated by the black line.

straight line to the saturation region of the IV curve. The definition of the start of the ion saturation region was decided by eye for each set of shots, but the final fit parameters were not particularly sensitive to this value. The straight line is then interpolated to generate a starting value for I_{sat}. A second fit is then performed to the whole IV (below V_f) but with I_{sat} held fixed to the value obtained from the first fit, in order to get initial values for the other three parameters. Finally a full, freely varying 4-parameter fit is carried out to get final fitting values and uncertainties, with the parameters from the second fit used as starting parameters.

In this analysis the final fit was replaced by a series of fits extending beyond the floating potential by varied amounts, and returning the minimum from these fits according to a

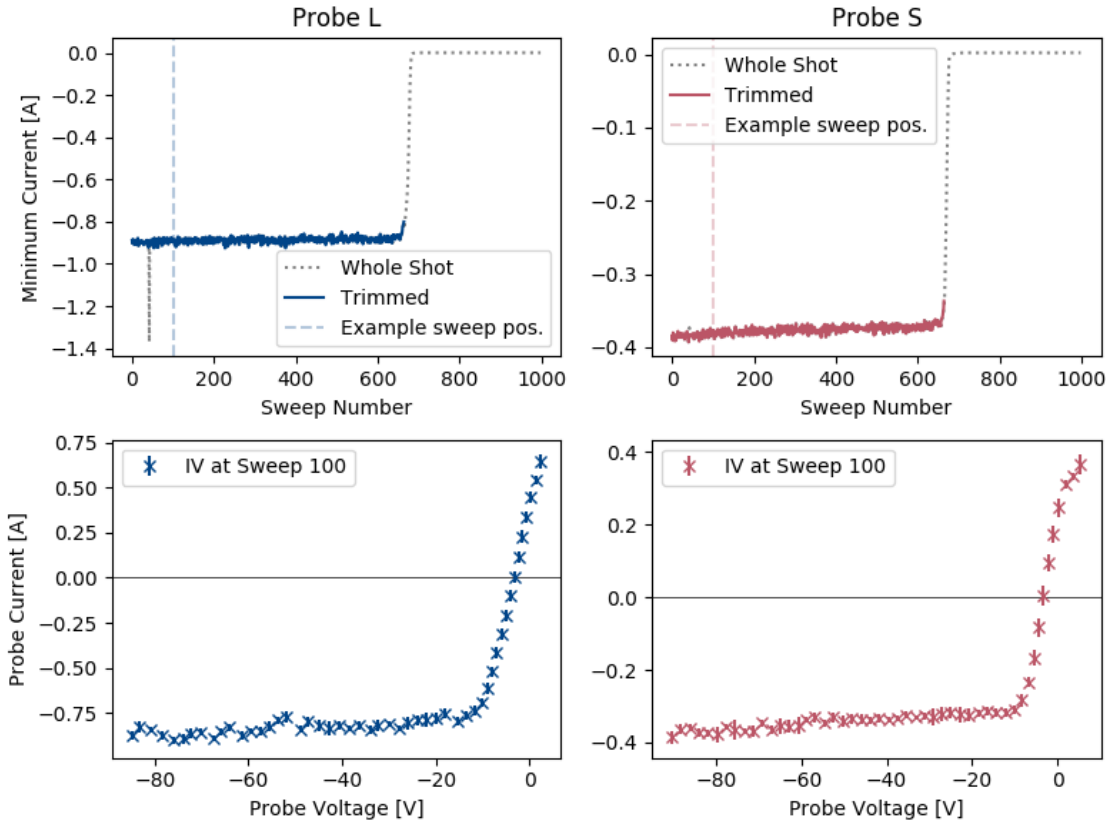

Figure 4.9: (Top) Examples of the trimming used to determine whether a particular sweep was performed during the steady-state section of the shot, or when the beam-dump was up or moving back into the plasma beam. The grey shows the minimum current value for each sweep – analogous to the ion saturation current and therefore proportional to density. The coloured segment denotes the sweeps performed during the steady-state part of the shot, determined by being 2 standard deviations from the median value of minimum current. A spike can be seen in the L probe around sweep 50, which is an arcing event. The sweep in this case was discarded. (Bottom) An example IV characteristic from the steady-state section of the shot, taken using the L probe (left) and the R probe (right).

goodness-of-fit parameter. This goodness-of-fit parameter was set to one of two options: (a) the product of T_e and δT_e (uncertainty on T_e), or (b) the product of T_e, δT_e and $|\chi^2_\nu - 1|$ where χ^2_ν is the reduced χ^2 statistic of the fit. Parameter (a) was used in the majority of cases, unless it was found that prioritising pure temperature minimisation was producing an unphysical fit. All fitting was performed using non-linear least squares using the python

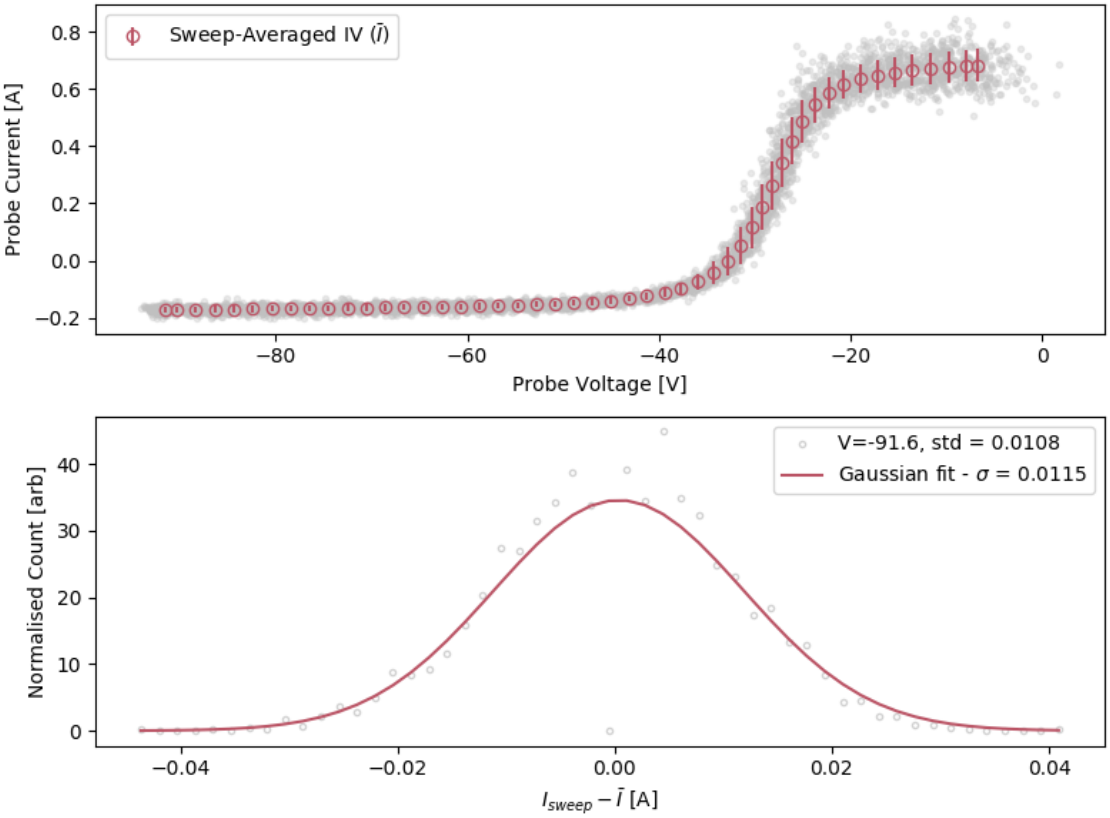

Figure 4.10: (above) An example of a sweep-averaged IV characteristic (red) on the S probe overlaid atop the individual current/voltage measurements for all sweeps during the steady-state section of a particular shot. (below) The distribution of current values about the mean for a particular value of voltage (in this case $V = 95$V). The distribution is roughly Gaussian (overlaid in red), justifying the use of the standard error to denote the uncertainty on a given current value.

package flopter[81].

Bergmann's 4-parameter model with Child-Langmuir scaling [24] was selected as the IV characteristic model of choice, as using a 4-parameter fit is well-established in reducing the overestimation of extracted temperatures[69], and Bergmann's model is the most physically justified.

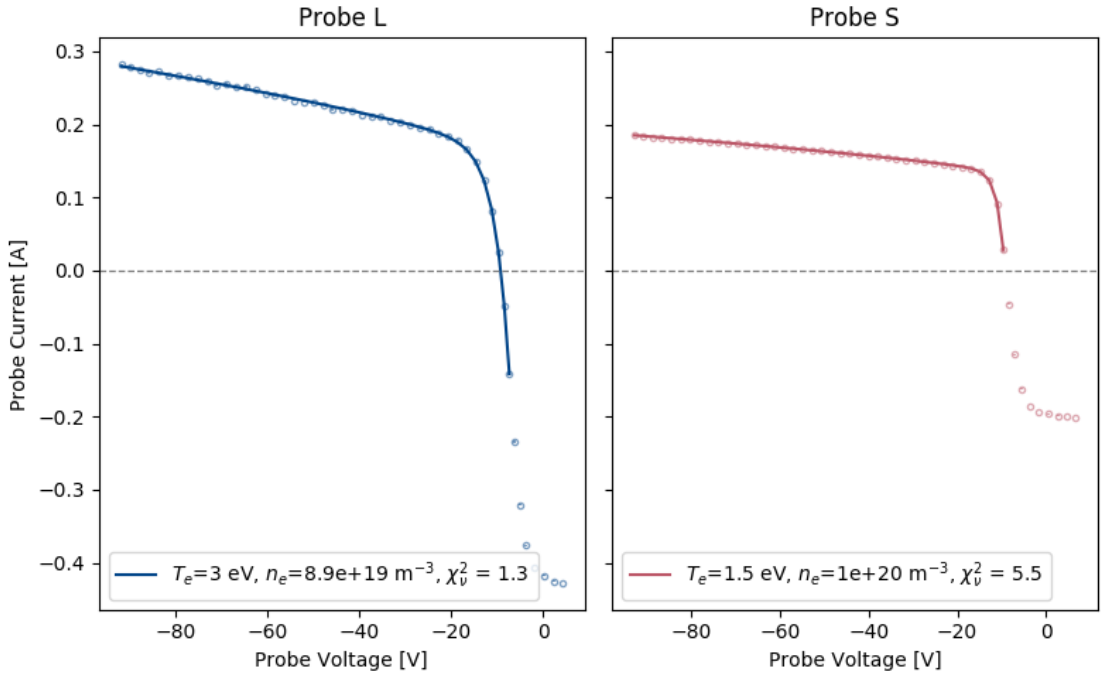

Figure 4.11: Example IV characteristics ($\theta = 2°$) with a fit using Bergmann's 4-parameter IV overlaid for the L (left) and S (right) probes. The fit was achieved using a modified version of the 3-stage method developed on MAST[80].

The model is given by

$$\frac{I}{I_{i,sat}} = 1 + a|V|^{\frac{3}{4}} - \exp(-V) \quad \text{with} \quad V = \frac{e(V_p - V_{fl})}{k_B T_e} \tag{4.7}$$

where I is the measured current, $I_{i,sat}$ is the ion saturation current, V_p and V_{fl} are the probe and floating potentials respectively. The sheath expansion parameter, with inclusion of gaps [53], was utilised when calculating a value of a for both initial fitting parameters and later comparison (eq. (2.62)). The values for frontal and lateral sheath expansion on the probes, c_1 and c_2, were set to 0.9 and 0.6 respectively, as per Murphy-Sugrue's findings for flush-mounted probes with gaps[53].

Densities were calculated from the fitted parameters using the definition of ion saturation

current (eq. (2.50)) but generalised to ions of any charge

$$I_{sat} = n_{se} Z e c_s A_{eff} \tag{4.8}$$

where c_s is the ion sound speed (as described in section 2.2.2, eq. (2.25)), and A_{eff} is the effective collection area of the probe. n_{se} in this case is the sheath edge density and thus must by multiplied be a factor of 0.5 to compare to the bulk n_e as measured by the TS. The collection area for each of the DSF probe tips were outlined earlier in this chapter in section 4.1.2. An example of an IV characteristic with an overlaid 4-parameter fit can be seen in fig. 4.11.

For density calculations, it was assumed that $T_e = T_i$, as suggested by recent collective TS results on Magnum-PSI [82]. This was previously found to be the case in the MAST divertor[39], providing justification for the comparison to expected MAST-U divertor conditions. Although Magnum-PSI plasmas would be expected to be more quiescent than fluctuation-prone tokamak plasmas, fluctuations within the MAST-U divertor are expected to be detectable (and therefore removable) by the probe system when operating in swept mode.

In certain shots, generally with lower temperatures, the knee of the IV characteristic was visible, allowing a measurement of Φ to be taken. This was performed by calculating the gradient of the IV characteristic, using the python package numpy[83], and returning the voltage at the maximum value. This value of Φ can then be combined with the measured V_{fl} value and used, with eq. (2.39), to calculate an estimate for T_e.

4.3 Summary

This chapter has presented the new, angled-tip design, in use on MAST-U Langmuir probes, intended to mitigate sheath expansion effects and make IV characteristics easier to interpret. 850 of these probes are arrayed throughout the PFCs in MAST-U. There is also a 4-probe array with a set of similarly shaped probe tips mounted on the DSF in the lower divertor, which allows the same local plasma to be interrogated by probes with varied collection areas. To verify whether this new angled-tip design works as expected, an experiment has been carried out on Magnum-PSI using the DSF probe head. The angle of magnetic field incidence was controlled using a target manipulator arm and probe measurements then compared to TS measurements made close to the probe surfaces. A novel IV-interpretation

technique has been developed, based upon the 3-stage method previously used on the MAST Langmuir probe system, utilising the Bergmann 4-parameter fit. Results from this experiment are presented in chapter 6.

Chapter 5

Sheath Expansion for a Recessed, Angled-Tip Probe

5.1 Introduction

Flush-mounted probes, and the dynamics of the sheath around their tips, have been the subject of detailed computational study. As such, models have been produced to express how the sheath expands as a function of angle of magnetic field incidence. As the MAST-U angled-tip design departs from these models in two significant ways – surface angling and recession – it would therefore be prudent to investigate how these departures affect the expansion of the sheath.

5.2 Updating for the MAST-U Probe Design

Bergmann's simulations in [24] and [38], as well as Murphy-Sugrue's subsequent extension [53], model the sheath as a rectangular box. The box expands with increasingly negative voltage in both the frontal and lateral directions, i.e. both parallel and perpendicular to the probe surface normal. The way this box expands with voltage is therefore described by the form of the sheath thickness voltage-scaling, and the geometry of the sheath in an expanded and unexpanded form.

Assuming that the sheath scaling has the same functional relationship on V and θ as found by Bergmann, the same logic can be employed to build a similar model of the sheath around a recessed, angled-tip probe. The best choice of sheath shape is not immediately clear, so two treatments are proposed with different approximations: a rotated rectangular sheath and a parallelogrammatic sheath.

5.2.1 Rotated Rectangular Sheath

The sheath in this case is treated as a rotated rectangle which expands, as before, normal to the probe surface (Δ – frontal expansion) and parallel to the surface (δ – lateral expansion). A schematic drawing of the sheath, defining the parameters of interest, can be seen in fig. 5.1. This shape of the probe is characterised by four key parameters: the angle of the probe tip to the horizontal plane (θ_p), the depth of the recession of the leading edge ($d_\perp$), the probe length (L) and the size of the leading gap (g). The sheath shape is therefore similarly controlled by these parameters.

Following the derivation in [24] and [53], we first write down the ion current to a floating probe, assuming all ions that come into contact with the sheath perimeter are collected. We can arrive at this via eq. (2.50). This expression is not as straight forward as in the

case of a flush-mounted probe, in which the collection area was taken to be the probe area projected along the magnetic field. In the 2D case this is given by

$$I_0 = en_e c_s (L + g) \sin\theta \tag{5.1}$$

where the part of interest is $(L + g)\sin\theta$ – the collection length per unit width in this 2D case (the projected collection area in a 3D case). For the angled-tip, recessed probe with a rotated rectangular sheath, this collection length L_0 becomes

$$L_0 = L_{exp,0} \sin\theta_{tot} \tag{5.2}$$

where $\theta_{tot} = |\theta| + |\theta_p|$ and $L_{exp,0}$ is the exposed sheath extent – analogous to the exposed probe extent from eq. (4.3) in chapter 4 – and is given by

$$L_{exp,0} = \frac{L}{\cos\theta_p} - \frac{d_\perp - g\tan\theta}{\sin\theta_p + \tan\theta\cos\theta_p} - \frac{\Delta_0 \cos\theta}{\sin\theta_{tot}} + \frac{\Delta_0}{\tan\theta_{tot}}. \tag{5.3}$$

There is now therefore an introduced dependency on Δ_0, which comes about from the angling of sheath expansion relative to the floating walls either side, and therefore disappears as $\theta_p \to 0$. In truth this is a dependence on Δ_w, but this will be discussed later.

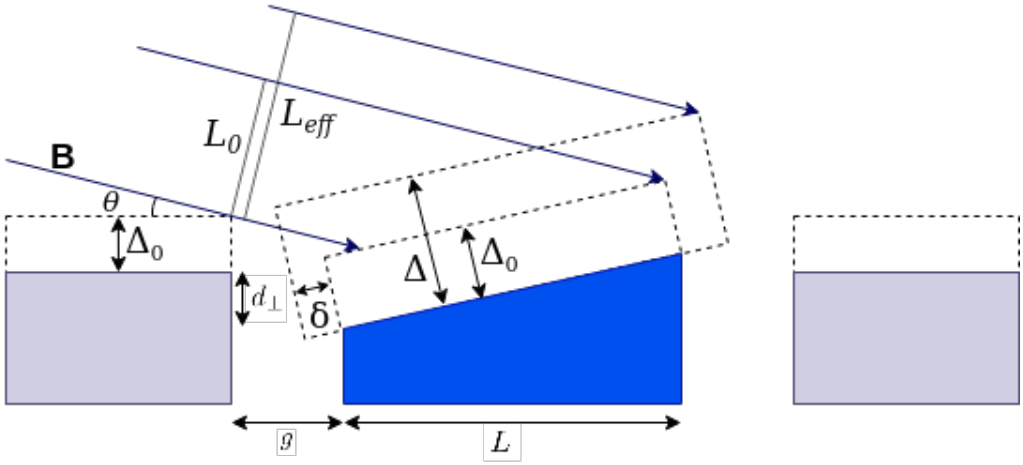

Figure 5.1: A schematic diagram of the setup for the rotated rectangular sheath. The collection length of the 2D probe at floating potential (L_0) and the effective collection length at some negative potential (L_{eff}) are also labelled.

We can also calculate the general form of ion current (I_i) to the probe, due to the expanded sheath at some voltage more negative than the floating potential ($|V| > 0$), as the current with the voltage-dependent effective collection length L_{eff} (see fig. 5.1). This is given by

$$L_{eff} = L_{exp,0} \sin\theta_{tot} + \delta \sin\theta_{tot} + (\Delta - \Delta_0)\cos\theta_{tot} \tag{5.4}$$

where δ is assumed to be equal on both sides of the probe.

Taking the ratio of these currents we get

$$\frac{I_i}{I_0} = \frac{L_{eff}}{L_0} = 1 + \frac{\delta \sin\theta_{tot} + (\Delta - \Delta_0)\cos\theta_{tot}}{L_{exp,0}\sin\theta_{tot}}. \tag{5.5}$$

Both δ and $\Delta - \Delta_0$ are proportional to $|V|^{\frac{3}{4}}$, so we can substitute in the expressions of proportionality from eqs. (2.57) and (2.58) and simplify to get

$$\frac{I_i}{I_0} = 1 + \left[\frac{c_1 + c_2\cot\theta_{tot}}{L_{exp,0}}\right]\frac{\lambda_D |V|^{\frac{3}{4}}}{\sin^{1/2}\theta_{tot}}. \tag{5.6}$$

Comparing this to the ion contribution in the assumed form of the IV characteristic equation eq. (2.59), we arrive at a new expression for the sheath expansion parameter

$$a_{RR} = \frac{c_1 + c_2\cot\theta_{tot}}{\sin^{1/2}\theta_{tot}}\frac{\lambda_D}{L_{exp,0}} \tag{5.7}$$

where the subscript $_{RR}$ denotes the rotated rectangular sheath.

This expression is equivalent to Bergmann's expression for a flush probe, but with $\theta \to \theta + \theta_p$ and $L \to L_{exp,0}$. The latter of these substitutions introduces Δ_0 as a dependency, so for this to have any kind of predictive power then an expression for Δ_0 must be obtained. This was not a problem in earlier derivations of sheath expansion parameters as the setup of the sheath shape allowed Δ_0 to be cancelled.

5.2.2 A Parallelogrammatic Sheath

An alternative formulation for the sheath shape is to assume that the frontal sheath still expands vertically into the plasma, as in the case of the fully flush probe. This is not necessarily the case for a real angled-tip probe but, as will be seen later, may yet provide a useful approximation to the more realistic behaviour outlined in section 5.2.1. The schematic for the parallelogrammatic sheath can be seen in fig. 5.2.

As before, we proceed by finding an expression for the ion current to the floating probe. Both the probe and wall sheath surfaces are simply shifted upwards by Δ_0 when compared to the calculation of the MAST-U probe projected area from eq. (4.1) in chapter 4, meaning that

$$\begin{aligned} L_0 &= L_{exp} \sin\theta_{tot} \\ &= L[\sin\theta + \cos\theta \tan\theta_p] + g\sin\theta - d_\perp \cos\theta \end{aligned} \tag{5.8}$$

where all values are the same as the previous derivation. Similarly, the effective collection area can be expressed as

$$\begin{aligned} L_{eff} &= (L + 2\delta)[\sin\theta + \cos\theta\tan\theta_p] + (g - \delta)\sin\theta + [(\Delta - \Delta_0) - \delta\tan\theta_p - d_\perp]\cos\theta \\ &= L_0 + \delta[\sin\theta + \cos\theta\tan\theta_p] + (\Delta - \Delta_0)\cos\theta. \end{aligned} \tag{5.9}$$

We therefore arrive at a sheath expansion parameter by comparing the ratio of these quantities, substituting in the proportionality relationships and comparing to the assumed form of the ion branch of the IV characteristic. The assumption that the proportionality relationships still hold for a sheath expanding in the manner we have set up may not hold

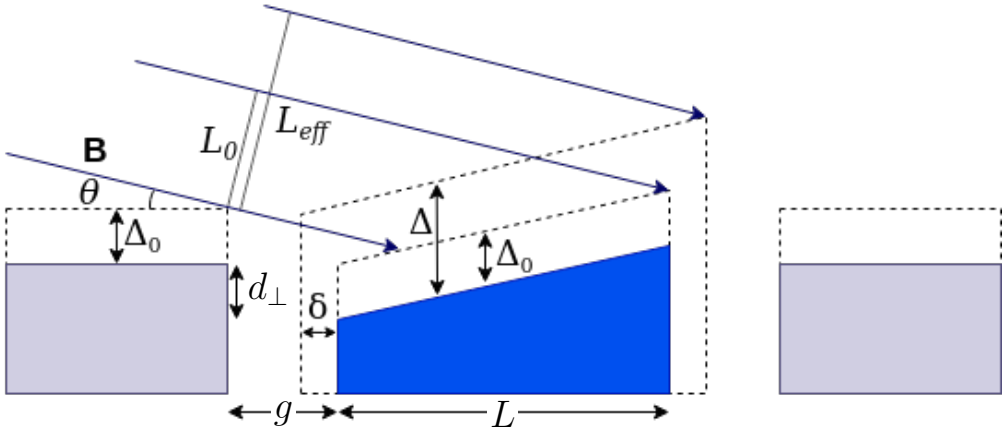

Figure 5.2: A schematic diagram of the setup for the parallelogrammatic sheath. In this case the sheath expands in the same direction as the sheath in front of the floating wall. The collection length of the 2D probe at floating potential (L_0) and the effective collection length at some negative potential (L_{eff}) are labelled.

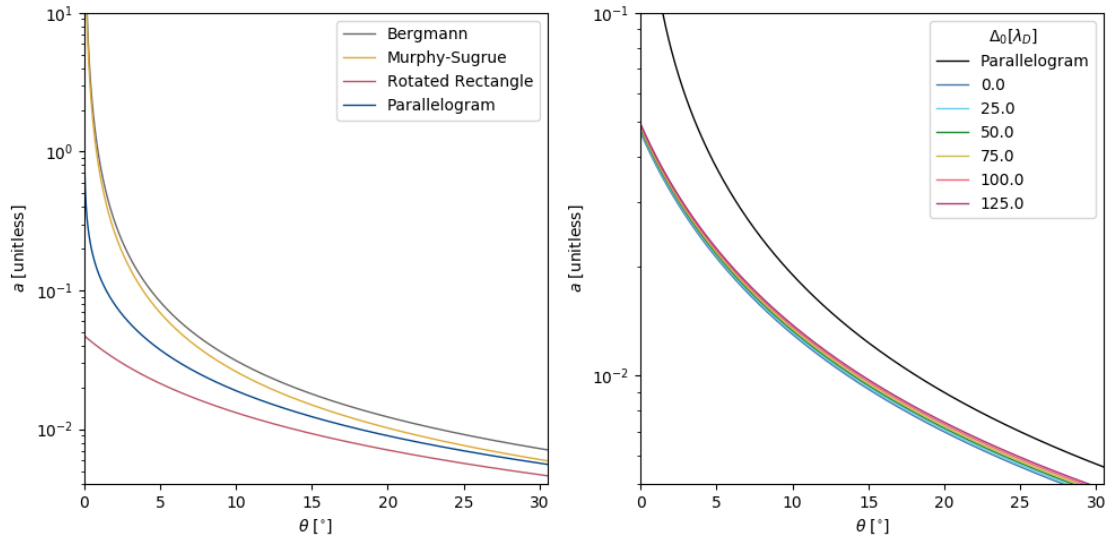

Figure 5.3: (left) Plot of predicted sheath expansion parameters from several different analytical forms. L and g were set to be $300\lambda_D$ and $60\lambda_D$ respectively with θ_p set to the MAST-U value of 10°. Bergmann's[38] values for $c_1 = 0.5$ and $c_2 = 0.6$ were used. Δ_0 in the case of the rotated rectangular sheath parameter was set to 0. (right) Shows the effect of different (constant) values Δ_0 on the profile of a_{RR}, with a_P drawn in black for comparison. Even for very large Δ_0 the change is essentially negligible when $\theta_p = 10.0°$.

well at large θ_p but will likely suffice for the MAST-U case. We therefore have

$$a_P = \frac{c_1[\sin\theta + \cos\theta\tan\theta_p] + c_2\cos\theta}{(L+g)\sin\theta + (L\tan\theta_p - d_\perp)\cos\theta}\frac{\lambda_D}{\sin^{1/2}\theta} \tag{5.10}$$

This expression has no dependence on Δ_0.

Both the new expressions for the sheath expansion parameter (eqs. (5.7) and (5.10)) reduce to Murphy-Sugrue's expression when θ_p and $d_\perp$ are set to 0, and therefore Bergmann's rectangular sheath when $g = 0$. It is not clear however what the coefficients c_1 and c_2 should be as the angling of the probe tip and the recession of the leading edge may change the scaling of the frontal and lateral expansion. The values of c_1 and c_2 can be approximated from a decomposition of 'measured' a values at different θ. These will be gained through simulations.

The different sheath expansion parameters are plotted in fig. 5.3 with MAST-U-like probe parameters and Bergmann's values for c_1 and c_2. a_{RR} has been plotted, with $\Delta_0 = 0$,

and predicts much less sheath expansion than the other parameters at small angles. a_{RR} has also been plotted with a range of Δ_0 and it is found that the change in profile is very small, even for the largest, and probably unrealistic, $\Delta_0 = 120\lambda_D$. It is arguable therefore that for the MAST-U probes with $\theta_p = 10°$, the contributions from the Δ_0 terms are negligible and can safely be ignored.

5.3 The Simulation Model

The particle-in-cell code SPICE, as described in chapter 3, was used to carry out simulations of Langmuir probes with MAST-U-like design parameters and in MAST-U-like conditions. SPICE was operated in scenario 1, wherein particles are injected from the top of the simulation window, the probe and walls are situated along the bottom of the domain, and both sides of the domain are periodic. Both a flush-mounted probe tip ($\theta_p = 0°$) and a recessed, angled probe tip ($\theta_p = 10°$) were simulated, with length, gap size and recession depth set to the MAST-U probe values. The probe and plasma parameters used as inputs to the simulations are listed in table 5.1. A schematic of the simulation domain for each probe can be seen in fig. 5.4.

The simulations ran for a total of 4 $t_{z,trav}$ (eq. (3.32)). The simulation was found to saturate at around 2 $t_{z,trav}$. The potential of the probe object was then swept from -15.0 $\hat{V}$ to +5 $\hat{V}$ over the remaining 2 $t_{z,trav}$. The current collected by the probe at each voltage step was stored and thus an IV characteristic could be extracted.

For simulations of both flush and angled-tip probes, the simulation window width was

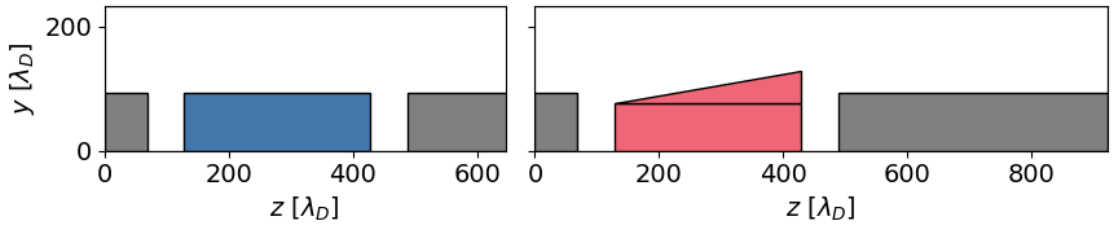

Figure 5.4: Schematic diagram showing simulation windows for the flush (left) and angled-tip probes (right) at $\theta = 10°$. The grey rectangles constitute the fore- and rear-walls, which were set to floating and fixed potentials in separate simulations. The length of the rear-wall is larger in the case of the angled-tip probe to account for self-shadowing.

Parameter	Value
T_e	5 eV
n_e	$1 \times 10^{18}\mathrm{m}^{-3}$
B	0.8T
ξ	17.18
μ	900
τ	1
θ	4-30°
N_{PC}	50
$\Delta_y\ (=\Delta_z)$	1.0 λ_D
L	300 λ_D
g	60 λ_D

(a) Plasma parameters

Parameter	Flush	Angled-tip
θ_p	0°	10°
$d_\perp$	0 λ_D	18 λ_D
L_z	232 λ_D	232 λ_D
L_y	570-1200 λ_D	570-1900 λ_D

(b) Probe parameters

Table 5.1: Input parameters for the 2D simulations of flush-mounted and angled-tip probes. Ranges of L_z and L_y denote the co-varying of the simulation window that took place to ensure the probes were not self-shadowing.

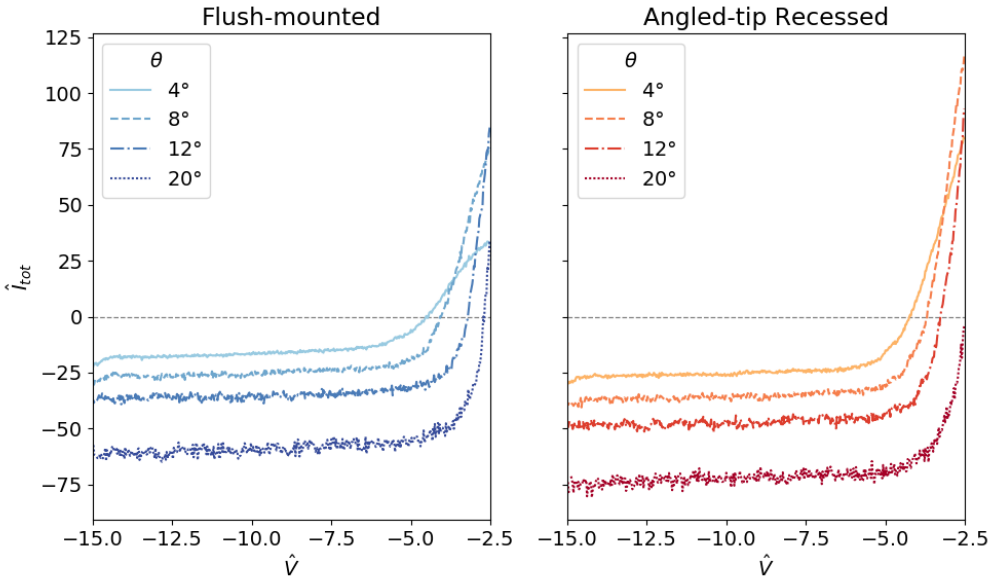

Figure 5.5: An example subset of simulated IV characteristics for the flush (left) and angled-tip (right) probes surrounded by a floating wall.

co-varied with angle so as to include the entirety of the shadow cast by the probe's sheath within the simulation domain and avoid probe self-shadowing. The greater vertical extent of the angled-tip probe required a concomitantly larger window width.

5.4 Results and Discussion

The IV characteristics extracted from the simulations of the flush and angled probes can be seen in fig. 5.5 for a subset of the range of simulated angles. The IV characteristics were fitted using two different fit functions (see fig. 5.6). The first fit function was the 4-parameter model devised by Bergmann (eq. (2.59)). Here the method of fitting was performed in two variations, a 'straight' fit to the IV characteristic below the floating potential, and a multi-fitting approach as employed on Magnum-PSI (see section 4.2.1). The second fit function was the ion contribution to this IV characteristic, i.e.

$$\frac{I_i}{I_0} = 1 + a|V|^{\frac{3}{4}}. \tag{5.11}$$

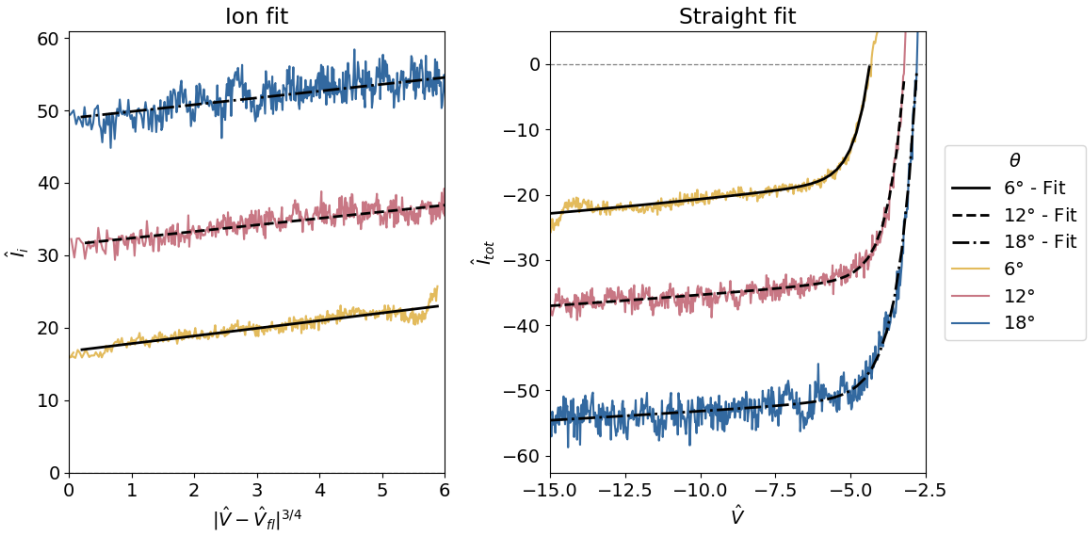

Figure 5.6: An example subset of fitted IV characteristics for the flush probe at a range of θ. Two fits are shown: a straight line fit to the ion current against $V^{3/4}$ (left), and a 'straight' 4-parameter fit (using eq. (2.59)) to the total current characteristic below the floating potential (right).

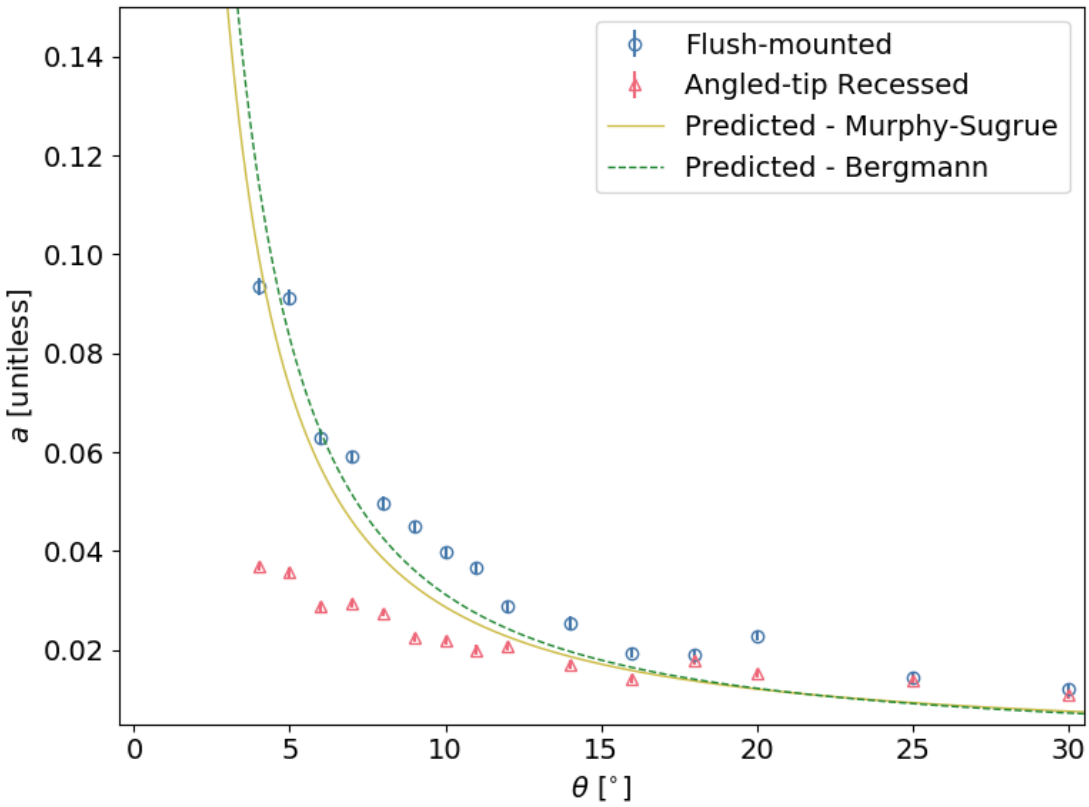

Figure 5.7: The sheath expansion parameters extracted from the ion current of simulated flush-mounted and angled-tip, recessed probes. The predicted curves, using Murphy-Sugrue's and Bergmann's expressions for a flush probe, are overlaid.

SPICE allows the separate collection of ion and electron currents to the probe, so the separated ion current can be fitted with eq. (5.11). In practice this is simpler to carry out by fitting a straight line to a plot of $|V|^{\frac{3}{4}}$ vs. I_i. This gives two separate methods of obtaining I_{sat} and a.

5.4.1 Sheath Expansion Parameter Coefficients

The extracted a values from the ion current fits can be seen in fig. 5.7. Both the flush-mounted probe and the angled-tip probe show the expected monotonically increasing behaviour. The flush probe shows inexact agreement with the predicted models of Murphy-

Sugrue and Bergmann, implying that the coefficients c_1 and c_2 require adjustment for these simulation parameters. The angled-tip probe sees consistently lower sheath expansion parameters, as predicted by both the parallelogrammatic and rotated rectangular sheaths.

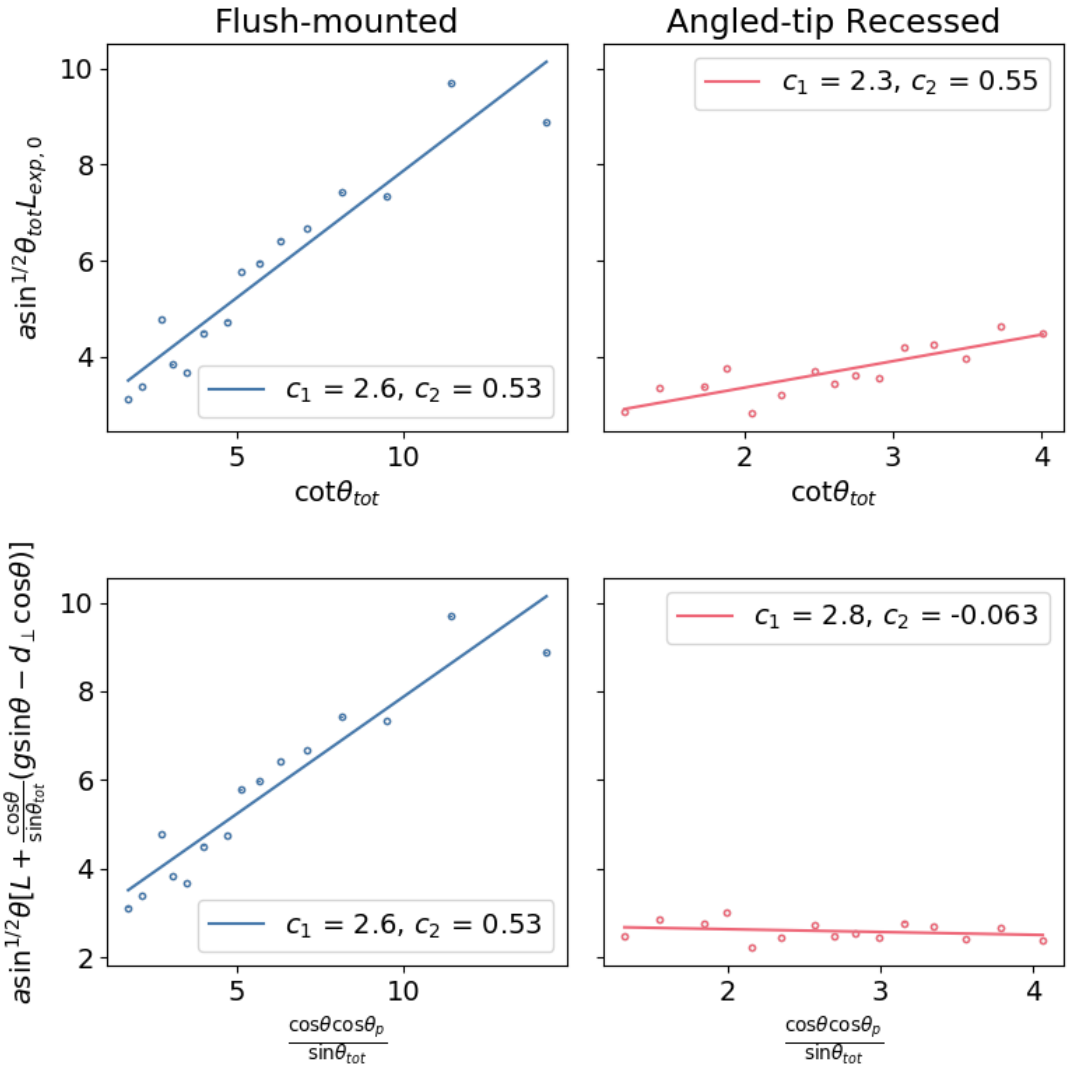

Figure 5.8: Decomposition plots of the sheath expansion parameters extracted from the lower resolution simulations. Decomposition for a_{RR} (bottom) and a_P (top) are shown, revealing similar values for c_1 and c_2 in the flush-mounted case, but differing values for the angled-tip case.

The coefficients c_1 and c_2 can now be extracted for these sheath expansion parameter profiles. This process, termed *decomposition*, involves plotting the numerator of the sheath expansion parameter against the denominator multiplied by the measured value of a. A linear fit to the resulting straight line can be used to determine c_1 and c_2. In the case of a_{RR}, Δ_0 was set to 0.

The decompositions for the lower resolution simulations can be seen in fig. 5.8. The decomposition of a_{RR} and a_P for a flush-mounted probe, i.e. with $d_\perp = \theta_p = 0$, reduces to the Murphy-Sugrue model. As such these decompositions found exactly the same values of $c_1 = 2.6$ and $c_2 = 0.53$ for the flush-mounted probe.

For the angled-tip probe, decomposition shows a fairly clear straight line indicating that the models are correctly predicting the measured sheath expansion. The obtained coefficients are different for each of the sheath models, with the rotated rectangular sheath model finding $c_1 = 2.3$ and $c_2 = 0.55$, and the parallelogrammatic model finding $c_1 = 2.8$ and $c_2 = -0.063$. A difference in these values is not unexpected given the differences in expansion direction of the sheath relative to the magnetic field in each model.

We can compare these coefficients to the values found by Bergmann and Murphy-Sugrue. For both models the flush-mounted probe frontal sheath expansion coefficient (c_2) was found to be ~ 0.5, which is in line with the three previous computational studies. The obtained c_1 values however, are much larger than the previous values found by Bergmann and Murphy-Sugrue, implying the contribution to the current collection from the lateral sheath expansion is much greater than previously thought, possibly due to the different plasma parameters. For the angled-tip probe, c_2 was found to stay at approximately 0.5 for the rotated rectangular sheath model, but reduced to -0.063 for the parallelogrammatic sheath model. This value being negative is surprising, as it implies that the sheath is contracting in the frontal direction as $\theta \to 0$. This is possibly a result of changing the direction of sheath expansion by assuming a parallelogrammatic sheath. In both cases c_1 stayed approximately the same and indeed still much larger than previously measured values.

5.4.2 The Effects of Wall Potential

As the walls of a tokamak are not always floating, and indeed in the case of MAST-U the walls are grounded, it would be informative to investigate the effect of changing the wall potential on probe measurements. Simulations were run with the wall set to an additional

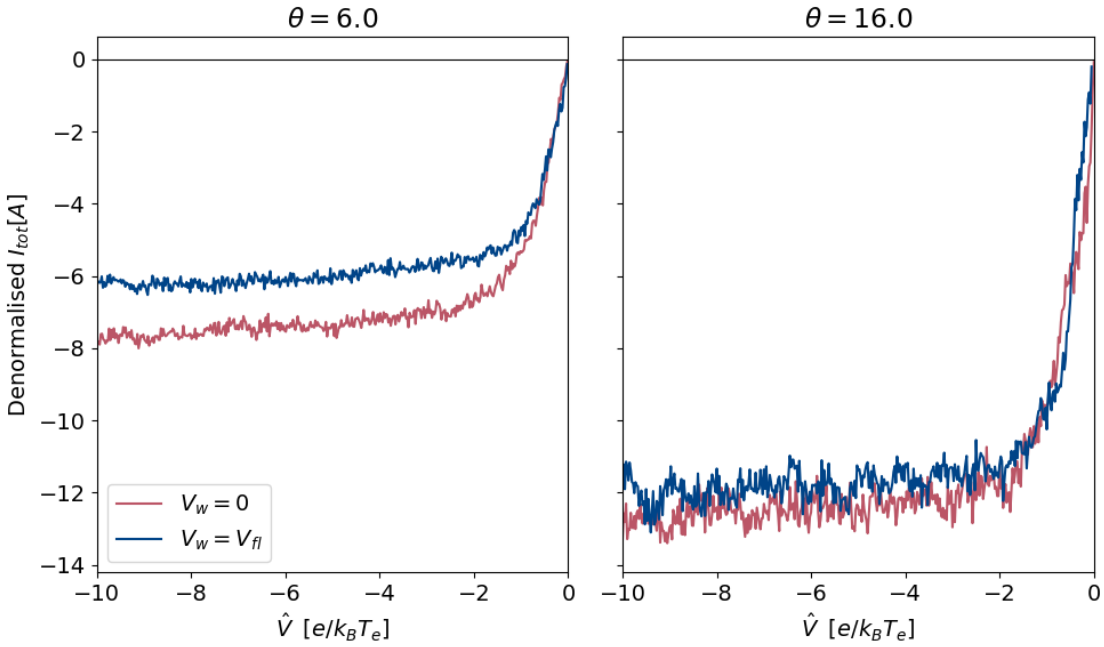

Figure 5.9: IV characteristics for the flush-mounted probe, with voltage corrected to the floating potential, for different wall potentials. Two different incidence angles – 6.0° (left) and 16.0° (right) – show increased saturation current at lower wall potential, indicating a larger probe collection area.

fixed potential ($V_w = 0\ e/k_BT_e$). With the addition of the previous set of simulations, in which the wall was floating, two wall potentials were simulated overall. Another angle scan was performed at this lower wall potential and for both sets of probe tips.

The ion branch of the IV characteristics for the two wall potentials, at two different angles, can be seen in fig. 5.9. There is a clear increase in current collected by both probes for the $V_w = 0$ case, which becomes more pronounced as $\theta \to 0$. This is most likely caused by an increase in effective collection area as the sheath shrinks due to lower potential, allowing portions of the probe previously shadowed by the sheath to be exposed to plasma. This can therefore be expressed as a correction to the effective collection length of the probe, in both the flush and angled-tip case, of the form

$$L_0^{'} = L_0 + (\Delta_0 - \Delta_w)\cos\theta \tag{5.12}$$

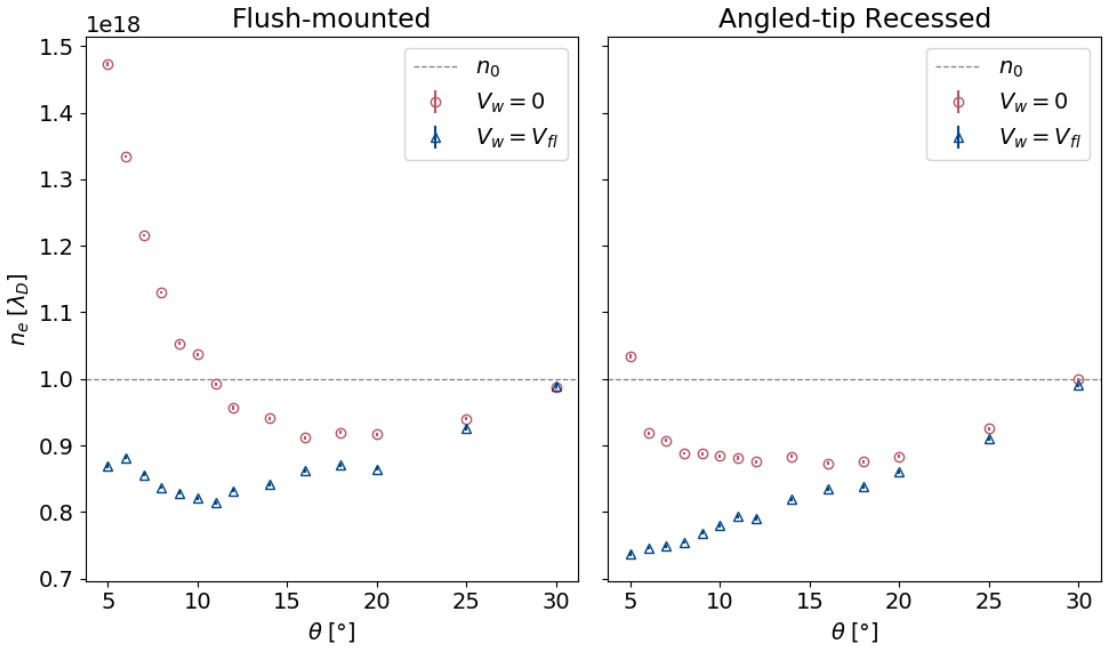

Figure 5.10: The synthetic density measurements, calculated from simulated ion current characteristics, are shown for both probe tips. The flush-mounted probe sees increased overestimation of the density at higher wall potential, especially pronounced at small θ, due to unaccounted-for probe collection area.

where $L_0^{'}$ is the corrected collection length and Δ_w is the sheath thickness in front of the wall at some wall potential V_w. $(\Delta_0 - \Delta_w)\cos\theta$ is the difference in sheath thickness from the floating case projected along the magnetic field. This effect therefore disappears when the wall is floating. To correct for this effect then, $\Delta_0 - \Delta_w$ must be known.

This increase in collection area, if not accounted for, could lead to an overestimation of density when analysing probe data for a probe in the presence of a floating wall. This overestimation will also become more pronounced as $\theta \to 0$ and the proportion of the collection area made up of the wall sheath contraction increases. This is illustrated in the densities synthetically measured by the simulated probes, whereby a large overestimation of density can be seen if evaluated without correcting the collection area with $\Delta_0 - \Delta_w$ (see fig. 5.10). Note that these densities were calculated with $\gamma_i = 2$ substituted into c_s. The probe simulations with the floating wall should be free of any overestimation due to this effect, and we see density values closer to n_0 in that case for both probes for $\theta > 5$. There

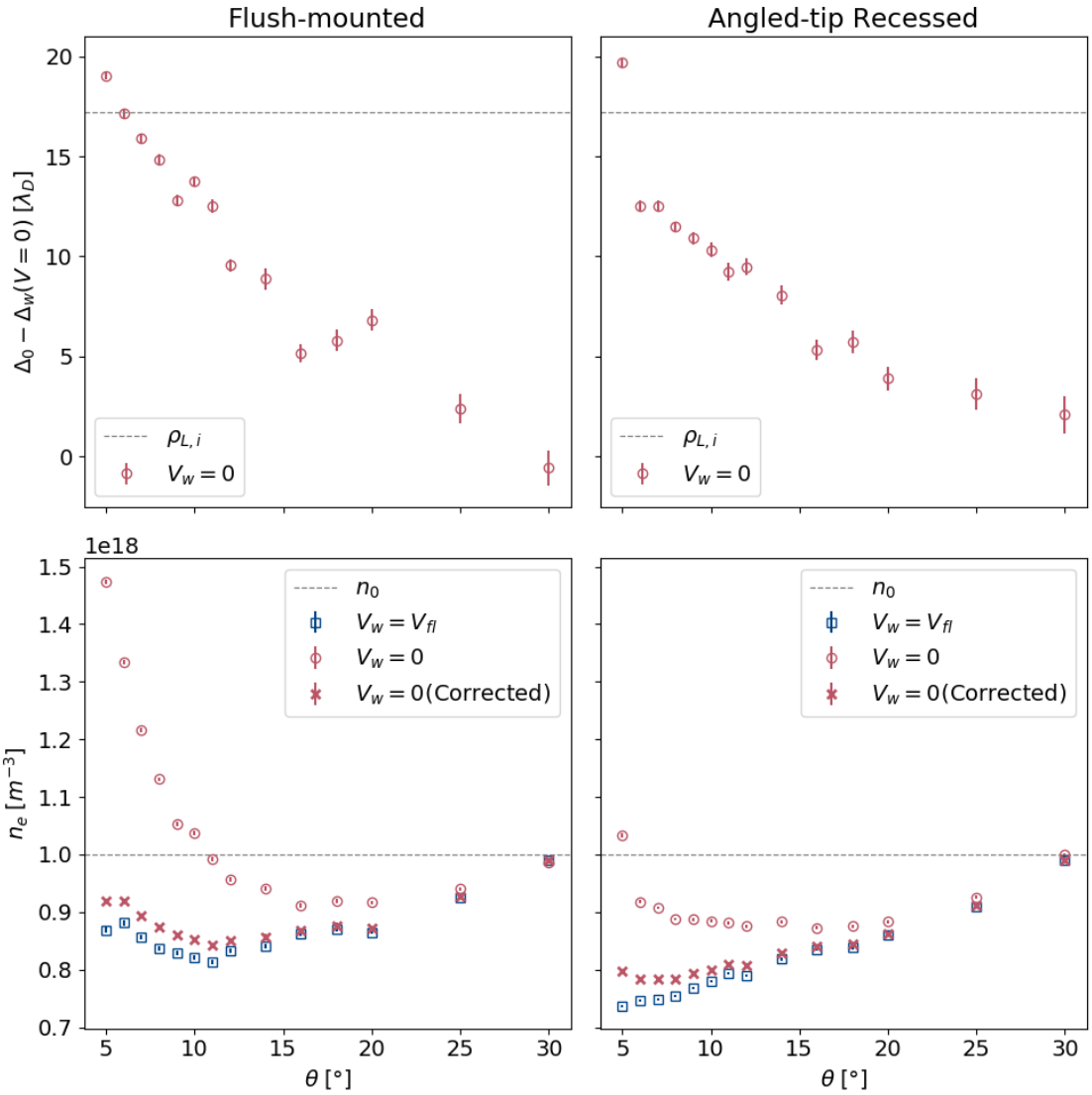

Figure 5.11: The reduction in sheath width from the floating case is plotted (above) as a function of θ. The sheath appears to increase in thickness down as $\theta \to 0$. The additional area from this sheath thickness is then used to correct the synthetic density measurements (below).

is however increasing overestimation as $\theta \to 0$ for the reduced wall potential simulations.

If we assume that the probes in the floating wall simulations are not receiving any

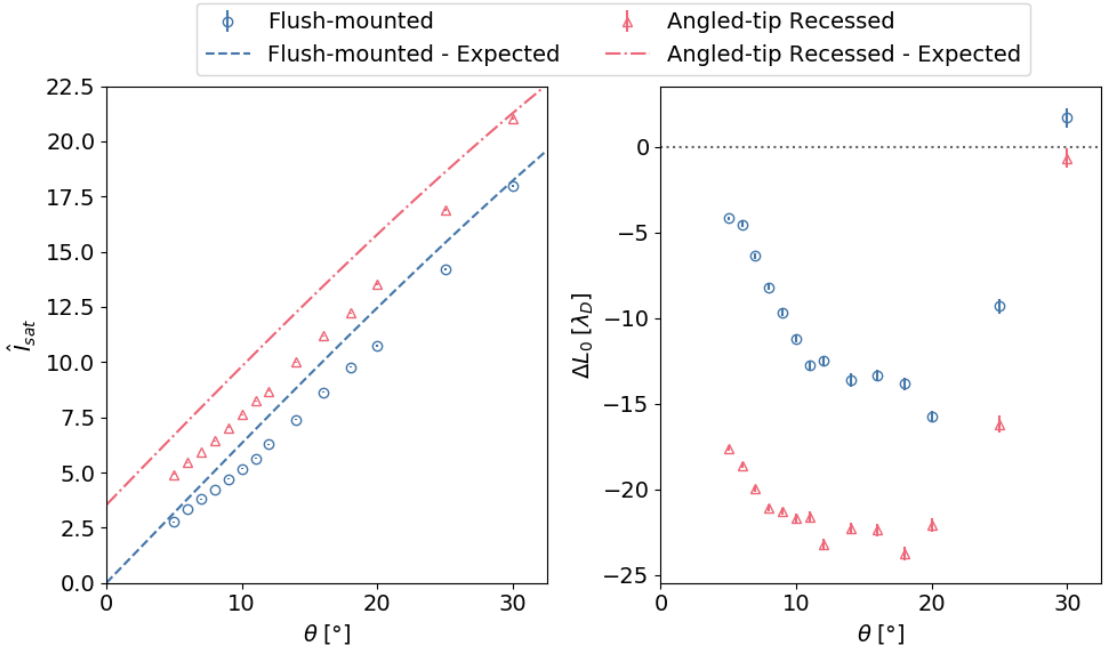

Figure 5.12: (left) Graph showing the comparison between expected and simulated $\hat{I}_{i,sat}$ for both probes. A clear reduction compared to the expected current, calculated from plasma input parameters, is seen. (right) Graph showing the difference between expected and simulated collection length (L_0) for both probes. The discrepancy in collection length appears to peak between $10 - 20°$ before inflecting.

additional current, they are therefore only comprised of current flowing to the probe through a collection length L_0. Thus, as per eq. (5.12), by subtracting this unmodified I_{sat} away from the I_{sat} of a probe with non-floating wall potential at the same θ, we can gain a measure of $\Delta_0 - \Delta_w$. In fig. 5.11 we can see this performed for both the flush and angled-tip probes. Both probes and wall potentials see increasing $\Delta_0 - \Delta_w$ up to $\theta = 8$, with both probes finding a maximum sheath thickness of just over $\sim 1\rho_L$.

This sheath thickness can therefore be used to correct for the additional collection area, thus removing the density overestimation due to this effect (see lower graphs in fig. 5.11).

For both probes, the floating wall case appears to increasingly underestimate density with decreasing θ. This implies that the expression for collection area (eq. (5.3)) is not fully capturing the collection area being simulated (see fig. 5.12). Both the simulated $I_{i,sat}$ and L_0 values show agreement with the expected values at $\theta = 30°$, but show a decreasing and

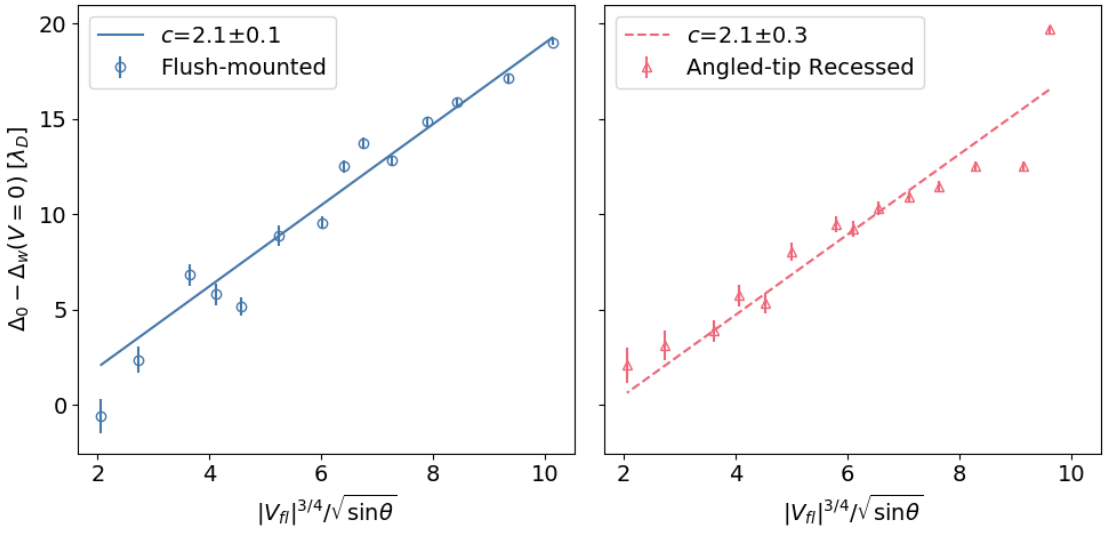

Figure 5.13: Graph showing the reduction in sheath width from the floating case, plotted as a function of $\frac{|V_{fl}|^{3/4}}{\sqrt{\sin\theta}}$. Assuming it follows the form Bergmann derived[38], a straight-line fit reveals the constant of proportionality for the sheath thickness scaling. A consistent value of $c = 2.1$ is found between the two probes, but the curve is offset and not clearly straight in the case of the angled-tip probe.

subsequently increasing profile down to $\theta = 5°$. There is an issue[84] with small θ SPICE simulations which is known to affect current which may be causing some discrepancy with the measured $I_{i,sat}$ values, but this would not be expected to have such a large effect. There is currently no other explanation for this phenomenon.

In this particular investigation $V_w = 0$ i.e. the same as the sheath edge potential. The wall sheath is therefore likely to be very small, reducing $\Delta_0 - \Delta_w$ to a measurement of the variation of Δ_0 with θ. This is, of course, under the assumption that all of the additional collection area is due to the sheath in front of the wall, i.e. that all other effects are encapsulated in our expression for L_0. We could assume that Δ_0 behaves similarly to Δ_1 (eq. (2.54)), and therefore has a similar constant of proportionality with $\frac{|V_{fl}|^{3/4}}{\sqrt{\sin\theta}}$. This has therefore been decomposed (see fig. 5.13) to obtain a value for this coefficient (termed c). The value of floating potential at each θ was taken as the mean wall potential from the floating wall simulations. Across both probes we see a consistent value of $c = 2.1$, however this may be dubious as the profile does not appear to be fully straight in the

case of the angled probe. Both decompositions also have a y-offset, which indicates that $\Delta_w(V = 0) \neq 0$. It would be future work to better characterise this sheath thickness by running more simulations for a greater range of plasma conditions and seeing how the measured $\Delta_0 - \Delta_w$ changes.

As this technique does not require the advantages of PIC simulation analysis to perform – it simply requires current measurements taken at the same density – it could therefore be used to measure the sheath contraction of a non-floating wall in front of any real Langmuir probe. A new type of probe could therefore be designed to take advantage of this effect and directly measure the sheath thickness. This could be implemented through having a separately biased front wall to adjust the size of the sheath shadowing in front of the probe. This may provide a method of experimentally verifying the sheath thickness scaling in eqs. (2.57) and (2.58).

5.5 Summary

This work was carried out with the aim of predicting the behaviour of MAST-U angled-tip Langmuir probes in order to assist in their analysis during operation.

By first building a simple geometrical model of the sheath, akin to those developed for purely flush probes, simulations were able to be used to create a predictive expression for the amount of current collected due to sheath expansion. Two models were presented with different approximations for the expansion of the sheath. The first is a rotated rectangular sheath which expands parallel and perpendicular to the probe surface normal, and as such has a dependency on Δ_0 due to the difference in sheath height between the wall and the probe. The second model was a parallelogrammatic sheath that avoids needing to know the exact height of the sheath at floating potential at the expense of exactness.

Simulations were run for a range of angles and the sheath expansion parameters analysed to obtain the coefficients of each of these sheath expansion models. Different values were found for the flush-mounted probe and the MAST-U-like angled-tip probe, with the latter being found at a value of $c_1 = 2.3$ and $c_2 = 0.55$ for the rotated rectangular sheath model. This can potentially now be used to predict a value of a for MAST-U Langmuir probe interpretation. This could be done by substituting values directly in to eq. (5.7) to either get an initial value for fitting routines or to subtract off the sheath expansion contribution to current and then use a 3-parameter fit.

The effects of wall potential were also investigated. Density measurements at wall

potentials less than floating were found to underestimate compared to the specified plasma density n_0, with an underestimation of collection area due to the change in wall sheath thickness being the cause. A method for inferring this change in sheath thickness was presented, thereby allowing the collection area to be corrected and more accurate density measurements to take place. A model, based on Bergmann's scaling, was fit to this measured profile, but whether this is applicable to other plasma scenarios remains an open question.

Chapter 6

Angular Dependence Measurements on Magnum-PSI

Declaration

Figures 6.3 to 6.6 and the accompanying discussion have previously been published in the author's paper[85].

6.1 Introduction

A probe tip has been designed, based on the successful designs employed on JET and DIII-D, for use in the divertor of the MAST-U tokamak at CCFE. An experiment has therefore been carried out with twofold objectives: (a) confirm that the angled-tip design of the probes mitigates the issues caused by grazing angles of incidence, and (b) assess their performance in different regions of plasma parameter space before the MAST-U experimental campaign. Measurements were taken on the linear device Magnum-PSI at DIFFER, using a 4-probe array with MAST-U-style tips, at a range of plasma parameters and magnetic field configurations. The description of the setup of this experiment and the analysis methods implemented can be found in chapter 4. The results of the experiment are presented here, as well as a discussion on the consequences for the interpretation of Langmuir probes in MAST-U.

6.2 Magnum Plasmas

For the experiment, multiple parameter scans were performed that fall into four categories: (a) an axial scan, (b) incidence angle scans, (c) a density scan, (d) a detachment study (see fig. 4.6 definitions of coordinates scanned over). All plasmas measured were either hydrogen or helium, at B-fields ranging between 0.8T and 1.5T (see fig. 6.1).

Hydrogen plasmas were widely used as this provides the most similar plasma – in terms of ion charge and mass – to the deuterium plasmas used in MAST-U. Deuterium was not chosen because of high cost. Helium plasmas were also used to broaden the range of plasma parameters (chiefly n_e), thereby improving the performance assessment aspect of the experiment. The magnetic field was initially set to 0.8T, as this is the upper end of expected magnetic field strength on MAST-U, but this upper limit was relaxed following a preliminary experiment (see Appendix B) due to the limits placed on temperature by the Magnum source at MAST-U-relevant magnetic field strengths. Additional magnetic field strengths of 1.2T and 1.5T were therefore used. The permutations of magnetic field

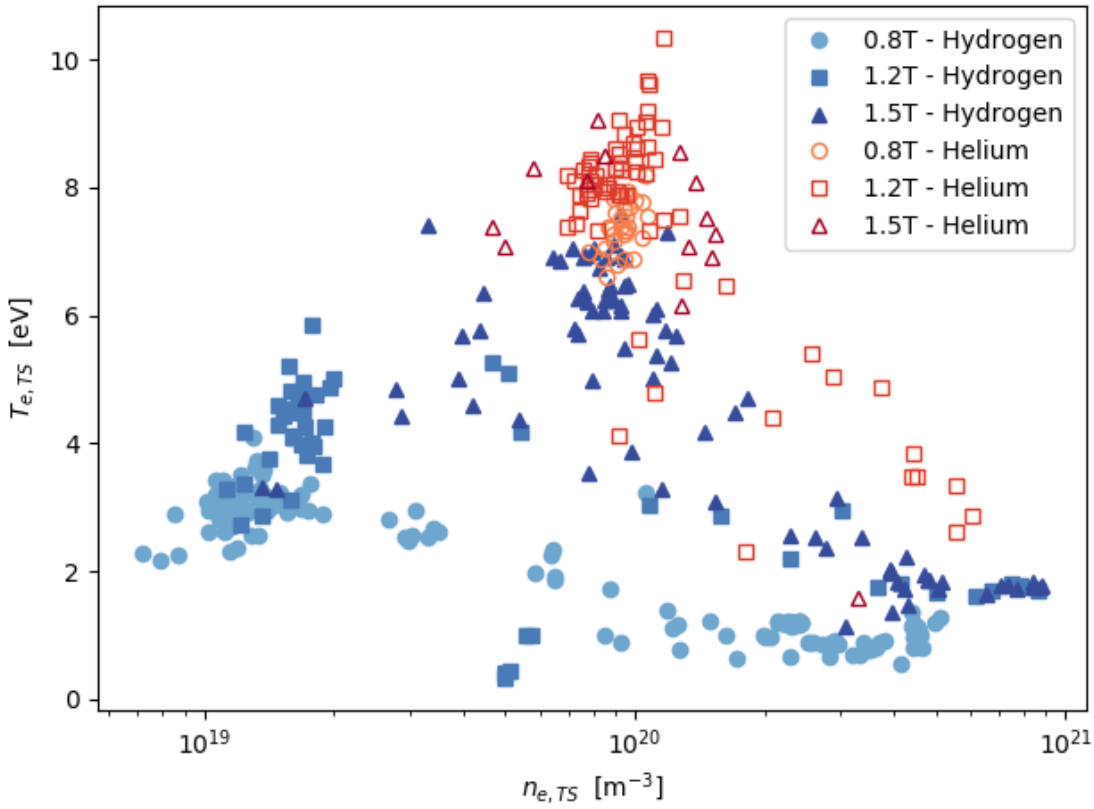

Figure 6.1: Plot of the temperature-density space explored broken down by species and magnetic field strength. Hydrogen plasmas are in solid blue and helium plasmas in hollow red, with 0.8T, 1.2T and 1.5T denoted by circles (○), squares (□), and triangles (△) respectively. The highest peak temperatures (∼10 eV) were achievable using helium at stronger magnetic fields.

strength and plasma species thereby constitute the different scenarios of plasmas measured.

There was some variation within each of these scenarios, as the Magnum source input parameters (source current, source position, and species gas flow) could be adjusted to fine-tune the resultant electron temperature and density. This fine-tuning was generally done to maximise temperature in each scenario, unless otherwise stated, before a measurement took place.

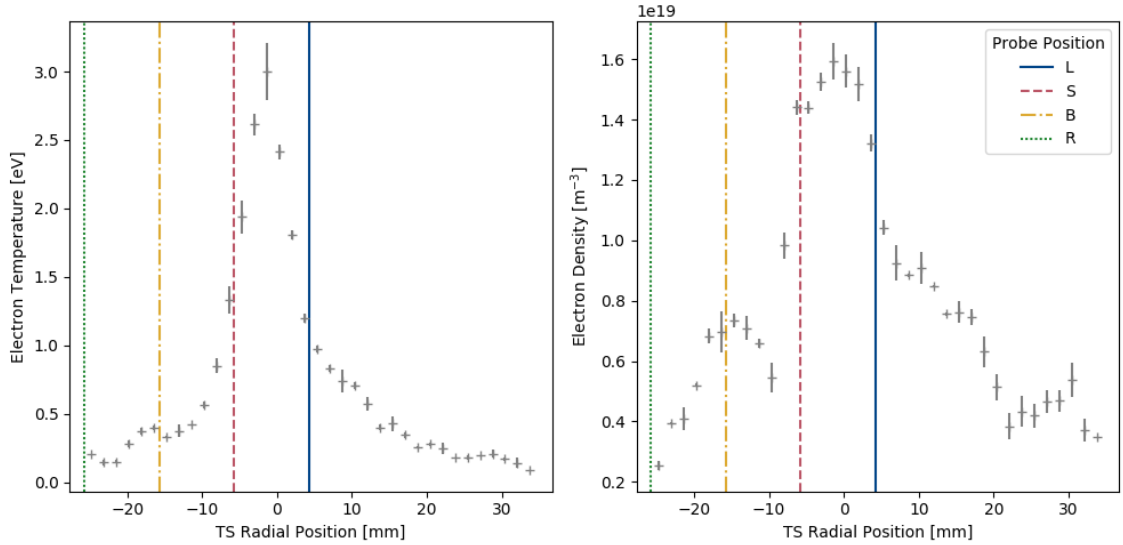

Figure 6.2: Typical Thomson scattering profiles for electron density (left) and temperature (right) for a 0.8T hydrogen shot. Approximate probe locations within this profile are overlaid as vertical lines.

6.3 Results and Discussion

Measurements were made with all four probes, the approximate relative positions of which can be seen in fig. 6.2. The TS values used in analysis are taken as the linearly interpolated value on the TS profile at the approximate radial probe location. In general the S and L were located most centrally and had the greatest signal-to-noise ratio, so these will be discussed in detail. The R and B probes were limited to taking measurements of the wings of the plasma in all shots, and therefore generally collected little current and suffered from low signal-to-noise ratios. This made the IV characteristics much more challenging to interpret, so these probes were excluded from detailed analysis.

6.3.1 Axial Scan

The distance of the probes from the Thomson scattering profile was not constant in all cases, so an axial-scan (along the beam axis) was used to measure the axial density and temperature profiles.

The profile width was not expected to change along the beam axis, but a reduction in

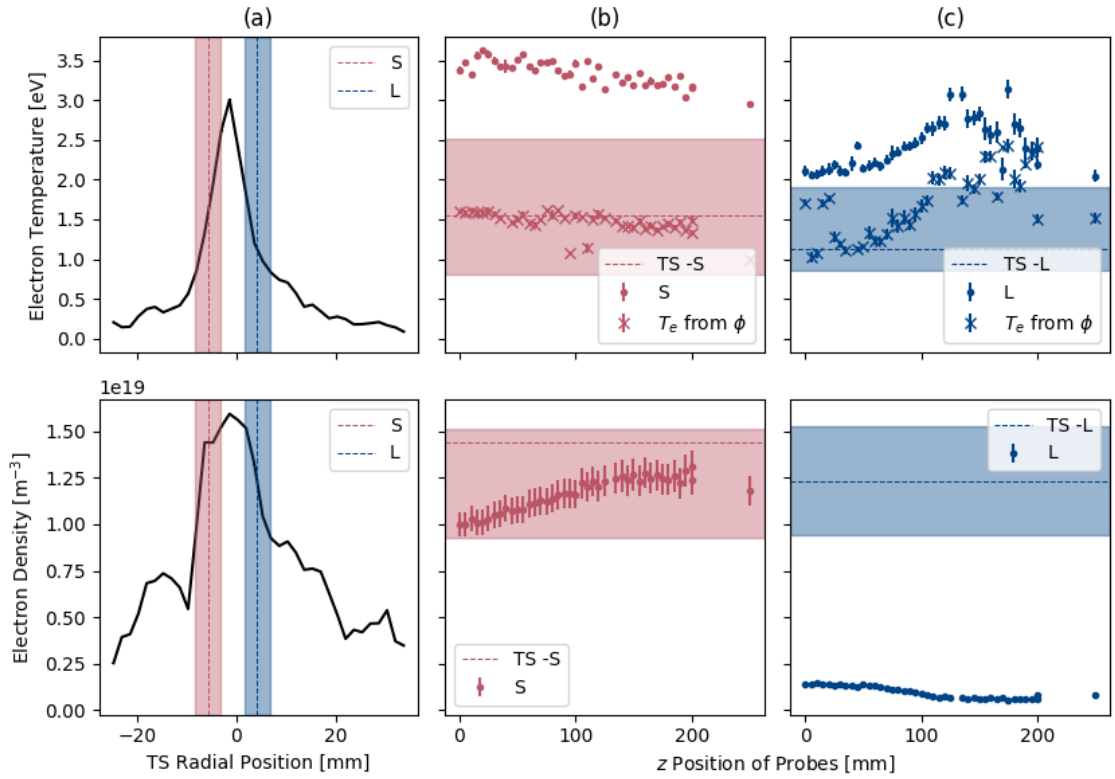

Figure 6.3: Results of the axial-scan, i.e. the probe measurements taken along the Magnum-PSI beam axis. The top and bottom rows show T_e and n_e respectively, with (a) being Thomson scattering profiles, (b) and (c) being the fit parameters from the S and L probes' IVs respectively. The dotted lines and associated bounds indicate the interpolated Thomson scattering measurement at the position of the S (red) and L (blue) probes and the corresponding uncertainty. The different probe measurements show axial density and temperature profiles with opposite trends, implying that the probes are translating through the radial beam profile with increased z. An estimate of T_e gained from measuring the plasma potential from the knee of the IV characteristics is also overlaid.

temperature with distance from the source is expected as energy is radiated away according to particle time-of-flight. The results from this axial scan can be seen in fig. 6.3. The L and S probes measured higher temperatures and lower densities compared to those measured by the TS. This is not unexpected as overestimation of temperature is a common occurrence for Langmuir probe measurements in fusion-relevant plasmas, especially at the low temperatures measured by the TS of $\sim 1 - 1.5$ eV at the location of the probe

measurements. The density measured by the S probe was also in better agreement with the TS measurements than that measured by the L probe.

The S probe sees a decrease of density towards the source whereas the L probe sees an increase. This may be explained by the arm the probes were mounted to not being strictly aligned with the beam (z) axis, and so 'drooping' downwards when extended to reach smaller z. This translates the probes radially through the beam (in the negative radial direction on the TS profiles on (a) in fig. 6.3), pushing the more central S probe out towards the wings, and the L probe closer to the centre.

The temperature profiles show opposite profiles to the density however, with the S probe increasing in temperature as density decreases, and the L probe decreasing in temperature towards the source as the density increases. We would expect the temperature to increase as we approach the source, and it may be that this increase in temperature is enough to counterbalance the small decrease in temperature from moving the probe outwards through the radial profile. The larger temperatures on the L probe however, are likely to be the probe measurements drastically overestimating in the very low temperature and low density plasmas at the wings of the profile. This is therefore evidence that the probe system used has an operational density floor of $\sim 7 \times 10^{17}$ m^{-3} and a temperature floor of ~ 1 eV. This does not necessarily imply the same for the MAST-U probe system however, due to the difference in electronics and sweep waveform used.

For comparison, an estimate of T_e was calculated from each IV characteristic using the equation for the floating potential. The floating potential is an output fit parameter, and at these plasma parameters the knee was visible in the electron region of the IV characteristics so Φ could be directly measured. As such eq. (2.39) can be rearranged and, with the appropriate mass substituted in, an estimate of T_e can be gained. This estimate is not usually considered very accurate[37], but in this case provided a value which showed better agreement with the values measured by the TS.

As most shots were performed between $z = 100 - 200$, which has a broadly flat density and temperature profile, no axial profile corrections were necessary.

6.3.2 Angle Scans

All angle scans covered the range $0 \leq \theta \leq 10^\circ$ (as is expected to be the case in the majority of MAST-U plasmas) in 1° increments. An angle scan was taken at each different combination of magnetic field strength and plasma species, except for 1.5T helium due to

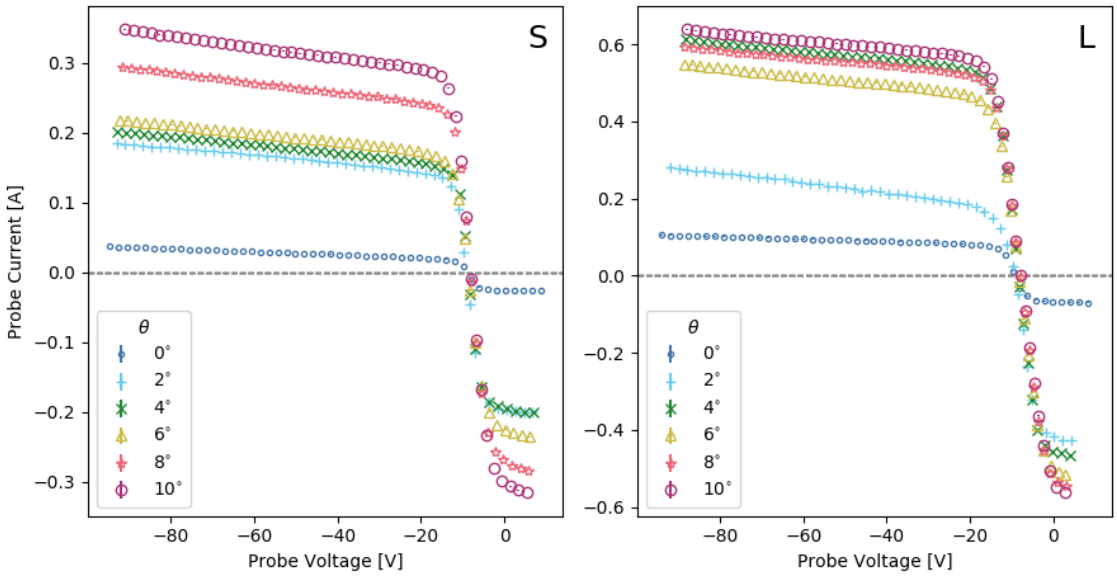

Figure 6.4: Results of the scan over magnetic field incidence angle for the 0.8T hydrogen plasma. The IV characteristics for the L and S probes are shown.

concerns about the peak heat flux.

Let us first examine the hydrogen plasma at 0.8T as this is the magnetic field regime most relevant to MAST-U. The set of IV characteristics can be seen in fig. 6.4. Both L and S probes measured higher temperatures and lower densities when compared to TS measurements. The temperature was greater by a factor of 1 - 4 depending on probe, and the density was lower by a factor of 1 - 8. Density shows good agreement with the TS in some cases, for example on the L probe at larger θ in the 0.8T hydrogen plasma scan. The IV characteristics were also found to either fully saturate, or have very low levels of non-saturation, even at small θ, implying that the design is effectively mitigating sheath expansion effects. In general the S probe seemed to perform better than the L probe when compared to the TS measurements. It is unclear why this would be, as sheath expansion effects should be greater, and therefore more interfering, for the smaller probe where the proportion of the collection area made up of the vertical sheath extent is greater. The inferred temperatures, densities and fitted sheath expansion parameters as a function of incidence angle can be seen in fig. 6.5. There were two notable trends.

Firstly, the density measurements still have a strong θ dependence, with the difference

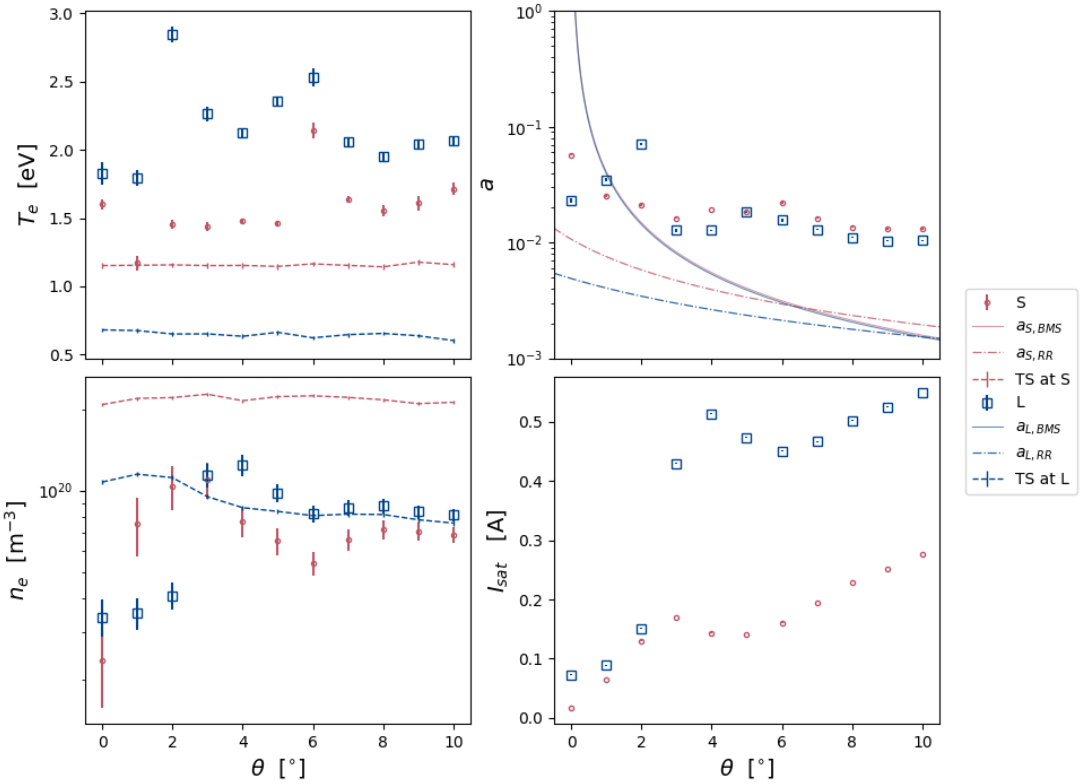

Figure 6.5: The measured plasma parameters for the L (blue) and S (red) probes at each value of θ in the 0.8T hydrogen plasma. T_e is temperature, n_e is electron density, and a is the sheath expansion parameter as per eq. (2.59), and $I_{i,sat}$ is the ion saturation current. The interpolated TS values at each probe's approximate radial position are overlaid for n_e. Both the Bergmann-Murphy-Sugrue (eq. (2.62)) and rotated rectangular (eq. (5.7)) models for sheath expansion are overlaid on the sheath expansion plot, which were calculated using the mean $T_{e,TS}$ and $n_{e,TS}$ for each probe.

between the TS and the Langmuir probes increasing with decreasing θ. The Thomson scattering measurements did record a slight change in density at smaller θ, but this was not large enough to explain this behaviour. This implies that the calculation of A_{coll}, i.e. the geometric area of the unshadowed probe tip projected along the magnetic field, does not accurately describe the probe's actual A_{coll} at small θ. This supports the findings of synthetic density measurements from particle-in-cell simulations in section 5.4.2 (see fig. 5.11).

Secondly, the fitted sheath expansion parameter does not agree with the analytical

value provided by Bergmann and Murphy-Sugrue – this is seen across both probes, but is particularly prevalent at larger θ. The analytical value was calculated from eq. (2.62) as a function of θ and using the mean TS T_e and n_e for each probe. In the case of the S probe the sheath expansion parameter is almost an order of magnitude larger than the analytical value at $\theta = 10$. The S and L probes follow the same rough increasing trend as the analytical case but do not show asymptotic behaviour around $\theta = 0$. This lack of asymptotic behaviour therefore suggests that the angled tip probe is successfully eliminating the strong θ dependence at grazing angles of incidence and that the design appears to be working as intended, but further experimental confirmation – with a non-angled flush probe in the same conditions – would be needed to confirm that the design is working.

As an additional point, the model (eq. (2.62)) is therefore ineffective at predicting the sheath size for the angled probe tip. This is not unexpected, as the theory describes a completely flush probe and does not take into account angling the tip or shadowing the leading edge. A comparison is therefore made to a_{RR} — the sheath expansion parameter for a rotated rectangular sheath on an angled-tip probe as derived in chapter 5. The measured values for the coefficients c_1 and c_2 were used. It appears to be in good agreement with the flatter trend of the measured a profile, showing a slight increase at small θ but avoiding the asymptotic behaviour of eq. (2.62). However, it is still smaller in absolute terms by an order of magnitude, the reason for which is not well understood.

6.3.3 Density Scan

The results from the density scan, performed in order to test the MAST-U Langmuir probe tip's operational parameter space, can be seen in fig. 6.6. Measurements were taken with the S and L probes at two angles, $\theta = 8°$ and $\theta = 10°$, in plasma densities ranging from 1×10^{19} - 2×10^{20}.

The ratio between the Langmuir probe measurements and the TS measurements ($\frac{T_{e,Probe}}{T_{e,TS}}$) did show some dependence on both electron density and θ. The temperature ratio for the S probe at $\theta = 8°$ is roughly constant at ~ 1 across most densities. At $\theta = 10°$ the same is true, except at very high densities where the ratio starts to increase i.e. the Langmuir probes are measuring a much larger T_e than the TS. At the lowest densities (9×10^{18} - 2×10^{19}) and at both angles the T_e measured by the S probe is also larger than TS measurements by up to 50%. For the L probe however there is a much higher temperature measurement ratio for most densities, which for $\theta = 8°$ reduces at higher densities. However for $\theta = 10°$,

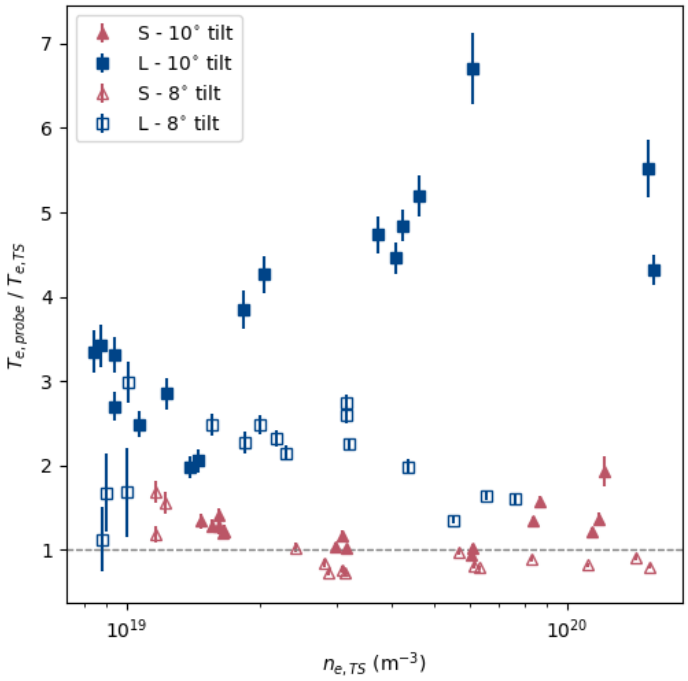

Figure 6.6: The temperature overestimation factor plotted as a function of TS density at probe radial position, for the S (triangles) and L (squares) probes at $\theta = 8°$ (empty) and $\theta = 10°$ (filled). The shots at $\theta = 10$ on both probes show increasing overestimation of temperature at high densities.

the ratio is much larger throughout and becomes greater at the highest densities, increasing up to 6 times greater than the interpolated TS value at the probe position. This is an unexpected result as sheath expansion should affect temperature overestimation less at larger angles. The only difference in configuration between the 8° and 10° cases is that the 1mm height difference between the fore- and rear-wall is not enough to shadow the rear wall leading edge for $\theta > 8.1°$. There is therefore an exposed leading edge in the 10° case which could be sputtering impurities into the plasma around the probes and interfering with the current collection. This would suggest that $\theta > 8°$ is an upper limit on the reliable operational range for the L probe, although similar density scan measurements made at a greater range of angles would be required to conclude this definitively. The L probe is installed throughout the MAST-U divertor, but an upper limit of $\theta = 8°$ would only prevent measurements being made at the very outer probe locations for conventional and Super-X plasma configurations.

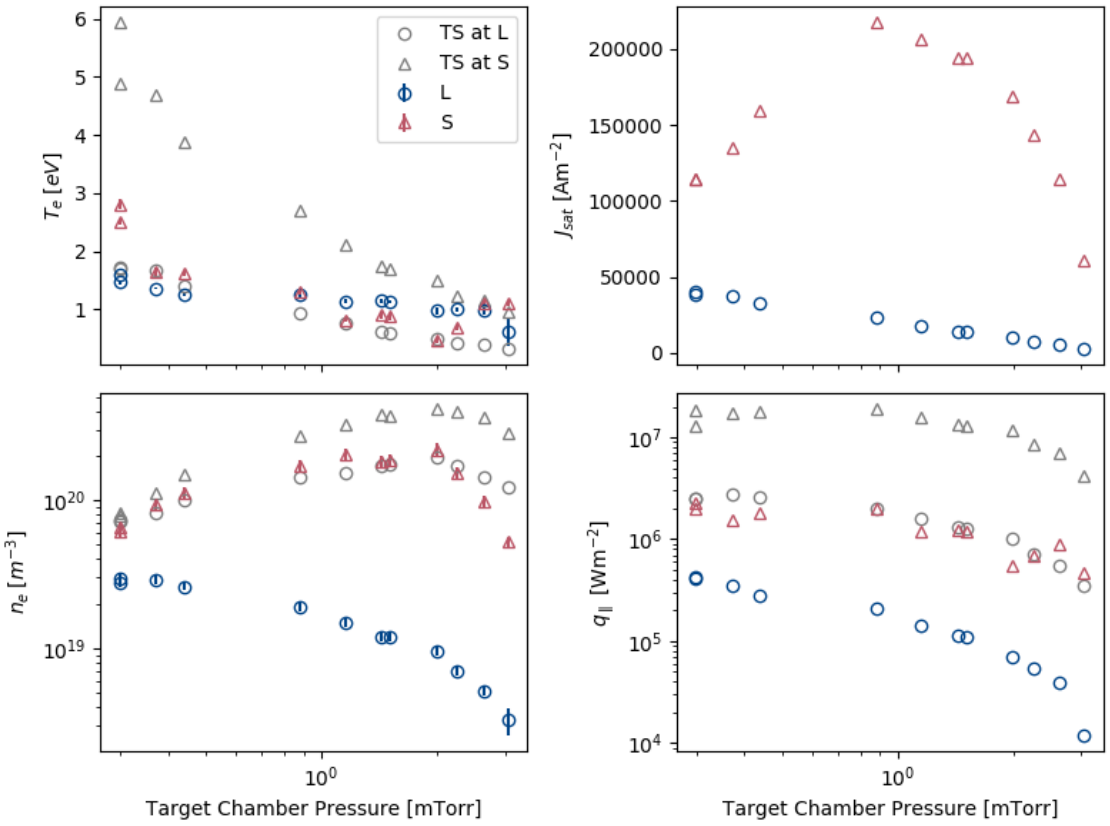

Figure 6.7: The results of the detachment study using probes S and L in a 1.5T hydrogen plasma at $\theta = 8°$. A flux rollover can be seen in both the probe and TS density data, with the later TS rollover peak implying a moving detachment front along the beam.

6.3.4 Detachment Study

A study of the probes' performance in a detached scenario was also performed, by scanning over increasing neutral density in front of the target. This was achieved by first lowering the pumping speed (the first three measurements) and then by puffing increasing quantities of hydrogen at the target. The results of this study can be seen in fig. 6.7.

Firstly, a peak is visible in the measurements of density for both the TS and probe measurements. The position of the peak is different for the two probe measurements however, with the L probe density dropping immediately with increasing pressure while the S probe measurements show a delayed peak at $\sim$ 1mTorr. The TS, both at the L

and S probe positions appears to peak at 2mTorr. This implies a moving detachment front that travels first from the outside toward the centre of the beam at the target and then rapidly away from the target towards the TS position $\sim$ 200mm. This implication is supported by the fact that the probe density measurements show better agreement with the TS measurements at low neutral pressure.

The saturation current density J_{sat} and the parallel heat flux $q_{\parallel}$ are also plotted, in the latter case calculated with $\gamma = 7$. J_{sat} shows a similar rollover to the density measurements, with a slightly earlier peak on the S probe than seen in the density measurements. It is still clear that the L probe, measuring in the wings of the beam, sees a decrease before the S probe. The heat flux measurements show a significant drop with increasing pressure, but does not decrease completely to 0. We are therefore not looking at full detachment, only the beginning stages. This constitutes evidence therefore that the MAST-U Langmuir probe system can feasibly detect the onset of detachment at the target.

We can see a decrease in temperature, measured by both the probes and the TS as neutral pressure is increased. In a departure from the lower magnetic field measurements, the probes in this case appear to be underestimating the temperature compared to the TS measurements, or in agreement with TS in the case of low pressure L probe measurements. As neutral pressure is increased this underestimation shrinks and then becomes an overestimation. The underestimation compared to the TS measurements is curious as the opposite is usually true when taking measurements in magnetised plasmas – as borne out by the measurements taken at lower magnetic field. This is likely a compounding effect of taking measurements in higher magnetic field and with higher temperature. Though the magnetic field would not be this high on MAST-U, this is nevertheless a regime relevant to MAST-U measurements if we look at the magnetisation parameter for the range of densities. We find that $\xi > 10$ for all measurements, so we are still in the partially magnetised regime and therefore would expect magnetised probe theory to still be relevant. The temperature measurements are therefore likely correct to within the same degree of accuracy as previous measurements at lower B-field. This result therefore implies the existence of a strong temperature gradient between the probes and the TS position which is reduced as the neutral pressure increases and the detachment front moves upstream.

6.4 Summary

An experiment has been carried out on Magnum-PSI at DIFFER to both verify the MAST-U probe's angled tip design and to study how it performs within typical conditions expected in the MAST-U divertor.

Results have shown that density measurements decrease with decreasing θ when compared to the TS measurements. This implies that there remains dependence on magnetic field incidence angle after accounting for projected collection area, and therefore that the effective collection area is being overestimated at small θ.

Further to this, the flat profile of the measured sheath expansion parameters implies that sheath expansion is being mitigated successfully at small θ, although additional comparisons to FMP measurements would be needed to confirm this. This is in contrast to the predicted values from Bergmann and Murphy-Sugrue's models for a flush-mounted probe, which still predict asymptotic behaviour as $\theta \to 0$. The measured values show better agreement with the sheath expansion parameter derived for a rotated rectangular sheath, though are still larger than predicted values by an order of magnitude.

The operational range has been evaluated in terms of temperature measurement compared to the TS system on Magnum-PSI. Results have shown inconsistencies at the upper end of the expected magnetic field incidence angles in MAST-U (10°), with measured temperatures being up to 6 times greater than the TS compared to an equivalent 8° case. This therefore appears to be an upper limit on reliable temperature measurement, particularly at high densities (1×10^{20}) and low temperatures (1eV), but this should be confirmed through further measurements at a greater range of angles.

The MAST-U Langmuir probe design has therefore been successfully verified to be working as intended and the probe system will be able to accurately measure temperatures at the small angles of magnetic field incidence expected in the MAST-U divertor. A similar comparison is planned between the Langmuir probes and divertor Thomson scattering systems on MAST-U to confirm these findings.

Chapter 7

Conclusions and Future Work

7.1 Conclusions

In this thesis, a body of work characterising and verifying the performance the MAST-U angled-tip probe design has been presented. This has been carried out through both computational means – in the form of particle-in-cell simulations – and experimental means – in the form of a series of B-field incidence angle scans and density scans on the linear plasma device Magnum-PSI.

Two re-derivations of Bergmann's sheath expansion parameter were presented with two alternative assumptions of the 2D sheath shape around an angled tip probe: a rotated rectangle and a parallelogram. Both take into account the angle of the probe tip θ_p and the depth of the recession of the leading edge of the probe d_{perp}. The rotated rectangular model also requires a small correction for the difference in height caused by rotating the sheath, and so has a small dependence on Δ_0 – the sheath size at floating potential.

Simulations were performed on the 2D3V particle-in-cell code SPICE of both a flush-mounted probe and an angled-tip probe with MAST-U-like length, gapsize and plasma parameters. This was done to gain values for the coefficients in the sheath expansion models, and to investigate the effect of changing the wall potential in front of the probe. For the rotated-rectangular sheath model, the coefficients were found to be $c_1 = 2.6$ and $c_2 = 0.53$ for the flush-mounted probe, showing agreement with Bergmann and Murphy-Sugrue in the latter but not in the former. The coefficients for the angled-tip probe were found to be $c_1 = 2.3$ and $c_2 = 0.55$. With these values, the level of sheath expansion for some given plasma parameters can now be predicted. Such predictions of a could be used in MAST-U probe analysis techniques to either provide initial parameters to fitting functions or to subtract off the predicted sheath expansion contribution to the ion current, allowing a 3-parameter model to be used instead.

The investigation of the fore-wall potential revealed that an additional current manifests at $V_w < V_{fl}$ which must be accounted for to assure accurate density measurements. This current is caused by an increase in collection area which scales with $\Delta_0 - \Delta_w$. A method for directly measuring this value was presented, allowing the synthetic density measurements to be properly corrected for in this simulated case. This method of current subtraction could also be used experimentally to either account for the difference in collection area at a specific V_w or to directly measure the sheath size in front of the wall.

Experimental measurements were also performed on the Magnum-PSI linear device at DIFFER. Incidence angle scans and density scans were carried out to assess probe

performance in conditions relevant to expected MAST-U operational space. This was done using a 4-probe array from the MAST-U divertor science facility with 4 MAST-U-like angled-tip probes.

The angular dependence measurements, for $0° \leq \theta \leq 10°$, showed higher temperatures and lower densities than those measured by the Magnum-PSI Thomson scattering (TS) system. Some probes showed good agreement with the TS density measurements at larger θ, but there existed some angular dependency which was not accounted for by the projected area calculations, leading to decreased n_e measurements with decreasing θ. The measured values of sheath expansion parameter a showed a flat profile at small θ when compared with the predicted values from the Bergmann-Murphy-Sugrue model, which is asymptotic around $\theta = 0$. This therefore constitutes evidence that the probe design is successfully mitigating sheath expansion at small angles. The measured values of a showed better agreement with the rotated rectangular sheath model a_{RR}, but were consistently larger by a factor of 5, implying some gap in the theory.

The density scan measurements, for $1 \times 10^{19} \leq n_e \leq 2 \times 10^{20}$, showed similarly higher temperatures on the probe measurements than the TS measurements. This effect was found to be dependent on the density, with overestimation growing with increasing density. The probe angle was also found to have an effect, with measurements at 8° showing significantly lower temperatures compared to measurements taken at 10° in equivalent density plasmas. These angles correspond to measurements taken with the vertical face of the rear tile exposed to plasma ($\theta = 10°$) or effectively shadowed ($\theta = 8°$), with the transition occurring at $\sim 8.1°$. This therefore potentially points to an operational upper limit on MAST-U probe measurements of $\theta = 8°$, though further experimental evidence at a wider range of angles would be needed to confirm this.

7.2 Future Work

There are several suggestions and unanswered questions that were beyond the remit of this body of work, but nevertheless deserve mention as possible areas of future investigation.

The experimental measurements raise several questions, notably how best to account for the remaining θ dependency in the measurements of n_e. This could quite neatly be addressed through a similar analysis of MAST-U probe data at a range of angles in similar plasma conditions. This density dependence could then be investigated more thoroughly, and answer the question of whether it points to a larger issue with estimating probe

collection area at small θ. Similarly, the operational range limitation would benefit from being reproduced at a greater range of angles to see whether the hypothesis of an exposed leading edge on the rear tile has merit.

The cause for the order of magnitude difference between prediction and measurement for the sheath expansion parameter is an open question. Even when using the improved model of sheath expansion for an angled-tip probe, the measured value is still larger by a factor of 5. This implies that something is missing from the formulation of the sheath expansion parameter as described by Bergmann. It has been suggested[86] that an alternative form of IV characteristic could be used that takes into account the 3D expansion of the sheath, which could prove an interesting avenue of investigation. This would require 3D simulations that could feasibly be run on the fully 3D version of SPICE given enough time and computational resource.

Finally, a method was demonstrated that could be used to directly measure the sheath size of the wall in front of the probe. The computational usage of this technique in this thesis was limited, so it could be future work to run this same analysis at a range of plasma conditions and in so doing derive a better general expression for Δ_0. It would also be of great interest to conduct this technique experimentally. This could be done by two measurements on a single probe in identical plasma conditions – Magnum-PSI, or any other linear device with strict control over θ, would be an option. Alternatively a new design of probe could be forthcoming wherein two probes, situated closely together, akin to the DSF probe tip, take measurements in the same plasma with two separate, independently biasable fore-wall sections to control V_w. Either of these approaches would constitute a method of directly measuring the sheath height and therefore experimentally verifying the proportional relationships at the core of Bergmann's sheath expansion model.

Appendices

Appendix A

Climate Change and the Role of Fusion

At the time of writing, economies comprising 50% of the world's GDP are now committed to reducing their net carbon emissions to zero by 2050 or before. Therefore, it stands to reason that the expected growth in energy demand, as well as the eventual replacement of existing high carbon energy supply, will be fulfilled by low carbon sources to avoid the worst effects of climate change.

Predicting the exact makeup of the energy mix that will meet this demand is therefore of great interest. Most sources[87, 88], including fossil fuel company British Petroleum[89], project that renewable sources (e.g. solar photovoltaics (PV) and wind turbines) will make up a majority of the global energy mix by 2050. The Committee on Climate Change in the UK projects that a 78% renewables fraction is "desirable", and even a "cautious" approach would result in a share of *only* 60%[90]. This is largely based on a dramatic fall in the price of renewables in recent years, with the levelised cost of energy (LCOE) falling to ∼50$/MWh for large solar PV, 56$/MWh for onshore wind and 92$/MWh for offshore wind, assuming the upper end of each range [88]. For comparison, the lowest estimate of the LCOE of new-build nuclear is 120$/MWh.

It would be wise then to assume that renewables will constitute a high fraction of the grid by the latter half of this century. This will drastically change grid structure, and the other low carbon sources filling the remainder of supply will likely have to fit around the intermittent nature of renewable generation. Currently the available options are nuclear fission and natural gas with carbon capture and storage – however other as-

	Intermittent Renewables (wind + solar)	**Gas + CCS**	**Fission** (e.g. PWR)	**Gen IV Fission** (e.g. Sodium-cooled fast reactor)	**Fusion**	**Fission-Fusion Hybrid**
LCOE	cheap (excluding energy storage)	medium	expensive	expensive	expensive	expensive (but < fusion)
Long-term waste	no nuclear	CO_2 storage	high-level nuclear	high-level nuclear (but spent nuclear fuel < fission)	likely intermediate-level nuclear	high-level nuclear
Nuclear safety risk	no nuclear risk	no nuclear risk	meltdown risk	meltdown risk, but passively-contained	risk of nuclear accident, but not meltdown	risk of nuclear accident, but not meltdown
Weapons proliferation risk (fissile material on site)	no	no	yes	yes	no (but tritium produced)	yes
Resource constraints	rare-earth metals (depends on substitutability)	gas reserves	Uranium-235	Can use Uranium-238	Lithium, but possibly Beryllium	Can use Uranium-238
Scalability	require intermittency solutions at high penetrations	limited by CO_2 storage locations	high	high	high	high
Areal energy density	low	high	high	high	high	
Load-following	no	fast	rate-limited by thermal inertia	rate-limited by thermal inertia	rate-limited by thermal inertia	rate-limited by thermal inertia
Heat production	no	T limited by technology	yes	yes	yes	
Burn actinide waste?	no	no	yes	yes	yes	
EROI	~ 50 (wind without storage) ~ 20 (solar without storage)	~ 40	~ 85	$\lesssim$ 170	$\lesssim$ 170	$\lesssim$ 170
Technology readiness level (TRL)	9	8	9	8/9	2/3	3/4

Table A.1: Various advantages and disadvantages of fusion relative to other low carbon energy sources. From [4].

yet-undemonstrated technologies should also be included: nuclear fusion, 4th generation nuclear fission, advanced geothermal, and fission-fusion hybrid devices. A recent paper[4], coauthored by the author of this thesis, discusses the relative advantages and disadvantages of these various firm, low carbon energy generation technologies, summarised in table A.1.

Appendix B

Preliminary Experiment on Magnum-PSI

A preliminary experiment was performed a year in advance of the full set of experiments and Magnum-PSI. Its aim was to test the functionality of the equipment and to uncover any unforeseen difficulties in the experimental plan. Three problems were discovered and either remedied or mitigated:

1. **Design of the DSF probe head.** The "pin-holder", i.e. the two-part piece of insulating material beneath the exterior graphite shell which isolates each probe from both the graphite shell and the other probes, was made of a material which proved to be unsuitable. High-temperature polyether ether ketone (PEEK) was originally chosen for the purpose as it had been used successfully several times on MAST, but was unfit for two reasons: (a) the unaccounted-for higher linear thermal expansion coefficient than the other graphite components, and (b) an insufficiently high melting temperature for Magnum-PSI experimental conditions. Due to (a), the PEEK pin holder expanded and pressed against the outer graphite shell during an initial vacuum bake, causing the graphite shell to break into three pieces. While the probe head was still able to be held together, this breakage likely significantly reduced the thermal conductivity of the pyrolytic graphite during the experiment which, along with (b), contributed to problems with (2).

2. **The operating temperature of the probe head and mount assembly.** Partly due to (1), and partly due to the presence of a leading edge between the DSF probe

head and the mounting assembly, the surface temperature of the graphite regularly exceeded 1800°C when measured using the Magnum-PSI infrared camera. This surface temperature was high enough that the temperature of the pin holder exceeded the melting point of PEEK and caused partially melted PEEK to flow into the gaps between the probes and the cracks of the graphite shell. This surface temperature was also high enough that we would expect to see the graphite shell 'bloom' i.e. release large quantities of carbon into the plasma – this was born out by an enhanced methane line on the spectrometer. The PEEK that flowed between the probes was exposed to plasma and, whether by burning or being sputtered with graphite, became electrically conductive and shorted two of the four probes – rendering them unusable for the remainder of the experiment.

3. **Magnum source limitations** The experiment planned to explore MAST-U relevant plasmas and thus limited the range of magnetic fields to those achievable on MAST-U: 0.5-0.8T. It was discovered however that the Magnum source has issues creating low density (1×10^{18}-1×10^{19} m^{-3}) and high temperature plasmas (> 5 eV) at those magnetic fields. Plasmas with higher density (1×10^{20} m^{-3}) were possible but came at the expense of lowering the peak temperature (~ 0.5eV – significantly lower than optimal operating temperature for LPs of ~ 5 eV).

The solution to (1) was to redesign the pin holder with an alternative material choice. A high temperature, machinable ceramic was chosen. This also partially solved (2) as the graphite shell would not break upon vacuum baking, improving thermal conductivity and therefore cooling capacity. Before the main experiment, the leading edge between the mounting assembly and the probe head was removed by filing down an edge on the mount so that the probe head sat lower compared to the mount. This successfully lowered the surface temperature of the probes and prevented blooming. To solve (3), the limits placed on the magnetic field were relaxed so as to access higher temperature regimes where the probes would be expected to measure temperature more accurately.

Despite these issues a series of measurements was able to be performed using the L and S probes in a study of detachment, where at a fixed probe position and plasma state the neutral pressure of the plasma was increased – to investigate both the plasma response and the sensitivity of the probes to that response. The results show similar findings to those presented in section 6.3.4.

References

[1]IEA, *World Energy Outlook 2019*, tech. rep. (IEA, 2019).

[2]V. Masson-Delmotte, P. Zhai, H. Pörtner, D. Roberts, J. Skea, P. Shukla, A. Pirani, W. Moufouma-Okia, C. Péan, R. Pidcock, S. Connors, J. Matthews, Y. Chen, X. Zhou, M. Gomis, E. Lonnoy, T. Maycock, M. Tignor, and T. Waterfield, "Ipcc, 2018: global warming of 1.5c. an ipcc special report on the impacts of global warming of 1.5c above pre-industrial levels and related global greenhouse gas emission pathways, in the context of strengthening the global response to the threat of climate change, sustainable development, and efforts to eradicate poverty", In Press. (2018).

[3]C. A. Horowitz, "Paris agreement", International Legal Materials **55**, 740–755 (2016).

[4]T. E. G. Nicholas, T. P. Davis, F. Federici, J. Leland, B. S. Patel, C. Vincent, and S. H. Ward, "Re-examining the role of nuclear fusion in a renewables-based energy mix", Energy Policy **149**, 112043 (2021).

[5]J. D. Lawson, "Some Criteria for a Useful Thermonuclear Reactor", Atomic Energy Research Establishment, 1–12 (1955).

[6]F. Chen, *Introduction to Plasma Physics and Controlled Fusion* (Springer International Publishing, 2016).

[7]L. A. Artsimovich, "Tokamak devices", Nuclear Fusion **12**, 215–252 (1972).

[8]J. Wesson and D. J. Campbell, *Tokamaks* (Oxford University Press, 2011), p. 812.

[9]I. Voitsekhovitch, B. Alper, M. Brix, R. V. Budny, P. Buratti, C. D. Challis, J. Ferron, C. Giroud, E. Joffrin, L. Laborde, T. C. Luce, D. McCune, J. Menard, M. Murakami, and J. M. Park, "Non-inductive current drive and transport in high βn plasmas in JET", Nuclear Fusion **49** (2009).

[10]A. Barke, M. Cox, J. Harbar, J. Hay, J. Hicks, J. Hill, D. Hurford, J. McKenzie, A. Morris, M. Nightingale, T. Todd, G. Voss, and J. Watkins, "The Mega Amp Spherical Tokamak", in Proceedings of 16th international symposium on fusion engineering, Vol. 2 (1995), pp. 1456–1459.

[11]R. Aymar, P. Barabaschi, and Y. Shimomura, "The ITER design", Plasma Physics and Controlled Fusion **44**, 519–565 (2002).

[12]F. Romanelli, *Fusion Electricity - A roadmap to the realisation of fusion energy*, tech. rep. (EU-EFDA, 2012).

[13]G. Fishpool, J. Canik, G. Cunningham, J. Harrison, I. Katramados, A. Kirk, M. Kovari, H. Meyer, and R. Scannell, "MAST-upgrade divertor facility and assessing performance of long-legged divertors", Journal of Nuclear Materials **438**, S356–S359 (2013).

[14]P. M. Valanju, M. Kotschenreuther, S. M. Mahajan, and J. Canik, "Super-X divertors and high power density fusion devices", in Physics of plasmas, Vol. 16, 5 (2009).

[15]J. Mlynář, *Focus On: JET The European Centre of Fusion Research*, tech. rep. (2007).

[16]G. F. Matthews, "Plasma detachment from divertor targets and limiters", Journal of Nuclear Materials **220-222**, 104–116 (1995).

[17]E. Havlí, H. Havlíčkov, H. Havlíčková, W. Fundamenski, M. Wischmeier, G. Fishpool, and A. W. Morris, "Plasma Physics and Controlled Fusion Investigation of conventional and Super-X divertor configurations of MAST Upgrade using scrape-off layer plasma simulation Related content Investigation of conventional and Super-X divertor configurations of MAST Upgrade using scrape-off layer plasma simulation", Plasma Physics and Controlled Fusion Plasma Phys. Control. Fusion **56**, 75008 (2014).

[18]MAST-U, *MAST Upgrade Research Plan*, tech. rep. 5 (CCFE, 2015), pp. 1–25.

[19]I. Langmuir, "The effect of space charge and resdual gases on thermionic currents in high vacuum", Physical Review **2**, 450 (1913).

[20]G. F. Matthews, "Tokamak plasma diagnosis by electrical probes", Fusion **36**, 1595–1628 (1994).

[21]J. Lovell, R. Stephen, S. Bray, G. Naylor, S. Elmore, H. Willett, M. Peterka, M. Dimitrova, A. Havranek, M. Hron, and R. Sharples, "A compact, smart Langmuir Probe control module for MAST-Upgrade", Journal of Instrumentation **12**, C11008–C11008 (2017).

[22]A. Kirk, T. Eich, A. Herrmann, H. W. Muller, L. D. Horton, G. F. Counsell, M. Price, V. Rohde, V. Bobkov, B. Kurzan, J. Neuhauser, and H. Wilson, "The spatial structure of type-I ELMs at the mid-plane in ASDEX Upgrade and a comparison with data from MAST", Plasma Physics and Controlled Fusion **47**, 995–1013 (2005).

[23]T. W. Morgan, M. A. Van Den Berg, G. De Temmerman, S. Bardin, D. U. Aussems, and R. A. Pitts, "Power deposition on misaligned castellated tungsten blocks in the Magnum-PSI and Pilot-PSI linear devices", Nuclear Fusion **57**, 126025 (2017).

[24]A. Bergmann, "Two-dimensional particle simulation of Langmuir probe sheaths with oblique magnetic field", Physics of Plasmas **1**, 3598–3606 (1994).

[25]M. Komm, J. Adamek, R. Dejarnac, J. P. Gunn, and Z. Pekarek, "Transport of electrons in the tunnel of an ion sensitive probe", Plasma Physics and Controlled Fusion **53**, 015005 (2011).

[26]I. Langmuir, "Positive ion currents from the positive column of mercury arcs", Science **58**, 290–291 (1923).

[27]H. M. Mott-Smith and I. Langmuir, "The theory of collectors in gaseous discharges", Physical Review **28**, 727–763 (1926).

[28]B. Labombard and L. Lyons, "Mirror Langmuir probe: A technique for real-time measurement of magnetized plasma conditions using a single Langmuir electrode", Review of Scientific Instruments **78**, 073501 (2007).

[29]C. Vincent, W. McCarthy, T. Golfinopoulos, B. Labombard, R. Sharples, J. Lovell, G. Naylor, S. Hall, J. Harrison, and A. Q. Kuang, "The digital mirror Langmuir probe: Field programmable gate array implementation of real-time Langmuir probe biasing", Review of Scientific Instruments **90** (2019).

[30]H. De Oliveira, P. Marmillod, C. Theiler, R. Chavan, O. Février, B. Labit, P. Lavanchy, B. Marlétaz, and R. A. Pitts, "Langmuir probe electronics upgrade on the tokamak à configuration variable", Review of Scientific Instruments **90** (2019).

[31]R. D. Monk, "Langmuir Probe Measurements in the Divertor Plasma of the JET Tokamak by", PhD thesis (1996).

[32]A. Brockhaus, C. Borchardt, and J. Engemann, "Langmuir probe measurements in commercial plasma plants", Plasma Sources Science and Technology **3**, 539–544 (1994).

[33]I. H. (H. Hutchinson, *Principles of Plasma Diagnostics* (Cambridge University Press, Cambridge, 2002), p. 440.

[34]D. Bohm, "Minimum ion kinetic energy for a stable sheath", in R. Wakerling and A. Guthrie, *The characteristics of electrical discharges in magnetic fields* (McGraw-Hill, 1949) Chap. 3.

[35]L. Tonks and I. Langmuir, "A general theory of the plasma of an arc", Physical Review **34**, 876–922 (1929).

[36]K. U. Riemann, "Bohm criterion and sheath formation", Journal of Physics D: Applied Physics **24**, 493–518 (1991).

[37]P. Stangeby, *The Plasma Boundary of Magnetic Fusion Devices*, Series in Plasma Physics (CRC Press, Jan. 2000).

[38]A. Bergmann, "Two-dimensional particle simulation of the current flow to a flush-mounted Langmuir probe in a strong oblique magnetic field", Citation: Physics of Plasmas **9** (2002).

[39]S. Elmore, "Scrape-off layer ion temperature measurements on MAST by retarding field energy analyser", PhD thesis (2013).

[40]S. Y. Allan, S. Elmore, G. Fishpool, and B. Dudson, "Ion temperature measurements of L-mode filaments in MAST by retarding field energy analyser", Plasma Physics and Controlled Fusion **58**, 45014 (2016).

[41]R. Chodura, "Plasma-wall transition in an oblique magnetic field", The Physics of Fluids **25**, 1628–702 (1982).

[42]S. Riyopoulos, "Unstable particle drift across a magnetic field caused by oblique electric field gradients", Physics of Plasmas **3**, 4355–4359 (1996).

[43]P. C. Stangeby, "The Chodura sheath for angles of a few degrees between the magnetic field and the surface of divertor targets and limiters", Nuclear Fusion **52**, 083012 (2012).

[44]D. Coulette and G. Manfredi, *Kinetic simulations of the Chodura and Debye sheaths for magnetic fields with grazing incidence*, tech. rep. (2016).

[45]P. C. Stangeby, "Determination of T e from a Langmuir probe in a magnetic field by directly measuring the probe's sheath drop using a pin-plate probe", Plasma Phys. Control. Fusion Plasma Phyr. Control. Fusion **37**, 1337–1347 (1995).

[46]D. Bohm, E. G. S. Burhop, and H. S. W. Massey, "The use of probes for plasma exploration in strong magnetic fields", in R. Wakerling and A. Guthrie, *The characteristics of electrical discharges in magnetic fields* (McGraw-Hill, 1949) Chap. 2.

[47]G. F. Matthews, S. J. Fielding, C. S. Pitcher, P. C. Stangeby, G. M. Mccracken, and M. Ulrickson, "Investigation of the fluxes to a surface at grazing angles of incidence in the tokamak boundary", Plasma Phys. Control. Fusion **32** (1990).

[48]P. C. Stangeby, "A problem in the interpretation of tokamak Langmuir probes when a fast electron component is present", Plasma Physics and Controlled Fusion **37**, 1031 (1995).

[49]J. P. Gunn, "The influence of magnetization strength on the sheath: Implications for flush-mounted probes", Physics of Plasmas **4**, 4435 (1997).

[50]C. D. Child, "Discharge from hot cao", Physical Review (Series I) **32**, 492–511 (1911).

[51]J. P. Gunn, C. Boucher, B. L. Stansfield, and S. Savoie, "Flush-mounted probes in the divertor plates of Tokamak de Varennes", Citation: Review of Scientific Instruments **66** (1995).

[52]M. Weinlich and A. Carlson, "Flush mounted Langmuir probes in an oblique magnetic field", Citation: Physics of Plasmas **4** (1997).

[53]S. Murphy-Sugrue, "Numerical Simulations of Probes in Magnetised Plasma", PhD thesis (University of Liverpool, 2017).

[54]R. L. Morse and C. W. Nielson, "Numerical simulation of warm two-beam plasma", Physics of Fluids **12**, 2418–2425 (1969).

[55]C. K. Birdsall and A. B. Langdon, *Plasma physics via computer simulation* (Taylor & Francis, 2005), p. 479.

[56]R. L. Morse and C. W. Nielson, "Numerical simulation of the Weibel instability in one and two dimensions", Physics of Fluids **14**, 830–840 (1971).

[57]C. K. Birdsall and D. Fuss, "Clouds-in-clouds, clouds-in-cells physics for many-body plasma Simulation", Journal of Computational Physics **135**, 141–148 (1997).

[58]A. B. Langdon and C. K. Birdsall, "Theory of plasma simulation using finite-size particles", Physics of Fluids **13**, 2115–2122 (1970).

[59]J. P. Boris, "Relativistic plasma simulation-optimization of a hybrid code", Proceeding of Fourth Conference on Numerical Simulations of Plasmas (1970).

[60]H. Qin, S. Zhang, J. Xiao, J. Liu, Y. Sun, and W. M. Tang, "Why is Boris algorithm so good?", Physics of Plasmas **20**, 084503 (2013).

[61]R. Courant, K. Friedrichs, and H. Lewy, "Über die partiellen Differenzengleichungen der mathematischen Physik", Mathematische Annalen **100**, 32–74 (1928).

[62]R. Courant, K. Friedrichs, and H. Lewy, "On the Partial Difference Equations of Mathematical Physics", IBM Journal of Research and Development **11**, 215–234 (1967).

[63]R. Dejarnac and J. P. Gunn, "Kinetic calculation of plasma deposition in castellated tile gaps", Journal of Nuclear Materials **363-365**, 560–564 (2007).

[64]R. Dejarnac, M. Komm, J. Stöckel, and R. Panek, "Measurement of plasma flows into tile gaps", Journal of Nuclear Materials **382**, 31–34 (2008).

[65]R. Dejarnac, M. Komm, J. P. Gunn, and R. Panek, "Power flux in the ITER divertor tile gaps during ELMs", Journal of Nuclear Materials **390-391**, 818–821 (2009).

[66]M. Komm, R. Dejarnac, J. P. Gunn, and Z. Pekarek, "Three-dimensional particle-in-cell simulations of gap crossings in castellated plasma-facing components in tokamaks", Plasma Physics and Controlled Fusion **55**, 25006 (2013).

[67]M. Komm, J. P. Gunn, R. Dejarnac, R. Pánek, R. A. Pitts, and A. Podolnik, "Particle-in-cell simulations of the plasma interaction with poloidal gaps in the ITER divertor outer vertical target", Nuclear Fusion **57** (2017).

[68]A. Podolnik, M. Komm, J. Adámek, P. Háček, J. Krbec, R. Dejarnac, J. P. Gunn, and R. Pánek, "3D particle-in-cell modeling of Langmuir probe effective collecting area in magnetized plasma", Plasma Physics and Controlled Fusion **60** (2018).

[69]A. Podolník, M. Komm, R. Dejarnac, J. P. Gunn, and R. Pánek, "Interpretation of flush-mounted probe current-voltage characteristics using four-parametric fits", Plasma Physics and Controlled Fusion **61**, 105011 (2019).

[70]A. Podolnik, "Study of probe diagnostics of tokamak edge plasma via computer simulation", PhD thesis (2019).

[71]K. S. Chung and I. H. Hutchinson, "Kinetic theory of ion collection by probing objects in flowing strongly magnetized plasmas", Physical Review A **38**, 4721–4731 (1988).

[72]J. P. Gunn, "Kinetic investigation of a collisionless scrape-off layer with a source of poloidal momentum", in Journal of nuclear materials, Vol. 337-339, 1-3 SPEC. ISS. (Mar. 2005), pp. 310–314.

[73]S. Murphy-Sugrue, Private Communication.

[74]J. Harrison, G. Fishpool, A. Kirk, and S. Allan, *Design of the MAST-U Divertor Langmuir Probe Tip Geometry*, tech. rep. (2012), p. 10.

[75]D. Buchenauer, W. L. Hsu, J. P. Smith, and D. N. Hill, "Langmuir probe array for the DIII-D divertor", Review of Scientific Instruments **61**, 2873–2875 (1990).

[76]J. G. Watkins, D. Taussig, R. L. Boivin, M. A. Mahdavi, and R. E. Nygren, "High heat flux Langmuir probe array for the DIII-D divertor plates", in Review of scientific instruments, Vol. 79, 10 (2008).

[77]S. Elmore, S. Y. Allan, A. Kirk, G. Fishpool, J. Harrison, P. Tamain, M. Kočan, R. Gaffka, R. Stephen, and J. W. Bradley, "Upstream and divertor ion temperature measurements on MAST by retarding field energy analyser", Plasma Physics and Controlled Fusion **54**, 065001 (2012).

[78]W. A. Vijvers, D. C. Schram, A. E. Shumack, N. J. Lopes Cardozo, J. Rapp, and G. J. Van Rooij, "Experimental and theoretical determination of the efficiency of a sub-atmospheric flowing high power cascaded arc hydrogen plasma source", Plasma Sources Science and Technology **19**, 065016 (2010).

[79]H. J. Van Der Meiden, A. R. Lof, M. A. Van Den Berg, S. Brons, A. J. Donné, H. J. Van Eck, P. M. Koelman, W. R. Koppers, O. G. Kruijt, N. N. Naumenko, T. Oyevaar, P. R. Prins, J. Rapp, J. Scholten, D. C. Schram, P. H. Smeets, G. Van Der Star, S. N. Tugarinov, and P. A. Van Emmichoven, "Advanced Thomson scattering system for high-flux linear plasma generator", Review of Scientific Instruments **83** (2012).

[80]A. Kirk, Private Communication.

[81]J. Leland, *flopter: Fitting and plotting workflow tools for analysing Langmuir probe data from a variety of sources.*

[82]J. van den Berg-Stolp, H. van den Meiden, I. Classen, J. Vernimmen, Y. Li, J. Scholten, S. Brons, and G. Van, "New pre-sheath boundary condition in dense thermal plasmas due to near-surface plasma-neutral coupling", Nuclear Fusion (Submitted for publication).

[83]C. R. Harris, K. J. Millman, S. J. van der Walt, R. Gommers, P. Virtanen, D. Cournapeau, E. Wieser, J. Taylor, S. Berg, N. J. Smith, R. Kern, M. Picus, S. Hoyer, M. H. van Kerkwijk, M. Brett, A. Haldane, J. F. del R'ıo, M. Wiebe, P. Peterson, P. G'erard-Marchant, K.

Sheppard, T. Reddy, W. Weckesser, H. Abbasi, C. Gohlke, and T. E. Oliphant, "Array programming with NumPy", Nature **585**, 357–362 (2020).

[84]M. Komm, Private Communication.

[85]J. Leland, S. Elmore, A. Kirk, H. J. van der Meiden, J. Scholten, S. Y. Allan, and J. W. Bradley, "Angular dependence measurements of Magnum-PSI plasmas using MAST-U angled-tip Langmuir probes", Nuclear Materials and Energy **27**, 100954 (2021).

[86]P. Ryan, Private Communication.

[87]C. Tryggestad, N. Sharma, O. Roser, B. Smeets, and J. van de Staaij, *Global Energy Perspective 2019 : Reference Case*, tech. rep. January (McKinsey, 2019).

[88]Ray and Douglas, *Lazard's Levelized Cost of Energy Analysis—Version 13.0*, tech. rep. (2020).

[89]BP, *Energy Outlook: 2020 edition*, tech. rep. (2020).

[90]*Net Zero Technical report*, tech. rep. 5 (UK Committee on Climate Change, 2019).

[91]R. Wakerling and A. Guthrie, *The characteristics of electrical discharges in magnetic fields* (McGraw-Hill, 1949).